# Paleoclimate reconstruction using LA-ICP-MS analyses of ostracods and stalagmite

Dissertation zur Erlangung des Grades

„Doktor der Naturwissenschaften“

am Fachbereich Chemie, Pharmazie und Geowissenschaften

vorgelegt von

M.Sc. Qichao Yang

geboren in Henan, China

Max Planck Graduate Center

mit der Johannes Gutenberg-Universität Mainz

angefertigt am Max-Planck-Institut für Chemie

Mainz, 2014

I hereby declare that I wrote the dissertation submitted without any unauthorised external assistance and used only sources acknowledged in the work. All textual passages which are appropriated verbatim or paraphrased from published and unpublished texts as well as all information obtained from oral sources are duly indicated and listed in accordance with bibliographical rules. In carrying out this research, I complied with the rules of standard scientific practice as formulated in the statutes of the Johannes Gutenberg University, Mainz, to ensure standard scientific practice.

May 20, 2014

Qichao Yang

# Abstract

Ostracod shells and stalagmites can be applied as archives for palaeoclimate reconstruction. However, high-resolution results for multiple trace element concentrations in single ostracod shells have not been reported until now. Radiogenic Pb isotopic characteristics in stalagmite samples have also not been determined in previous studies. In this study, in order to investigate the past climate processes in different continental regions, a new LA-ICP-MS (laser ablation-inductively coupled plasma-mass spectrometry) technique was developed for in-situ trace element and Pb isotope measurements at high-resolution. To evaluate the suitability of calibration material for this technique, LA-ICP-MS was first used to test the silicate reference glasses BAM-S005-A and BAM-S005-B from BAM (The Federal Institute for Materials Research and Testing, Germany). The homogeneity of these reference glasses was investigated using LA-ICP-MS and the other microanalytical techniques EPMA and SIMS. The results indicated that all major and most trace elements are homogeneously distributed at micrometre sampling scale in both glasses. However, some trace elements (e.g., Cs, Cl, Cr, Mo and Ni) are inhomogeneously distributed. The major element composition of BAM-S005-A and BAM-S005-B was determined by EPMA analysis; the results confirmed the information values specified by the BAM certificate. With the exception of Sr, Ba, Ce and Pb, the LA-ICP-MS trace element data were also in agreement with the certified values within the stated uncertainty limits. The reasons for the discrepancy found for these four elements mentioned above are still unclear, but may be related to erroneous reference values. In addition, new data for twenty-two further trace elements were obtained, for which the concentrations had not been certified by BAM. Based on these investigations, it is assumed that both BAM glasses are suitable for many microanalytical applications.

In order to investigate novel palaeoclimate proxies in ostracod calcite from Tibetan lake sediments, the trace element variability in single ostracod valves was determined by a new LA-ICP-MS technique. Ostracod shells, belonging to three taxa (*Leucocytherella sinensis* Huang, 1982, ?*Leucocythere dorsotuberosa* Huang, 1982 and ?*L. dorsotuberosa* f. *postilirata sensu* Pang, 1985), were collected from two sediment cores from Lake Nam Co, on the central Tibetan Plateau. Two variants of LA-ICP-MS, spot and line-scan analysis, were applied to determine trace element concentrations (Mg, Sr, Ba, U and rare earth elements [REEs]) in single ostracod shells. The results suggest that the line-scan method can provide more precise data than the spot analysis and is therefore preferred. No significant difference in trace element composition between taxa was detected in this study.

Variations of Mg/Ca and Sr/Ca in the shells show good agreement with the reported lake level changes during the Holocene, indicating that ostracod Mg and Sr can be related to palaeohydrochemical processes in this area. A high correlation between the Ba/Ca and Sr/Ca ratios was detected in this study, suggesting that Ba and Sr incorporation were controlled by the same mechanisms. A possible relationship between ostracod U/Ca and the past redox conditions on the lake bottom is discussed. Relatively low and constant La/Ca ratios were observed, which could be due to the REE characteristics in the lake water, or ostracod biological processes, or even the associated Fe-Mn and/or organic contaminants. Future studies on more specimens from this area, especially shells from living ostracods, are essential to investigate the potential of ostracod Ba, U and REEs for use as palaeoenvironmental indicators.

Moreover, LA-ICP-MS was used to analyse an aragonitic stalagmite sample. This study focuses on a section of ca. 6 cm length from stalagmite HBSH-1 from the Hüttenbläserschachthöhle, north-western Germany. Dating by the $^{230}Th/U$ method was performed with solution multi-collector-ICP-MS. The results revealed that the section has an age between ~210.0 and ~190.0 ka, with a relatively uniform growth rate of 3.1 µm a-1. Trace element (Sr, Mg, Al, Si, Mn, Th, P and Pb) concentrations and Pb isotope ratios ($^{207}Pb/^{206}Pb$ and $^{208}Pb/^{206}Pb$) along the growth axis were determined by LA-ICP-MS analysis. This is the first time that radiogenic Pb isotopes in stalagmite samples have been measured. The results of the trace element analyses show distinct covariations between Mg, Al, Si, Mn, Th, P and Pb, probably due to their similar transport and incorporation phases, i.e., colloids and/or particles. Strontium, likely mobilized and incorporated as free ions, is not correlated with the other elements. Two intervals (from ~204.9 to ~201.5 and ~198.4 to ~195.9 ka) associated with higher concentrations of Mg, Al, Si, Mn, Th, P and Pb are interpreted to reflect strong water infiltration, whereas three intervals (from ~210.0 to ~204.9, ~201.5 to ~198.4 and ~195.9 to ~190.0 ka) with rather low concentrations are linked to lower recharge. The isotope ratios $^{207}Pb/^{206}Pb$ and $^{208}Pb/^{206}Pb$ show a positive relationship with each other, as well as with the trace element (except Sr) concentrations, potentially indicating a mixture of two Pb components with different isotope ratios. The component with higher Pb isotope ratios may originate from galena minerals in the cave area, while the component with lower isotope ratios is probably derived from the carbonate fraction of the limestone host rock. In summary, with the help of LA-ICP-MS, it is suggested that BAM silicate glasses are suitable calibration materials for microanalysis. The trace element concentrations and/or radiogenic Pb isotopes in ostracod and stalagmite samples can provide meaningful information for palaeohydrological and palaeohydrochemical changes under different environmental (lacustrine/karstic) conditions.

# Zusammenfassung

Als paläoklimatische Archive können unter anderem Stalagmiten und Klappen von Ostrakoden herangezogen werden. Bisher gab es noch keine veröffentlichten Ergebnisse räumlich hochaufgelöster Spurenelementverteilungen in einzelnen Ostrakodenklappen. Das gleiche gilt für die Bestimmung radiogener Blei-Isotope in Stalagmiten. Um klimatische Prozesse vergangener Zeiten zu untersuchen, wurde eine neue LA-ICP-MS (Laserablations – Massenspektrometrie mit induktiv gekoppeltem Plasma) Technik für hochaufgelöste in-situ Messungen von Spurenelementen und Bleiisotopen entwickelt.

Zunächst wurden geeignete Materialien für die Kalibrierung der Technik untersucht; als Proben dienten die Silikatreferenzgläser BAM-S005-A und BAM-S005B der Bundesanstalt für Materialforschung und –prüfung (BAM). Die Homogenität dieser Referenzgläser wurde mit LA-ICP-MS und den anderen mikroanalytischen Methoden EPMA (Elektronenmikrosonde) und SIMS (Ionensonde) überprüft. Die Ergebnisse zeigten, dass alle Haupt- und die meisten Spurenelemente in beiden Gläsern selbst im Mikrometerbereich homogen verteilt sind. Ausnahmen sind einige Spurenelemente, wie Cs, Cl, Cr, Mo und Ni, die heterogen in den Gläsern verteilt sind. Die Hauptelementzusammensetzung von BAM-S005-A und BAM-S005-B wurde mit Hilfe der EPMA bestimmt, wobei die Ergebnisse die Referenzwerte des BAM-Zertifikats bestätigten. Mit Ausnahme von Sr, Ba, Ce und Pb, stimmten die LA-ICP-MS-Spurenelementwerte mit den zertifizierten Werten innerhalb der angegebenen Fehlergrenzen überein. Gründe für die Diskrepanz der vier oben erwähnten Elemente sind noch unklar, aber sind möglicherweise durch fehlerhafte Referenzwerte zu erklären. Zusätzlich wurden 22 Spurenelemente gemessen, deren Gehalte von BAM nicht zertifiziert wurden. Aufgrund dieser Untersuchungen konnte festgestellt werden, dass beide BAM-Gläser für mikroanalytische Anwendungen geeignet sind.

Um neuartige paläoklimatische Proxies im Calcit von Ostrakoden aus tibetanischen Seesedimenten zu untersuchen, wurde die Spurenelementvariabilität in einzelnen Ostrakodenklappen durch eine neue LA-ICP-MS-Technik bestimmt. Klappen von Ostrakoden der drei Arten (*Leucocytherella sinensis* Huang, 1982, ?*Leucocythere dorsotuberosa* Huang, 1982

und ?*L. dorsotuberosa* f. *postilirata sensu* Pang, 1985) wurden aus zwei Sedimentkernen des Nam Co Sees auf dem Hochplateau von Tibet gewonnen. Zwei LA-ICP-MS-Varianten, Spot- bzw. Linienanalyse, wurden verwendet, um die Elementkonzentrationen der Spurenelemente Mg, Sr, Ba, U und die der Seltenen Erdelemente (SEE) in den Klappen einzelner Ostrakoden zu bestimmen. Die Ergebnisse zeigten, dass die Linienanalyse präzisere Daten als die Spotanalyse liefert und sie wurde daher vorgezogen. Signifikante Unterschiede in der Spurenelementzusammensetzung zwischen den verschiedenen Arten der Ostrakoden wurden nicht gefunden. Variationen der Elementverhältnisse Mg/Ca und Sr/Ca in den Klappen stimmen mit veröffentlichten Seenspiegelschwankungen während des Holozäns überein, was zeigt, dass Mg- und Sr-Messungen in den Ostrakoden zur Untersuchung paläohydrochemischer Prozesse in diesem Gebiet herangezogen werden kann. Die gute Korrelation, die in dieser Arbeit zwischen Ba/Ca und Sr/Ca gefunden wurde, ist ein Hinweis darauf, dass der Einbau von Ba und Sr in die Klappen durch den gleichen Mechanismus erfolgte. Eine mögliche Beziehung zwischen dem U/Ca-Verhältnis in den Ostrakoden und den Redoxbedingungen auf dem Boden des Sees in der Vergangenheit wird diskutiert. Relativ geringe und konstante La/Ca-Verhältnisse wurden festgestellt, deren Ursache möglicherweise entweder auf der SEE-Charakteristik des Seewassers, auf biologischen Prozessen in den Ostrakoden oder auf Kontamination von Fe-Mn und/oder organischen Substanzen beruhen. Weitere Untersuchungen an Proben aus diesem Gebiet, speziell Klappen von lebenden Ostrakoden, sind notwendig, um den Gehalt von Ba, U und den SEE in Ostrakoden als paläoklimatische Proxies von Umweltbedingungen zu verwenden.

Darüber hinaus wurde LA-ICP-MS verwendet, um eine aus Aragonit bestehende Stalagmitprobe zu analysieren. Diese Studie konzentrierte sich auf einen ca. 6 cm langen Abschnitt des Stalagmiten HBSH-1 aus der Hüttenbläserschachthöhle in Nordwestdeutschland. Die Altersbestimmung mit Hilfe der $^{230}$Th/U-Methode wurde mit Lösungs-Multikollektor-ICP-MS durchgeführt. Die Ergebnisse zeigten, dass der Abschnitt ein Alter zwischen ~210.0 und ~190.0 ka hat, mit einer relativ gleichförmigen Wachstumsrate von 3,1 µm a$^{-1}$. Die Konzentrationen der Spurenelemente Sr, Mg, Al, Si, Mn, Th, P und Pb sowie die Blei-Isotopenverhältnisse $^{207}$Pb/$^{206}$Pb und $^{208}$Pb/$^{206}$Pb entlang der Wachstumsachse wurde mit der LA-ICP-MS bestimmt. Hier wurden zum ersten Mal radiogene Blei-Isotope in Stalagmiten gemessen. Die Ergebnisse der Spurenelementanalysen zeigen deutliche Kovariationen zwischen Mg, Al, Si, Mn, Th, P und Pb, was wahrscheinlich durch ähnliche Transport- und Aufnahmephasen, d.h. über Kolloide und/oder Partikel, zu erklären ist. Strontium, das wahrscheinlich als freie Ionen mobilisiert und eingebaut wurde, zeigt keine Korrelation mit den anderen Elementen. Zwei Zeitintervalle (von

~204.9 bis ~201.5 ka und ~198.4 bis ~195.9 ka), die mit hohen Konzentrationen von Mg, Al, Si, Mn, Th, P und Pb in Verbindung stehen, werden als Zeiten hoher Wasserinfiltration interpretiert, wohingegen drei Intervalle (von ~210.0 bis ~204.9 ka, ~201.5 bis ~198.4 ka und ~195.9 bis ~190.0 ka) mit ziemlich geringen Konzentrationen als Zeiten geringer Grundwasserbildung interpretiert werden. Die Isotopenverhältnisse von $^{207}Pb/^{206}Pb$ und $^{208}Pb/^{206}Pb$ sind positiv miteinander korreliert, aber auch mit den Spurenelementkonzentrationen (Sr ausgenommen), was möglicherweise durch eine Mischung zweier Bleikomponenten mit unterschiedlichen Isotopenverhältnissen zu erklären ist. Die Komponente mit den hohen Blei-Isotopenverhältnissen dürfte ihren Ursprung im Bleiglanz aus der weiteren Umgebung der Höhle haben, während die Komponente mit den niedrigen Isotopenverhältnissen wahrscheinlich von der Carbonatfraktion des Kalksteins herrührt.

Die Ergebnisse dieser Arbeit zeigen, dass BAM-Silikatgläser geeignete Referenzmaterialien zur Kalibrierung von LA-ICP-MS sind. Über Spurenelementkonzentrationen und/oder radiogene Blei-Isotope in Ostrakoden- und Stalagmitproben können aussagekräftige Informationen über paläohydrologische und paläohydrochemische Veränderungen unter verschiedenen Umweltbedingungen (lakustrisch/karstisch) gewonnen werden.

# Acknowledgements

I would like to acknowledge all the people who helped me during my PhD period. A special thanks to my family, without whom I wouldn't have persisted for so many years!

# Contents

# Chapter 1

# Introduction

## 1.1 LA-ICP-MS

Laser ablation-inductively coupled plasma-mass spectrometry (LA-ICP-MS) is a powerful micro-analytical method used in many different disciplines, such as geochemistry, cosmochemistry, environmental science and so on (Jochum et al., 2012). This technique has the advantage of low detection limits (at the level of ng $g^{-1}$) and high spatial resolution (in the range of 10-100 μm), and therefore can provide high-resolution results for the analyzed specimens (Jochum et al., 2012). Different combinations of ICP-MS instruments and laser ablation systems are used for the LA-ICP-MS analysis. Some of the most commonly used ICP-MS and LA systems are compiled in the following tables (Tables 1.1 and 1.2).

In this study, a high-resolution sector-field ICP-MS Thermo Element2 combined with the 193 (UP-193SS) and 213 (UP-213) nm Nd:YAG laser ablation system from New Wave is used. The basic principle for such a MS system is: the surface of the analyzed sample, where the laser focuses on, releases particles due to laser ablation. These particles are then transported to the ICP by carrier gas and ionized there due to the high temperature (~8000 °C). The ions are separated by the magnetic sector field based on the mass-to-charge ratio, as well as by the electric sector field according to the kinetic energy, and quantified (Jochum et al., 2009). Due to fast magnets, the scan time can last approximately 1-2 s for LA-ICP-MS analysis of 40-50 trace elements (Jochum et al., 2009).

LA-ICP-MS has been widely used to test homogeneity and elemental composition in a variety of reference glasses (e.g., Guilong et al., 2005; Jochum et al., 2006, 2011; Hu et al., 2011). Recently, Jochum et al. (2012) demonstrated the applicability of LA-ICP-MS on trace elements in inorganic (speleothems) and biogenic (ostracods) calcium carbonates to improve the application of this technique in paleoclimate and paleoenvironmental studies.

Table 1.1: The widely applied ICP-MS for LA-ICP-MS analysis (adapted from Jochum et al. (2009)).

| Mass spectrometers | Scan time from one mass to another | Mass resolution | Peak shape | Sensitivity | Applications |
|---|---|---|---|---|---|
| Quadrupole | fast | 300-400 | triangular | medium to high | elemental analysis |
| Single collector sector-field | electrical scan: fast; magnetic scan: slow | 300-10,000 | flat top | high | elemental and isotopic analysis |
| Time-of-flight | very fast | 500-2000 | triangular | low | fast scanning capability |
| Multicolletor sector-field | very slow | 300 | flat top | high | high-precision isotopic analysis |

Table 1.2: The widely applied laser ablation systems for LA-ICP-MS analysis (adapted from Jochum et al. (2009)).

| LA system | wavelength (nm) | pulse energy (mJ) | pulse width | repetition rate (Hz) | crater size (μm) |
|---|---|---|---|---|---|
| Nd:YAG | 266 | 0.5-4 | 9 ns | 1-20 | 3-80 |
| Nd:YAG | 213 | 0.2-2 | 5 ns | 1-20 | 2-160 |
| Nd:YAG | 193 | 0.1-1 | 3 ns | 1-10 | 5-100 |
| ArF excimer | 193 | 0.05-0.8 | 15 ns | 1-100 | 4-200 |
| fs laser | 196-800 | 1-4 | 60-400 fs | 1-1000 | 5-100 |

## 1.2 BAM reference glasses

Reference glasses are essential materials for many microanalytical techniques, e.g., LA-ICP-MS, secondary ionization mass spectrometry and synchrotron radiation induced X-ray fluorescence (Jochum and Stoll 2008). They are widely used for calibration, quality control, method development and inter-laboratory comparison. Until now, approximate twenty reference glasses are available for microanalysis, while the demand for suitable reference glasses is still increasing (Jochum and Stoll 2008; Hu et al., 2011). Two of the most commonly used reference glasses are NIST SRM 610 and 612, produced by the National Institute of Standards and Technology, USA, with the advantage of high abundances for many trace elements. In paleoenvironmental studies, carbonate specimens are usually investigated, such as corals (Scholz et al., 2004; Scholz and Hoffmann, 2008), speleothems (Fairchild and Treble, 2009; Wassenburg et al., 2012, 2013), fossil ostracods (Börner et al., 2013; Yang et al., 2014). Different matrices between carbonate samples and silicate reference glasses, when LA-ICP-MS is

applied, could influence the measurement accuracy. However, Jochum et al. (2012) demonstrated that the matrix effect for lithophile refractory elements, such as Ca, Sr, Ba, REEs, U and Th, in speleothem and ostracod calcite is insignificant for LA-ICP-MS analysis using 213 and 193 nm Nd:YAG laser ablation system.

The Federal Institute for Materials Research and Testing (BAM, Germany) has launched two soda lime reference glasses (BAM-S005-A and BAM-S005-B, Matschat et al., 2005) in cooperation with the International Commission on Glass (ICG), Technical Committee 2 (TC 2). The preparation processes of the BAM-S005 glasses have been described in detail in the BAM certificate (Matschat et al., 2005). Initially, both glasses were designed for bulk analyses, such as X-ray fluorescence. The concentrations of twenty-two elements, including rarely analyzed elements such as As, S, Cl, Se and Cd, have been certified in the framework of an inter-laboratory comparison using three to nine different analytical methods in twenty-three different laboratories (Matschat et al., 2005). In this study, the homogeneity of both glasses was investigated to evaluate whether they were suitable for microanalysis. Concentrations of a set of major (such as Si, Na, Ca, Mg, Al and K) and trace (such as As, Ba, Cr, Fe, Mn and Th) elements were also determined by LA-ICP-MS.

## 1.3 Ostracod shells

Ostracods are small, bivalve crustaceans with typical sizes around 1 mm, comprehensively existing in different aquatic environments (Holmes, 2008). During the lifetime of ostracods, their growth accompanies with a series of moult stages, notated as A-1, A-2…. etc., representing the penultimate and pre-penultimate etc. juvenile stage (Griffiths and Holmes, 2000). After moulting, new shells of low-Mg calcite are secreted. The moulting and secreting processes cease when ostracods are adult (Griffiths and Holmes, 2000). Their shells are often well preserved in lake and/or marine sediments and provide important implications for past climatic and environmental processes (Griffiths and Holmes, 2000; Börner et al., 2013).

The trace element chemistry (mainly Mg and Sr) in non-marine ostracod calcite has been widely used for paleosalinity reconstructions. Evaporative concentration in hydrologically closed basins often induces precipitation of $CaCO_3$, causing an elevation of Mg/Ca and Sr/Ca and therefore a positive relationship between the element ratios and salinity in the host water (Holmes

et al., 1999). Since Mg/Ca and Sr/Ca in ostracod shells have been demonstrated to be a function of the same ratios in solutions, a possible positive correlation between the ratios in ostracod calcite and water salinity can be expected under certain circumstances (e.g., Chivas et al., 1983, 1985, 1986; Engstrom and Nelson, 1991; Holmes, 1996; Xia et al., 1997a,b; Wansard et al., 1998; De Deckker et al., 1999). Ostracod Mg/Ca may also depend on the water temperature, while Sr/Ca is relatively independent of temperature in the ranges in which ostracods normally live (Chivas et al., 1983, 1985, 1986; Engstrom and Nelson, 1991). A possible relation between ostracod U/Ca and the redox conditions in the lake bottom water was also reported by Ricketts et al. (2001). Moreover, the stable isotope ratios ($\delta^{18}O$ and $\delta^{13}C$) in ostracod calcite are also widely used proxies, shedding light on paleotemperature, meteoric precipitation source, precipitation/evaporation balance, the residence time of the waterbody and primary production in lacustrine systems (Griffiths and Holmes, 2000).

In this study, three ostracod taxa, i.e., *Leucocytherella sinensis,* ?*Leucocythere dorsotuberosa* f. *typical* and ?*L. dorsotuberosa* f. *postilirata*, were collected from two sediment cores Nam Co 8 and NC 08/01 from Lake Nam Co on the Tibetan Plateau (TP). All three taxa are endemic to the TP and adjacent areas and tolerate cold and saline aquatic environments (Huang et al., 1985; Zhang et al., 2006a; Wrozyna et al., 2009a). Trace element (such as Mg, Sr, Ba, U and 14 rare earth elements) compositions in single ostracod shells were determined by LA-ICP-MS analyses. Past hydrologic and hydrochemical changes in this lake system during the Holocene period were discussed.

## 1.4 Stalagmite

Speleothems, including stalagmites, stalactites and flowstones, are secondary mineral deposits formed in karstic cave systems. The processes of calcite precipitation and stalagmite growth have been described in detail by previous studies (Dreybrodt, 1999; Kaufmann, 2003; Fairchild et al., 2006; Mühlinghaus et al., 2007). In general, the soil zone above the cave has high $pCO_2$ values due to vegetation decay and biological activity (McDermott, 2004). Percolating rainwater through the soil dissolves the underlying carbonate host rock as the following equation:

$$CaCO_3 + CO_2 + H_2O \leftrightarrow Ca^{2+} + 2HCO_3^-$$

Due to lower $pCO_2$ in the cave, $CO_2$ degassing starts when drip water enters the cave. The drip water gets supersaturated with respect to calcite and calcite is precipitated to form stalactites (Scholz et al., 2009). When drip water finally

drops on the top of stalagmites, degassing process further proceeds and promotes new calcite layers deposited on stalagmites.

Stalagmites have been widely used as archives in paleoclimate studies (e.g., McMillan et al., 2005; Spötl et al., 2008; Wang et al., 2008; Wassenburg et al., 2012) because they have long continuous growth periods (Mühlinghaus et al., 2008), which can be dated precisely and accurately by U-series methods (Scholz and Hoffmann, 2008), and high-resolution multiple paleoenvironmental proxies (Fairchild et al., 2006). As the most commonly measured proxies, the carbon and oxygen isotopes ($\delta^{13}C$ and $\delta^{18}O$) in stalagmites have been utilized to reflect soil/vegetation dynamics (Genty et al., 2003) and cave temperature/meteoric precipitation changes (McDermott, 2004) respectively. Recently, trace elements preserved in stalagmites have received more and more attention (Treble et al., 2003; Fairchild et al., 2006; Borsato et al., 2007; Fairchild and Treble, 2009; Wassenburg et al., 2012, 2013). Speleothem Mg, Sr and Ba may reflect the prior calcite process and/or prior aragonite process in the epikarst zones, while Th, Si, Mn and Al could be linked to the detrital material input due to flushing events (Fairchild and Treble, 2009; Wassenburg et al., 2012).

The Pb radiogenic isotopes $^{206}Pb$, $^{207}Pb$ and $^{208}Pb$, produced by the radioactive decay of $^{238}U$, $^{235}U$ and $^{232}Th$ respectively, have been successfully applied to trace the global and local Pb pollution sources, such as leaded gasoline, coal combustion, metallurgical activities and waste incineration (Monna et al., 1997; Hansmann and Köppel, 2000; Ettler et al., 2004; Carignan et al., 2005). Pb isotopes have also been used for U-Pb dating on speleothem specimens (Richards et al., 1998; Bajo et al., 2012). However, these variables have not been used as paleoenvironmental proxies in stalagmites. In this study, an aragonitic stalagmite was retrieved from the Hüttenbläserschachthöhle, north-western Germany. A set of trace elements (Sr, U, Mg, Th, Si, Mn, P and Pb) and Pb isotope ratios ($^{207}Pb/^{206}Pb$ and $^{208}Pb/^{206}Pb$) were investigated by LA-ICP-MS analyses in this sample. The possible paleohydrological processes during the MIS 7 period in the sampling area were discussed.

# Chapter 2

# BAM-S005 Type A and B: New silicate reference glasses for microanalysis

This chapter is published as Yang Q, Jochum KP, Stoll B, Weis U, Kuzmin D, Wiedenbeck M, Traub H and Andreae MO (2012) Geostandards and Geoanalytical Research 36, 301-313.

## 2.1 Introduction

Reference glasses are essential materials for many microanalytical methods, such as laser ablation – inductively coupled plasma – mass spectrometry (LA-ICP-MS), secondary ionization mass spectrometry (SIMS) and synchrotron radiation induced X-ray fluorescence (SY-XRF) (Jochum and Stoll 2008). They are widely needed as reference materials in geochemistry, cosmochemistry and environmental research for calibration, quality control, method development and inter-laboratory comparison purposes. Currently, there are about twenty reference glasses available that are suitable for microanalysis (Jochum and Stoll 2008; Hu et al., 2011). The National Institute of Standards and Technology's (NIST) standard reference materials (SRMs) NIST SRM 610 and 612 are commonly used for calibration purposes; these glasses have the advantage that they contain many trace elements at concentrations that are high enough for a low uncertainty calibration (ca. 400 and 40 μg $g^{-1}$ for NIST SRM 610 and 612, respectively). Eggins and Shelley (2002) and Jochum et al. (2011) investigated the suitability of these NIST glasses for microanalysis by assessing possible inhomogeneities. Jochum et al. (2011) also provided reference values and their 95% confidence level uncertainties for different test portion masses following ISO guidelines (ISO Guide 35).

With the growth in use of microanalytical techniques, the demand for suitable reference glasses has been increasing in the past few years. The Federal Institute for Materials Research and Testing (BAM, Germany) has launched two soda-lime reference glasses (BAM-S005-A and BAM-S005-B; Matschat et al., 2005) in cooperation with the International Commission on Glass (ICG), Technical Committee 2 (TC 2). The concentrations of twenty-two elements,

including rarely analyzed elements such as As, S, Cl, Se and Cd, have been certified in the framework of an inter-laboratory comparison using three to nine different analytical methods in twenty-three different laboratories. These two glasses were initially designed for bulk analytical purposes, such as X-ray fluorescence (XRF). The aim of this paper is to evaluate whether the BAM glasses are also suitable for microanalysis. Here we investigate the homogeneity of the BAM glasses using electron probe microanalysis (EPMA), LA-ICP-MS and SIMS. In addition, the concentration data of the major and 44 trace elements are also reported.

## 2.2 Experimental procedure

### 2.2.1 Samples

The preparation procedures of the BAM-S005 glasses have been described in detail in the BAM certificate (Matschat et al., 2005). Weighed pure chemicals were added to a typical soda lime glass batch (about 86 kg in total), melted at a temperature of 1400 ˚C for 12 hours and then conditioned at 1100 ˚C for an additional 8 hours to allow the resorption of gas bubbles. After removing the upper layers, melt glass was gathered with a cast iron spoon and poured over steel plates to obtain thirty-four glass cakes. After abrading the surface to remove contamination, each glass cake was divided into four discs with a diameter of about 4 cm and a thickness of 0.7-0.8 cm, using a hole saw. This set of samples was named “type A material” (BAM-S005-A, 129 discs). Owing to some bubbles appearing in these glass samples and the desire to improve glass quality, the remaining melt was further conditioned for 24 hr and then sampled using the same procedure as for the BAM-S005-A glasses. The second set of discs was denoted as “type B material” (BAM-S005-B, 130 discs). In our study, fragments (ca. 30 mm in size) of both types of BAM glass were analyzed, which had been polished on one side.

### 2.2.2 Analytical techniques

The BAM-S005 glasses were analyzed using EPMA, LA-ICP-MS and SIMS. A brief description of each technique is given in the following section.

EPMA at the MPI Mainz: Measurements of major elements were performed at the Max Planck Institute for Chemistry (MPI), Mainz, Germany. Analyses were

carried out in the wavelength-dispersive detection mode of the JEOL Superprobe JXA-8200 electron microprobe at 15-kV accelerating voltage and 12-nA beam current. To avoid the loss of Na during the measurements, the electron beam was defocused to 20 µm and the step width was 50 µm. The data were corrected using routine ZAF procedure. Peak counting times were 30 s for Na and 60 s for all other major elements. The following spectrometers were used to determine the major element concentrations: TAP (thallium acid phthalate) for Na, Si, Al and Mg, PET (pentaerythritol) for Ca and K. Under these conditions the detection limits were around 150 µg $g^{-1}$ for Si, Al and Ca, 250 µg $g^{-1}$ for Na and 100 µg $g^{-1}$ for K and Mg. A set of reference materials, i.e., natural and synthetic oxides, minerals and glasses (P&H Developments Ltd., Calibration Standards for Electron Probe Microanalysis, Standard Block GEO, and the Smithsonian Institution standard set for electron microprobe analysis) (Jarosewich 2002) was used for routine calibration and instrument stability monitoring. As monitor samples to assess repeatability and to test the presence of any bias, we used the USNM 111240/52 VG2 basaltic glass, USNM 72854 VG-568 acidic alkaline glass (Jarosewich 2002) and also NIST SRM 610 and 612 reference glasses. A total of 323 spots were measured for BAM-S005-A and 215 spots for BAM-S005-B. The test portion mass for EPMA at the 20 µm spot size was about 0.01 µg.

LA-ICP-MS at the MPI Mainz: The analytical procedure for LA-ICP-MS at the MPI Mainz has been described in detail by Jochum et al. (2007). This investigation of the homogeneity of the BAM-S005 glasses used both a 193 nm (UP-193SS) and a 213 nm (UP-213) Nd:YAG laser ablation system from New Wave. For both systems, ablation was carried out in a He atmosphere, which was mixed with the Ar carrier gas prior to the plasma torch. Spot analyses were performed using spot diameters ranging between 35 and 95 µm (UP-193SS) and 25 and 55 µm (UP-213) with energy densities of 5-16 J $cm^{-2}$. These experiments used a 500 µm spacing across the diameter of the BAM fragments. Ablation time was 80 or 110 s, washout time between spot was 30 or 60 s and blank count rates were measured for either 13 or 14 s prior to ablation (details are shown in Table 2.1).

Table 2.1: Operating parameters for the laser ablation system UP-193SS and UP-213.

| **Samples** | **BAM-S005-A** | | | | **BAM-S005-B** | | | |
|---|---|---|---|---|---|---|---|---|
| Laser ablation system | UP-193SS | | UP-213 | | UP-193SS | | UP-213 | |
| Spot sizes (µm) | 45 | 95 | 25 | 55 | 35 | 75 | 25 | 55 |
| Energy density (J $cm^{-2}$) | 12 | 11 | 12 | 16 | 5 | 11 | 10 | 15 |
| Ablation times (s) | 80 | 110 | 80 | 110 | 80 | 110 | 80 | 80 |
| Washout times (s) | 60 | 60 | 30 | 30 | 60 | 60 | 30 | 30 |
| Blank count times (s) | 13 | 14 | 13 | 14 | 13 | 14 | 13 | 13 |
| Pulse repetition (Hz) | 10 | 10 | 10 | 10 | 10 | 10 | 10 | 10 |

Ion intensities were measured at the low mass resolution of $m/\Delta m \approx 300$ using a single-collector sector-field Thermo Element 2 ICP mass spectrometer. Mass peaks were tested for possible interferences using the medium mass resolution mode ($m/\Delta m$ = 4000). The operating parameters for the ICP-MS are listed in Table 2.2. Tuning for the ICP-MS (Ar and He gas flows, torch position and focusing potentials) was performed using the NIST SRM 612 reference glass to achieve stable ion beam intensities and low oxide formation (ThO/Th < 0.5%) at maximum compatible transmission. Measurements were carried out using a combination of electrical and magnetic scan modes. The determination of forty-three trace element abundances required *ca.* 1.5 s per scan. For each run between sixty and eighty scans were made, depending on the spot sizes and laser wavelengths. A total of 240 spots were analyzed for BAM-S005-A and 252 spots for BAM-S005-B. Data reduction was performed by calculating the blank corrected count rates of the analyzed isotopes relative to the internal standard $^{43}Ca$, the values that were determined by EPMA. By this procedure, the impact of ion current drop during an individual analysis progress can be suppressed. To minimize matrix effects, the silicate reference glass NIST SRM 610 with a similar major element composition was used for external calibration of the analytical data of the BAM samples, and NIST SRM 612 was used to demonstrate the technique's robustness. Reference values used here were from Jochum et al. (2011).

Table 2.2: Operating parameters for the Element2 ICP-MS.

| | |
|---|---|
| RF power (W) | 1180 |
| Cooling gas flow rate (l $min^{-1}$) | 16 |
| Carrier gas (Ar) flow rate (l $min^{-1}$) | 0.4 |
| Carrier gas (He) flow rate (l $min^{-1}$) | 0.8 |
| Samples per peak | 120 |
| Time per pass (s) | 1.55 |
| Mass window (%) | 10 |

The isotopes selected for the LA-ICP-MS analyses are listed in Table 2.6, which also shows the detection limits using UP-193SS (95 µm spot size) and UP-213 (55 µm spot size) based on the 3s criterion, where s is the standard deviation of readings on the blank. Detection limits were found to decrease with increasing atomic number. To assess for any possible molecular and multiply-charged ion interferences on the measured isotopes, analyses of homogeneous reference glasses (such as NIST SRM 612 and 614 glasses) were performed using the medium mass resolution of $m/\Delta m$ = 4000. The analytical results indicated that the interferences were generally low. In particular, the count rate ratios of $^{40}Ar^{37}Cl^{+}/^{77}Se^{+}$, $^{16}O^{37}Cl^{+}/^{53}Cr^{+}$ and $^{68}Zn^{2+}/^{34}S^{+}$ were less than 2-3%, suggesting that the interferences of Cl molecules and $Zn^{2+}$ did not affect significantly the $^{77}Se$, $^{53}Cr$ and $^{34}S$ measurements.

SIMS at the GFZ Potsdam: The concentration homogeneity of P, S and Cl was determined at the Helmholtz Zentrum Potsdam GFZ using a Cameca ims 6f ion microprobe. The measurements were performed using a 30-µm diameter spot size normally with 10 keV $Cs^{+}$ primary ions operated at 1 nA. The total impact energy for the primary ions was 17.5 keV. Negative secondary ions were extracted using a 7.5 keV. The energy window was set at 50 eV width to which no energy offset was applied. The mass spectrometer was operated at high mass resolving power ($m/\Delta m$ = 4500). Secondary ion intensities were collected using a 750 µm field aperture (equivalent to a 60 µm diameter field-of-view at the sample surface). Count rates for $^{31}P^{-}$, $^{32}S^{-}$ and $^{37}Cl^{-}$ were normalized to the count rate of $^{18}O^{-}$. Relative ion yields were calibrated using the NIST SRM 610 (Jochum et al., 2011). Thirty-seven point analyses were performed on the type A material and twenty-nine were performed on type B. Because of the limited number of analyses, the SIMS measurements were focused on the middle and several locations near the edge for a single fragment rather than across the whole sample. Based on white light interferometer volume determinations, the test portion mass for each spot was approximately 1 ng.

## 2.3 Homogeneity

A homogeneous distribution of major and trace elements is a fundamental requirement for any microanalytical reference glass. Homogeneity is not an inherent property of a given material, rather it is element specific and must be defined for a selected test portion mass (Kane 2002). Where the relative standard deviation (RSD) for an element in a given sample is similar to the analytical repeatability determined by analyzing a homogeneous reference material, which closely matches in composition with the sample, this suggests

that chemical inhomogeneity for the element is smaller than the analytical uncertainty and hence not detectable.

We used EPMA to investigate the major element homogeneity across the glass fragments at 20 µm spot size and 50 µm step distance. Results for the $SiO_2$, $Na_2O$, CaO, MgO, $Al_2O_3$ and $K_2O$ abundances at different locations of the BAM glasses are shown in Figure 2.1. Table 2.3 lists the Poisson counting errors of X-ray intensities and the RSD values for the EPMA results. The RSD values for the major elements are 0.4-3.5%. The relatively high RSD values for $K_2O$ abundances (3.1% in BAM-S005-A and 3.5% in BAM-S005-B) are mainly caused by the measurement conditions of EPMA (12 nA, 15 kV) and the relatively low abundances of $K_2O$ (about 0.7% in both BAM glasses) in contrast to the abundances of other major elements. The counting errors of X-ray intensities for $Na_2O$, CaO, MgO, $Al_2O_3$ and $K_2O$ agree well with the observed analytical repeatability in the two glasses. This suggests that inhomogeneities for these elements were not detectable in either of the BAM glasses under the analytical conditions which we used. However, as shown in Table 2.3, the variability for $SiO_2$ was twice as large as the detected counting errors. To investigate whether this indicates an inhomogeneity of $SiO_2$ in the BAM glasses, the repeatability of $SiO_2$ in two reportedly homogeneous reference materials (USNM 72854 VG-568 and USNM 111240/52 VG2, Jarosewich 2002) was determined under the same analytical conditions. Both reference materials have $SiO_2$ abundances broadly comparable to the BAM glasses. The repeatability is about 0.5% in both of these two materials, indicating that the relatively high variability of $SiO_2$ in the BAM glasses could be attributed to the lower $SiO_2$ repeatability of the EPMA analyses rather than an inhomogeneous distribution of $SiO_2$ in the BAM glasses. Hence, we conclude that the BAM glasses appear to be homogeneous with respect to all the major elements at the 20 µm-scale.

Table 2.3: Counting errors (%) of X-ray intensities and RSD values (%) of EPMA results for BAM glasses.

| **Element** | **Counting errors of X-ray intensities** | **BAM-S005-A (% RSD)** | **BAM-S005-B (% RSD)** |
|---|---|---|---|
| $SiO_2$ | 0.2 | 0.48 | 0.43 |
| $Na_2O$ | 0.8 | 0.82 | 0.76 |
| CaO | 0.5 | 0.56 | 0.54 |
| MgO | 1.5 | 1.8 | 1.6 |
| $Al_2O_3$ | 1.0 | 1.1 | 1.1 |
| $K_2O$ | 3.3 | 3.1 | 3.5 |

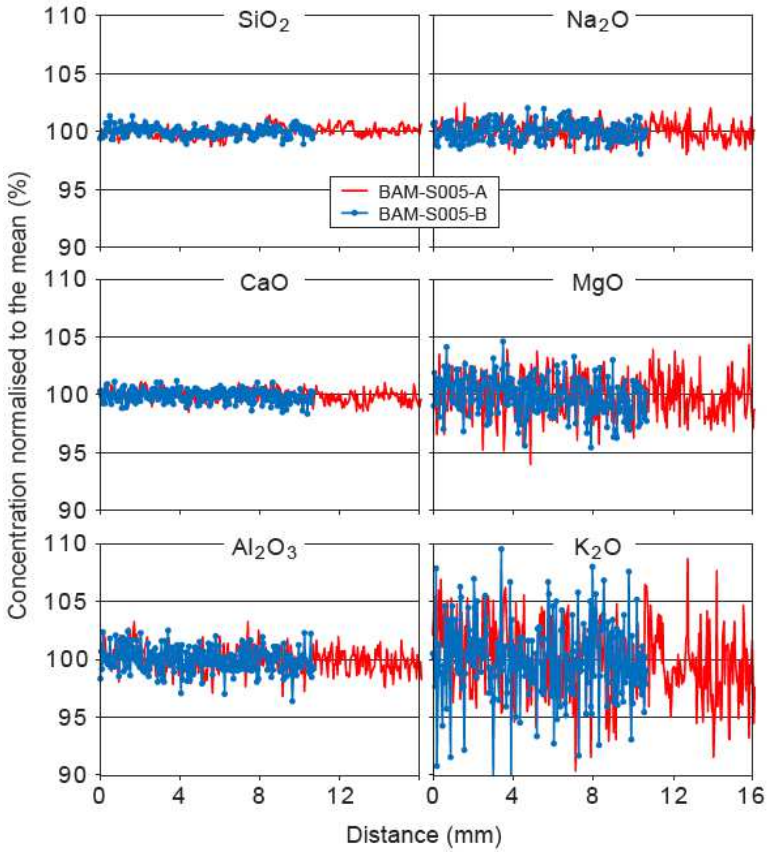


Figure 2.1: Variation of major element abundances across BAM-S005-A and BAM-S005-B glasses. The mean concentrations (represented as 100% in this figure) of the six major elements in both BAM glasses are shown in Table 2.5.

The homogeneity of trace elements in the BAM glasses was investigated using LA-ICP-MS (for forty-three trace elements except P) and SIMS (only for P, S and Cl). Figure 2.2 shows the mean count rates and RSD values for the isotopes measured (Table 2.6) using the two laser ablation systems UP-213 and UP-193SS, respectively, at spot sizes of 25-95 µm, equivalent to sample test portion masses of 0.02-1.5 µg. The mean count rate $CR_i$ of the measured isotope i is given by

$$CR_i = R_{ik} CR_k$$

where $R_{ik}$ is the mean ratio of the count rates of isotope i and of isotope k of the internal standard element ($^{43}$Ca in our study); $CR_k$ is the mean count rate of $^{43}$Ca. Because of the effectively constant relationship between the abundances of an element and its isotope(s), any variability in the content of the analyzed isotope must necessarily reflect an inhomogeneous distribution of the corresponding element in the measured sample.

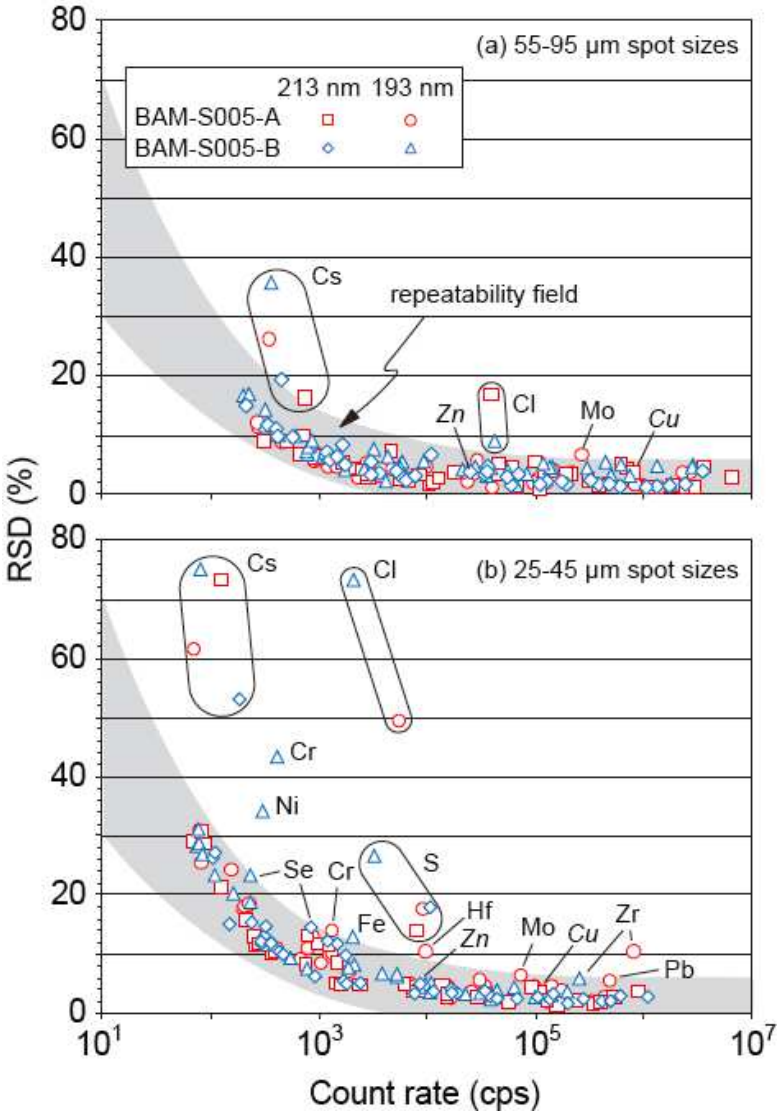


Figure 2.2: Relationship between the mean count rates and RSD values of measured isotopes in the BAM glasses. Measurements were performed with 55-95 µm and 25-45 µm spot sizes, respectively. Also shown is the repeatability field of LA-ICP-MS (Jochum et al., 2006, 2011; Hu et al., 2011). Data lying outside this field are thought to indicate heterogeneous element distribution in the BAM glasses while the values of Zn and Cu are within this field.

As expected, low count rate measurements usually have higher RSD values, which are obviously observed for those laser ablation analyses conducted at small spot sizes (Figure 2.2). For spot analyses of 25-95 µm, the RSD values increase from <5% at count rates >$1\times10^6$ cps to about 30% at count rates around 100 cps. Figure 2.2 also shows the analytical repeatability field (shaded field) for LA-ICP-MS, which was obtained by investigating the variability

of different trace elements in homogeneous reference glasses, such as MPI-DING glasses (Jochum et al., 2006), CGSG glasses (Hu et al., 2011) and NIST SRM glasses (Jochum et al., 2011). The repeatability field can be used to test the homogeneity of a given reference glass by assessing whether the variability of the trace elements of interest is within this field. The RSD values of most measured isotopes in the BAM glasses are within the repeatability field of LA-ICP-MS in Figure 2.2, implying that the corresponding trace elements display no significant heterogeneity in their distributions in either the type A or B material. Exceptions include such elements as Cs, Cl and Mo, for which the RSD values are outside the repeatability field at 55-95 μm spot sizes. For the 25-45 μm spot analyses, possible heterogeneities are also detected for Cr, Hf, Ni, Se, Fe, Pb, Zr and S.

We also tested the homogeneity of P, S and Cl for both BAM glasses using SIMS at low test portion mass (about 1 ng at the 30 μm crater size, Figure 2.3). Table 2.4 lists the analytical repeatability and the RSD values for the SIMS results. The analytical repeatability was obtained from the analyses of the variability of P, S and Cl in the calibration material (NIST SRM 610 glass). As shown in Table 2.4, the RSD values for the three elements are better than 5%, which agrees well with the analytical repeatability for SIMS, indicating that the three elements seem to be homogeneously distributed in both BAM glasses. This is in contrast to the observation from the LA-ICP-MS analyses, which suggested that the BAM glasses are inhomogeneous with respect to S and Cl to different degrees. Possible reasons causing the difference between the results of the two methods could be, first, the samples used in the SIMS analyses were different fragments from those measured by LA-ICP-MS (although all the samples were derived from the same disc of type A or B material), which could result in different homogeneity testing results; second, the LA-ICP-MS analyses were performed across the whole fragments of both BAM glasses whereas the SIMS measurements were only focused on the middle and several locations near the edge of the fragments (see the method description of LA-ICP-MS and SIMS), which could miss the possible heterogeneity information by SIMS because of the limited range of the measurements. Another possibility may be the poor LA-ICP-MS measurements of S and Cl because of high background (see the high LA-ICP-MS detection limits for S and Cl in Table 2.6).

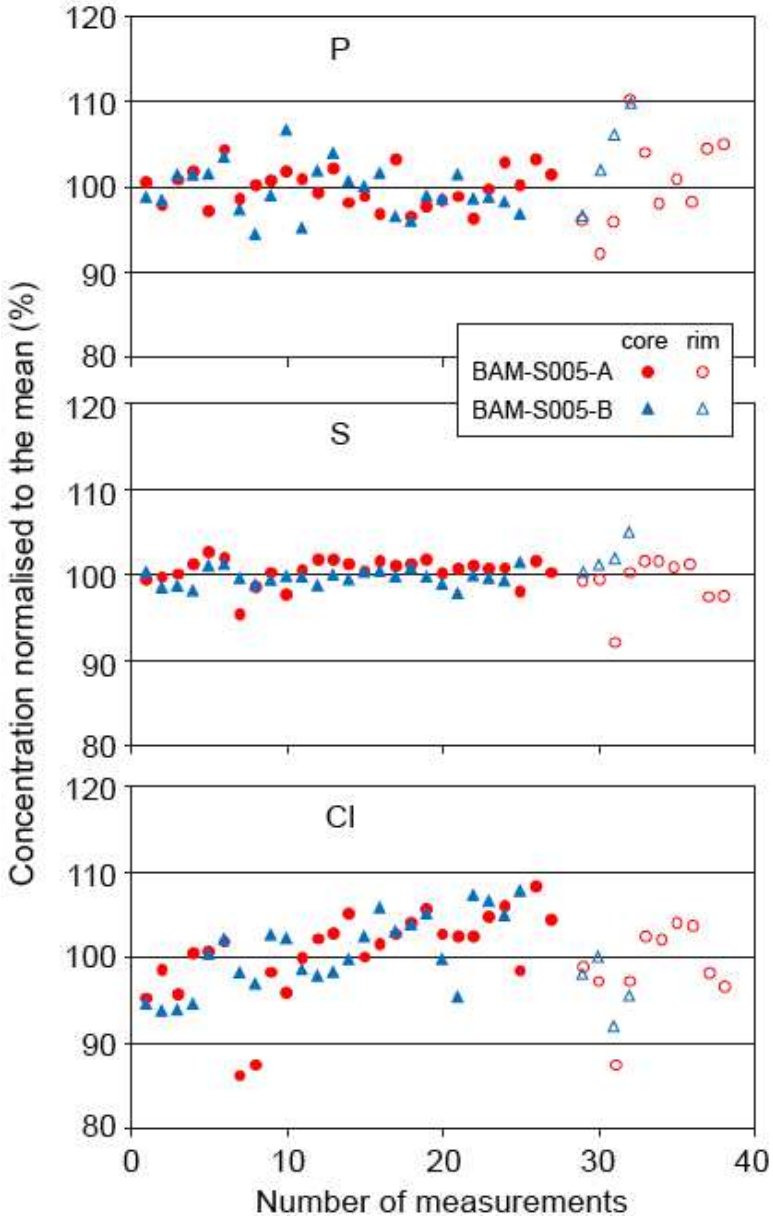


Figure 2.3: Variation of P, S and Cl abundances in the BAM glasses. The percentage (100%) represents the mean concentrations for the three elements.

Table 2.4: Analytical repeatability (%) and RSD values (%) of SIMS results for the BAM glasses.

| Element | Repeatability | BAM-S005-A | BAM-S005-B |
|---|---|---|---|
| P | 2.5 | 3.3 | 3.5 |
| S | 3.2 | 2.0 | 1.4 |
| Cl | 4.3 | 5.0 | 4.4 |

The BAM certificate contains homogeneity tests using the bulk analytical technique XRF spectrometry (Matschat et al., 2005). In the following, we compare the homogeneity results in our study with the results reported by BAM. The homogeneity test for the certification was carried out using different samples of both BAM glasses. The test portion mass was much higher (several g depending on the element) compared with our microanalytical investigations (µg to lowest ng range). The XRF results indicate that the samples coming from the same raw glass plates are homogeneous with respect to most major elements, except for $K_2O$ that shows significant inhomogeneity and $Al_2O_3$ that shows detectable inhomogeneity to a lesser degree. Our EPMA data are not in agreement with these results. As shown in Figure 2.1, our 500 measurements of both BAM-S005-A and BAM-S005-B show no evidence for a heterogeneous distribution of $K_2O$ and $Al_2O_3$; the RSD values are 1.1% for $Al_2O_3$ in both glasses, 3.1% for $K_2O$ in BAM-S005-A and 3.5% for $K_2O$ in BAM-S005-B, in close agreement with the counting errors of X-ray intensities shown in Table 2.3 (1.0% for $Al_2O_3$ and 3.3% for $K_2O$). We also found a very good agreement between the $K_2O$ and $Al_2O_3$ concentration data by EPMA (better than 2%, Table 2.5) for different splits of both glasses, also indicating that the two major elements could be homogeneously distributed. In addition, other silicate reference glasses, such as NIST SRM series (the EPMA results for the major elements in the NIST SRM 610 and 612 glasses are shown in Table 2.5; Jochum et al., 2011), USGS (Jochum et al., 2005; Guillong et al., 2005), MPI-DING (Jochum et al., 2006) and CGSG (Hu et al., 2011), do not show any inhomogeneities for these two elements, whereas they had similar production protocols as the BAM glasses.

Table 2.5: Major element concentrations (% by mass) determined by EPMA and information values for the BAM glasses. Also shown are the EPMA results for NIST SRM 610 and 612.

| Element | BAM-S005-A EPMA | BAM-S005-B EPMA | BAM Inform.values | NIST SRM 610 EPMA | NIST SRM 612 EPMA |
|---|---|---|---|---|---|
| $SiO_2$ | 70.5 ± 0.3 | 70.5 ± 0.3 | 71 | 69.4 ± 0.2 | 71.7 ± 0.2 |
| $Na_2O$ | 13.5 ± 0.1 | 13.7 ± 0.1 | 13.7 | 13.6 ± 0.1 | 14.0 ± 0.1 |
| CaO | 10.7 ± 0.1 | 10.8 ± 0.1 | 10.5 | 11.59 ± 0.06 | 11.93 ± 0.05 |
| MgO | 2.11 ± 0.04 | 2.14 ± 0.03 | 2.3 | 0.057 ± 0.014 | - |
| $Al_2O_3$ | 1.16 ± 0.01 | 1.18 ± 0.01 | 1.1 | 1.98 ± 0.03 | 2.06 ± 0.02 |
| $K_2O$ | 0.68 ± 0.02 | 0.68 ± 0.02 | 0.7 | 0.048 ± 0.015 | - |
| Total | 98.7 ± 0.5 | 99.0 ± 0.5 | 99.3 | 96.68 ± 0.42 | 99.69 ± 0.37 |

The information values for the BAM glasses were obtained from the certificate (Matschat et al., 2005). The EPMA results for NIST SRM 610 and 612 were taken from Jochum et al. (2011) and were determined under the same analytical conditions as the BAM glass measurements. Uncertainties are 1 standard deviation.

The XRF results given in the certificate indicate that most trace elements are homogeneously distributed in both reference glasses with the exceptions of Cl, Cu, Mo and Zr (strong heterogeneities), Zn and Se (significant heterogeneities) and Pb (weak heterogeneities).

As shown in Figure 2.2, our LA-ICP-MS investigations demonstrated that Cl is heterogeneously distributed in both reference glasses; this is especially obvious for the small spot size (25-45 μm) analyses, where its RSD values were significantly higher than the analytical repeatability of LA-ICP-MS. These findings are in agreement with the XRF results in the certificate. Compared with the significant heterogeneities of Mo, Zr and Se reported by the certificate, only slight possible heterogeneities are detected in BAM-S005-A and/or BAM-S005-B, indicating that greater heterogeneities for these three elements may be present at the bulk scale than at the tablet scale sampled by our microanalytical methods. A weak heterogeneity of Pb was also observed in BAM-S005-A (Figure 2.2b). Despite the heterogeneities reported by XRF, we detected no heterogeneity for Cu and Zn in our study, which may be due to having limited our work to a single sample tablet. Although no heterogeneous distribution for Cs, Cr, Hf, Fe, S or Ni is reported in the certificate, possible heterogeneities were detected in type A and/or B materials by our LA-ICP-MS tests. This may reflect homogeneity for these elements in bulk analysis but possible inhomogeneities at microanalytical scales.

As described previously, the NIST SRM 610 glass was used for calibration in the LA-ICP-MS analyses. Because an inhomogeneous distribution of some trace elements in NIST SRM 610 has been previously reported (e.g. Eggins and Shelley 2002), it seems that this glass is not a universally suitable calibration material for LA-ICP-MS. Jochum et al. (2011) investigated the homogeneity of the NIST SRM 610-617 glasses and demonstrated that inhomogeneities for some siderophile/chalcophile elements (such as Ni, Se, Pd and Pt) are present in all the NIST glasses. On the other hand, the relative uncertainties for the reference values of different trace elements at the 95% confidence level (including errors caused by inhomogeneities) are similar for the NIST 610 and 612 glasses (Jochum et al., 2011), both of which were used for calibration or monitoring the technique reliability in our LA-ICP-MS analyses. Therefore, the NIST SRM 610 glass can be used as a suitable calibration material. Additionally, the same set of trace elements in the NIST SRM 612 glass was also investigated under the same analytical conditions using NIST SRM 610 for the calibration in our study. The LA-ICP-MS results for NIST SRM 612 are shown in Table 2.6, where the trace element concentrations agree well with their reference values reported by

Jochum et al. (2011), implying the utility of NIST SRM 610 for calibration purposes.

Based on the previous discussion, all six major elements and thirty-three of the trace elements are homogeneously distributed in both BAM glasses, even for low test portion masses down to 0.02 µg (25 µm spot size). However, ten trace – mainly chalcophile and siderophile – elements (Cs, Se, Cl, Ni, Mo, Cr, Hf, Pb, Fe and Zr) may be inhomogeneously distributed in the glasses, which could be due to the loss of elements with high volatilities and/or release of material from either the melt crucible (aluminum/zirconium oxide) or heating electrodes (molybdenum) (e.g., NBS 1970; Rocholl et al., 1997). Both XRF and microanalytical data demonstrate that Cl, Mo, Zr, Se and Pb are heterogeneously distributed to different degrees at test portion masses in the µg to g range. Microanalytical inhomogeneities were also detected for Cs, Ni, Cr, Hf and Fe at low test portion masses of 0.02 – 1.5 µg corresponding to crater sizes of 25 – 95 µm. However, at larger test portion masses of 0.5 – 1.5 µg (55 – 95 µm crater sizes), most inhomogeneities of these elements were not detected by LA-ICP-MS. The inhomogeneity of S in both BAM glasses is still unclear up to now. These findings are in agreement with homogeneity tests of other reference glasses (Jochum et al., 2006; Jochum et al., 2011; Hu et al., 2011), where some chalcophile and siderophile elements are also heterogeneously distributed. Some of our results differ from the XRF data reported by the certificate, where significant heterogeneities for Cu and Zn are observed at test portion masses of several grams.

Table 2.6: Summary of composition data for trace elements in both BAM glasses.

| Element | Measured isotopes | DL | DL | BAM-S005-A SIMS | | BAM-S005-A LA-ICP-MS | | | BAM-S005-A certified | | BAM-S005-B SIMS | | BAM-S005-B LA-ICP-MS | | | BAM-S005-B certified | | NIST SRM 612 LA-ICP-MS | | | NIST SRM 612 reference | |
|---|---|---|---|---|---|---|---|---|---|---|---|---|---|---|---|---|---|---|---|---|---|---|
| | | UP-193/95 µm | UP-213/55 µm | conc | *s* | conc | *s* | *U* | conc | *U* | conc | *s* | conc | *s* | *U* | conc | *U* | conc | *s* | *U* | conc | *U* |
| As | $^{75}$As | 0.6 | 0.2 | - | - | 94.8 | 4.2 | 12.1 | 100 | 8 | - | - | 95.8 | 6.2 | 12.5 | 100 | 8 | 35.4 | 2.1 | 4.6 | 35.7 | 5.5 |
| Ba | $^{137}$Ba | 0.1 | 0.03 | - | - | 116 | 4 | 8 | 103 | 9 | - | - | 110 | 3 | 8 | 103 | 5 | 40.9 | 1.1 | 3.0 | 39.3 | 0.9 |
| Cd | $^{111}$Cd | 0.5 | 0.4 | - | - | 54.8 | 2.9 | 10.0 | 54.3 | 3.5 | - | - | 54.2 | 5.7 | 9.9 | 54.3 | 2.6 | 30.3 | 1.8 | 5.5 | 28.1 | 1.1 |
| Ce | $^{140}$Ce | 0.01 | 0.004 | - | - | 95.9 | 2.6 | 6.8 | 85.5 | 4.9 | - | - | 93.7 | 2.3 | 7.2 | 85.5 | 4.1 | 40.3 | 1.6 | 3.0 | 38.4 | 0.7 |
| Cl | $^{35}$Cl | 30 | 140 | 206 | 10 | 303 | 46 | 165 | 247 | 33 | 214 | 10 | 272 | 20 | 145 | 247 | 24 | 221 | 35 | 111 | 142 | 58 |
| Co | $^{59}$Co | 0.4 | 0.04 | - | - | 41.9 | 0.9 | 3.0 | 38.9 | 2.4 | - | - | 42 | 2 | 3 | 38.9 | 2.3 | 36.5 | 1.5 | 2.7 | 35.5 | 1.0 |
| Cr | $^{53}$Cr | 1 | 0.7 | - | - | 11.0 | 0.5 | 0.8 | 10.7 | 2.4 | - | - | 11.2 | 0.8 | 0.9 | 10.4 | 1.2 | 37.6 | 1.0 | 2.8 | 36.4 | 1.7 |
| Cs | $^{133}$Cs | 0.03 | 0.02 | - | - | 0.029 | 0.006 | 0.006 | - | - | - | - | 0.030 | 0.009 | 0.007 | - | - | 45.2 | 2.6 | 3.6 | 42.7 | 1.8 |
| Cu | $^{63}$Cu | 0.2 | 0.1 | - | - | 95.9 | 4.3 | 8.4 | 89.5 | 4.0 | - | - | 96.3 | 4.3 | 8.5 | 89.5 | 3.2 | 41.1 | 2.6 | 3.7 | 37.8 | 1.5 |
| Dy | $^{163}$Dy | 0.02 | 0.005 | - | - | 0.26 | 0.02 | 0.02 | - | - | - | - | 0.25 | 0.02 | 0.02 | - | - | 35.9 | 1.1 | 2.9 | 35.5 | 0.7 |
| Er | $^{167}$Er | 0.02 | 0.009 | - | - | 0.31 | 0.02 | 0.03 | - | - | - | - | 0.29 | 0.02 | 0.03 | - | - | 38.4 | 1.2 | 3.4 | 38.0 | 0.9 |
| Eu | $^{151}$Eu | 0.01 | 0.003 | - | - | 0.020 | 0.003 | 0.002 | - | - | - | - | 0.020 | 0.003 | 0.002 | - | - | 37.3 | 0.9 | 3.1 | 35.6 | 0.8 |
| Fe | $^{57}$Fe | 20 | 7 | - | - | 288 | 8 | 19 | 295 | 11 | - | - | 308 | 13 | 23 | 295 | 10 | 50.6 | 3.4 | 3.6 | 51 | 2 |
| Gd | $^{157}$Gd | 0.06 | 0.02 | - | - | 0.14 | 0.02 | 0.01 | - | - | - | - | 0.14 | 0.02 | 0.01 | - | - | 38.2 | 0.9 | 3.1 | 37.3 | 0.9 |
| Hf | $^{178}$Hf | 0.007 | 0.003 | - | - | 16.5 | 1.0 | 1.4 | - | - | - | - | 15.3 | 0.7 | 1.3 | - | - | 37.5 | 1.3 | 3.2 | 36.7 | 1.2 |
| Ho | $^{165}$Ho | 0.009 | 0.003 | - | - | 0.079 | 0.006 | 0.007 | - | - | - | - | 0.074 | 0.006 | 0.006 | - | - | 40.6 | 1.5 | 3.4 | 38.3 | 0.8 |
| La | $^{139}$La | 0.01 | 0.009 | - | - | 0.57 | 0.04 | 0.04 | - | - | - | - | 0.56 | 0.01 | 0.04 | - | - | 37.5 | 1.3 | 2.9 | 36.0 | 0.7 |
| Lu | $^{175}$Lu | 0.008 | 0.003 | - | - | 0.100 | 0.008 | 0.008 | - | - | - | - | 0.091 | 0.007 | 0.007 | - | - | 40.0 | 2.2 | 3.1 | 37.0 | 0.9 |
| Mn | $^{55}$Mn | 0.3 | 0.2 | - | - | 96 | 3 | 8 | 96 | 5 | - | - | 98 | 4 | 8 | 96 | 5 | 39.1 | 0.7 | 3.1 | 38.7 | 0.9 |
| Mo | $^{95}$Mo | 0.2 | 0.02 | - | - | 237 | 14 | 30 | 229 | 12 | - | - | 227 | 12 | 29 | 229 | 12 | 38.1 | 1.7 | 4.8 | 37.4 | 1.7 |
| Nb | $^{93}$Nb | 0.02 | 0.009 | - | - | 0.33 | 0.01 | 0.05 | - | - | - | - | 0.33 | 0.01 | 0.05 | - | - | 39.1 | 0.9 | 6.2 | 38.9 | 2.1 |
| Nd | $^{146}$Nd | 0.01 | 0.01 | - | - | 0.45 | 0.02 | 0.03 | - | - | - | - | 0.45 | 0.02 | 0.03 | - | - | 35.9 | 0.7 | 2.5 | 35.5 | 0.7 |
| Ni | $^{61}$Ni | 10 | 4 | - | - | 49.6 | 2.4 | 2.9 | 46.4 | 1.6 | - | - | 50.9 | 3.4 | 3.0 | 46.4 | 1.9 | 40.6 | 2.2 | 2.4 | 38.8 | 3.7 |
| P | $^{31}$P$^{-}$ | - | - | 9.3 | 0.3 | - | | - | - | - | 9.2 | 0.3 | - | - | - | - | - | - | - | - | - | - |
| Pb | $^{208}$Pb | 0.03 | 0.01 | - | - | 213 | 9 | 15 | 188 | 8 | - | - | 219 | 14 | 15 | 188 | 7 | 44.6 | 3.4 | 3.2 | 38.57 | 0.20 |
| Pr | $^{141}$Pr | 0.006 | 0.003 | - | - | 0.123 | 0.006 | 0.008 | - | - | - | - | 0.120 | 0.009 | 0.009 | - | - | 39.8 | 1.2 | 2.7 | 37.9 | 1.0 |
| Rb | $^{85}$Rb | 0.1 | 0.03 | - | - | 0.44 | 0.02 | 0.02 | - | - | - | - | 0.45 | 0.02 | 0.03 | - | - | 33.0 | 1.2 | 2.0 | 31.4 | 0.4 |
| S | $^{34}$S | 100 | 60 | 782 | 16 | 782 | 32 | 103 | 778 | 85 | 801 | 11 | 757 | 30 | 96 | 778 | 57 | 380 | 30 | 50 | 377 | 85 |
| Sb | $^{121}$Sb | 0.2 | 0.05 | - | - | 107 | 4 | 12 | 110 | 7 | - | - | 105 | 6 | 12 | 110 | 6 | 35.7 | 2.7 | 4.1 | 34.7 | 1.8 |
| Se | $^{77}$Se | 1 | 0.9 | - | - | 17.6 | 2.4 | 10.8 | 19.6 | 1.7 | - | - | 18.1 | 1.5 | 11.1 | 19.6 | 1.2 | 17.9 | 0.9 | 10.9 | 16.3 | 2.7 |
| Sm | $^{147}$Sm | 0.04 | 0.03 | - | - | 0.103 | 0.011 | 0.008 | - | - | - | - | 0.105 | 0.012 | 0.008 | - | - | 38.1 | 0.7 | 3.0 | 37.7 | 0.8 |
| Sn | $^{119}$Sn | 0.2 | 0.1 | - | - | 75.3 | 3.4 | 11.0 | 78.8 | 5.5 | - | - | 74.6 | 3.3 | 11.0 | 78.8 | 5.5 | 39.8 | 1.9 | 5.9 | 38.6 | 1.3 |
| Sr | $^{88}$Sr | 0.06 | 0.02 | - | - | 144 | 2 | 9 | 128 | 7 | - | - | 144 | 3 | 9 | 128 | 7 | 79.9 | 1.4 | 4.8 | 78.4 | 0.2 |
| Ta | $^{181}$Ta | 0.02 | 0.004 | - | - | 0.034 | 0.005 | 0.006 | - | - | - | - | 0.032 | 0.005 | 0.005 | - | - | 40.3 | 2.5 | 6.5 | 37.6 | 1.9 |
| Tb | $^{159}$Tb | 0.007 | 0.004 | - | - | 0.031 | 0.003 | 0.002 | - | - | - | - | 0.030 | 0.003 | 0.002 | - | - | 39.3 | 1.3 | 3.0 | 37.6 | 1.1 |

Table 2.6: Summary of composition data for trace elements in both BAM glasses.

| Element | Measured isotopes | DL | DL | BAM-S005-A SIMS | | BAM-S005-A LA-ICP-MS | | | BAM-S005-A certified | | BAM-S005-B SIMS | | BAM-S005-B LA-ICP-MS | | | BAM-S005-B certified | | NIST SRM 612 LA-ICP-MS | | | NIST SRM 612 reference | |
|---|---|---|---|---|---|---|---|---|---|---|---|---|---|---|---|---|---|---|---|---|---|---|
| | | UP-193/95 µm | UP-213/55 µm | conc | *s* | conc | *s* | *U* | conc | *U* | conc | *s* | conc | *s* | *U* | conc | *U* | conc | *s* | *U* | conc | *U* |
| Th | $^{232}$Th | 0.007 | 0.001 | - | - | 0.45 | 0.03 | 0.03 | - | - | - | - | 0.42 | 0.02 | 0.03 | - | - | 41.4 | 1.4 | 2.8 | 37.79 | 0.08 |
| Ti | $^{47}$Ti | 5 | 2 | - | - | 101 | 1 | 7 | 98.3 | 5.4 | - | - | 102 | 3 | 8 | 97.7 | 4.2 | 41.2 | 1.2 | 3.0 | 44.0 | 2.3 |
| Tm | $^{169}$Tm | 0.01 | 0.003 | - | - | 0.061 | 0.005 | 0.005 | - | - | - | - | 0.056 | 0.005 | 0.005 | - | - | 39.7 | 1.8 | 3.2 | 36.8 | 0.6 |
| U | $^{238}$U | 0.005 | 0.0007 | - | - | 0.60 | 0.03 | 0.04 | - | - | - | - | 0.56 | 0.04 | 0.04 | - | - | 42.5 | 2.1 | 3.0 | 37.38 | 0.08 |
| V | $^{51}$V | 0.06 | 0.03 | - | - | 192 | 9 | 14 | 196 | 22 | - | - | 195 | 10 | 15 | 196 | 22 | 39.0 | 1.0 | 2.8 | 38.8 | 1.2 |
| Y | $^{89}$Y | 0.02 | 0.01 | - | - | 2.18 | 0.10 | 0.16 | - | - | - | - | 2.10 | 0.09 | 0.16 | - | - | 38.1 | 1.0 | 2.9 | 38.3 | 1.4 |
| Yb | $^{173}$Yb | 0.02 | 0.005 | - | - | 0.47 | 0.04 | 0.03 | - | - | - | - | 0.44 | 0.03 | 0.03 | - | - | 38.3 | 1.2 | 2.8 | 39.2 | 0.9 |
| Zn | $^{67}$Zn | 3 | 2 | - | - | 158 | 11 | 17 | 163 | 10 | - | - | 157 | 14 | 17 | 163 | 6 | 41.3 | 2.9 | 4.6 | 39.1 | 1.7 |
| Zr | $^{90}$Zr | 0.06 | 0.02 | - | - | 660 | 24 | 46 | 623 | 125 | - | - | 634 | 32 | 47 | 623 | 76 | 38.2 | 0.9 | 2.7 | 37.9 | 1.2 |

The units are µg g-1. Detection limits (DL) for LA-ICP-MS (using UP-193SS at 95 µm spot size and UP-213 at 55 µm spot size), concentrations (conc), standard deviations (s) and expanded uncertainties (U) are indicated. For the twenty-two trace elements underlined, certified reference values are available, while for the other twenty-two trace elements, concentrations are not certified. The certified values were obtained from the certificate (Matschat et al. 2005). The reference values of NIST SRM 612 were derived from Jochum et al. (2011). The SIMS concentrations were derived from the averages of the SIMS data. The LA-ICP-MS concentrations were derived from the averages of the LA-ICP-MS data at large spot sizes (95 and 55 µm spot sizes for BAM-S005-A, 75 and 55 µm spot sizes for BAM-S005-B).

## 2.4 Quantitative data

Major elements: In addition to the investigation of homogeneity, we also determined the element concentrations in BAM-S005-A and BAM-S005-B. Table 2.5 lists the major element composition of the BAM glasses obtained by EPMA together with the information values in the certificate, as derived by XRF. Our EPMA results of type A and B materials agree very well with each other. They are also in good agreement with the information values of the certificate, with the exception of MgO, where our results were slightly lower than the information value.

Trace elements: Table 2.6 lists our LA-ICP-MS and SIMS results for forty-four trace elements. It also includes the certified values for twenty-two elements (Matschat et al., 2005). The LA-ICP-MS concentrations were calculated from the data obtained at large crater sizes (55-95 µm). Our data are accompanied with standard deviations (SD) and the expanded uncertainties containing all identified sources of errors.

The expanded uncertainty of the certified values was calculated according to the Guide to the Expression of Uncertainty in Measurements (GUM 1995) with a coverage factor 2, which is described in detail in the certificate (Matschat et al., 2005). The expanded uncertainty $U$ of our LA-ICP-MS result for an element was calculated by the following equation using the IAG protocol (Kane et al., 2003):

$$U = k\sqrt{u_{BAM-meas}^2 + u_{BAM-Ca}^2 + u_{610-meas}^2 + u_{610-ref}^2 + u_{610-Ca}^2 + u_{in}^2}$$

where the coverage factor $k$ was 2; $u_{\text{BAM-meas}}$ and $u_{610\text{-meas}}$ are the uncertainties of the measurements of the sample and the calibration material NIST SRM 610, respectively; $u_{\text{BAM-Ca}}$ is the uncertainty of the internal standard element Ca of the BAM glasses; $u_{610\text{-ref}}$ and $u_{610\text{-Ca}}$ are the uncertainties of the element of interest and of Ca at the 95% confidence level of the NIST SRM 610 glass (Jochum et al., 2011); $u_{\text{in}}$ is the uncertainty caused by the possible inhomogeneous distribution of the element. Figure 2.2 indicates that most trace elements are homogeneously distributed at 55-95 µm scales (within the repeatability field), for these elements we assume $u_{\text{in}} = 0$. For the elements with possible heterogeneities in type A and/or B materials, we assume $u_{\text{in}}$ values of 10% of the mean concentration value for Cs, 1 % of the mean value for Mo and 10% of the mean value for Cl, as determined by the repeatability of the measurement.

Certified concentrations: Twenty-two trace elements have been certified in BAM-S005-A and B for bulk analytical purposes (Matschat et al., 2005). The percentage deviations of our LA-ICP-MS data from the certified values are shown in Figure 2.4. For most elements, the deviations of our results were within the

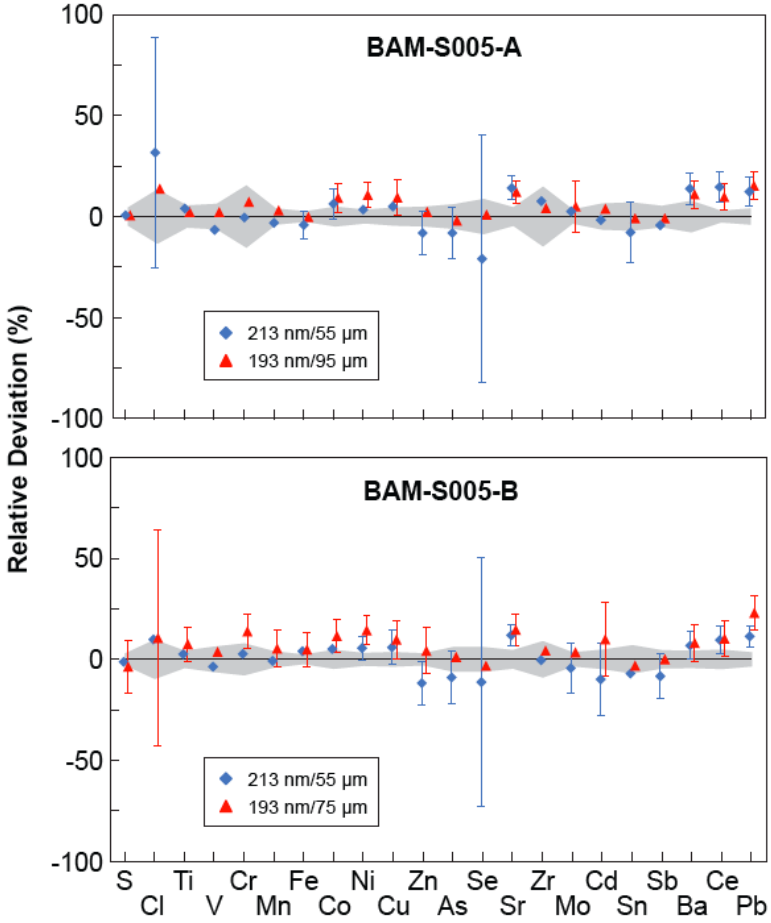


Figure 2.4: Relative deviations of LA-ICP-MS data from the certified values in both BAM glasses. The shaded field refers to the expanded uncertainty range of the certified values. Error bars (the expanded uncertainties of LA-ICP-MS results) for the points outside the shaded field are shown.

uncertainty ranges of the certified values, indicating the reliability of the LA-ICP-MS data. This is because the calibration material (NIST SRM 610) has a matrix similar to the BAM glasses, which significantly decreases the risk of systematic matrix effects of LA-ICP-MS, and the reference values for NIST SRM 610 from Jochum et al. (2011) have small assigned uncertainties. However, there were four exceptions (Sr, Ba, Ce and Pb) in both glasses with significant deviations of about 10%. To test whether these discrepancies were caused by analytical

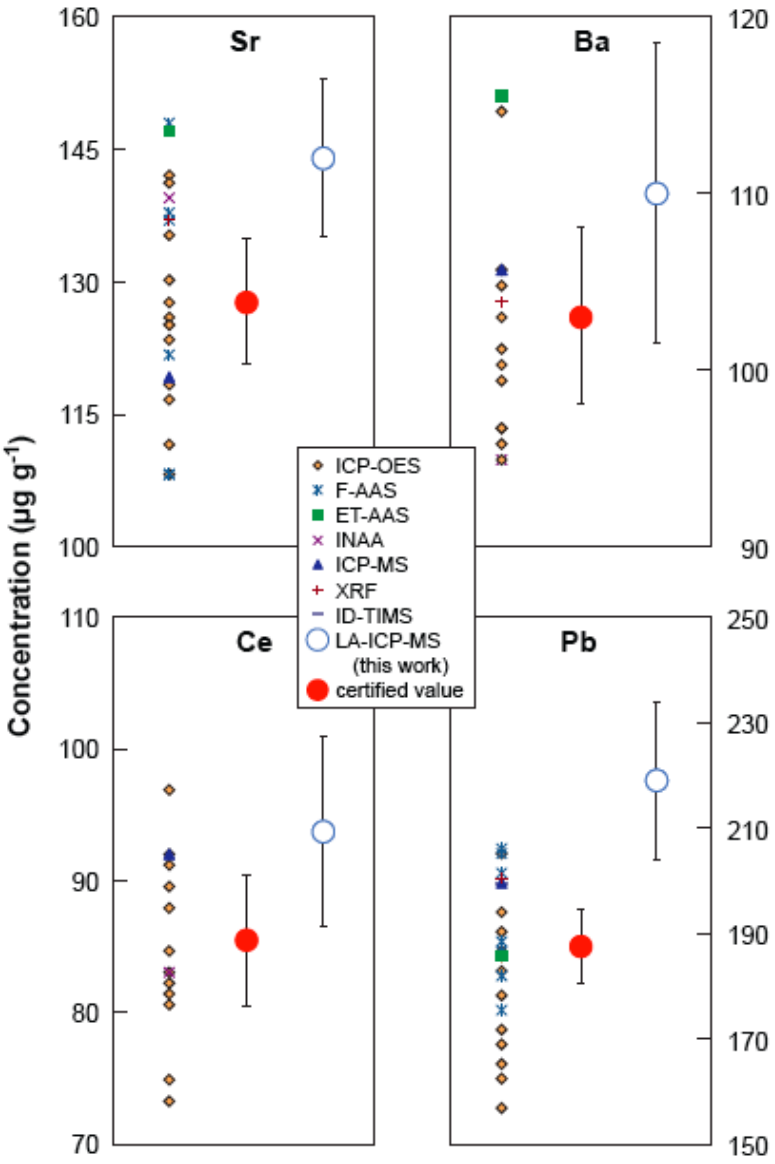


Figure 2.5: Comparison of the LA-ICP-MS data for Sr, Ba, Ce and Pb in the BAM-S005-B glass with their certified values and individual concentration values derived from different analytical techniques used for certification. Error bars refer to the expanded uncertainties.

problems, we compared our results (see Figure 2.5) with the concentration values derived from different analytical techniques used for the certification, such as flame atomic absorption spectrometry (FAAS), atomic absorption spectrometry with electrothermal atomization (ET AAS), instrumental neutron activation analysis (INAA), isotope dilution with thermal ionization mass spectrometry (ID-TIMS) and ICP-optical emission spectrometry (ICP-OES). Because the two BAM glasses are essentially identical in composition, the

comparison for the four elements was only carried out for the BAM-S005-B glass. As shown in Figure 2.5, our mean LA-ICP-MS values were systematically higher than the certified values, but within the concentration ranges obtained from different analytical techniques. Since our results were calibrated using recently derived reference values for NIST SRM 610 based on low uncertainty isotope dilution (ID) data (Jochum et al., 2011), we are confident that our mean values are of good quality and the certified values may be biased by low ICP-OES values. The concentrations of S and Cl were also investigated by SIMS (shown in Table 2.6). The SIMS results for S agreed well with the certified values and LA-ICP-MS data for both BAM glasses. However, the SIMS determined Cl values were consistently low, the meaning of which remains unclear.

Other trace element data: Table 2.6 also lists the concentrations of twenty-two trace elements for both glasses, which are not certified. These values were obtained by only one method (the P concentration was obtained by SIMS and the concentrations of other twenty-one elements were determined by LA-ICP-MS), and thus should be used as information values only. However, as mentioned earlier, they have a high level of confidence because of matrix-matched calibration. The reliability of the concentration data for these elements may also be demonstrated by the chondrite normalized rare earth element (REE) patterns (except doped Ce), which show smooth curves for the light and heavy REE elements, and the Y/Ho abundance ratios which are very close to the chondritic values. As described in the certificate (Matschat et al., 2005), none of the REE elements except Ce were added to the glass batch when producing the BAM glasses. Therefore, the REE elements (except Ce) are most likely present as trace elements (contaminants) in the raw materials used for the glass production, such as the main components like $SiO_2$ and/or the doped chemicals. Natural abundance patterns for the REE elements can therefore be assumed.

Additionally, the concentration data for all the trace elements of both BAM glasses (Table 2.6) agreed very well and were consistent with an identical composition of both materials. The relative standard deviations of the concentration data were about 1-30%, while the relative expanded uncertainties, which include all the possible uncertainties caused in the LA-ICP-MS measurements (as described above) were higher (about 6-61%).

## 2.5 Conclusions

We tested the homogeneity of the BAM-S005-A and BAM-S005-B reference glasses with respect to major and forty-four trace elements using EPMA, LA-ICP-MS and SIMS analyses. The results indicate that all major and thirty-three trace elements are homogeneously distributed at the μm scale. Some elements, such as Cs, Se, Cl, Ni, Mo, Cr, Hf, Pb, Fe and Zr, may be heterogeneously distributed at the cm and/or μm scales. The inhomogeneity of S in the two materials is still unclear. Both BAM glasses can, therefore, be used as reference glasses for bulk and microanalytical purposes. Further investigations are needed to clarify some discrepancies between the homogeneity results reported in the certificate and this work. The EPMA data of the major elements in our study agree with the information values in the certificate. With the exception of the elements Sr, Ba, Ce and Pb, our LA-ICP-MS data for eighteen trace elements (As, Cd, Cl, Co, Cr, Cu, Fe, Mn, Mo, Ni, Sb, Se, Sn, S, Ti, V, Zn and Zr) were within the uncertainties of the certified concentrations, indicating the good quality of our LA-ICP-MS data. We present new data for the trace elements P, Rb, Y, Nb, Cs, La, Pr, Nd, Sm, Eu, Gd, Tb, Dy, Ho, Er, Tm, Yb, Lu, Hf, Ta, Th and U, which will be useful for the use of the BAM glasses as microanalytical reference glasses. Additionally, the BAM glasses are especially suitable for calibration purposes for the determination of trace elements, such as As, Cd, Sb, Se and Zn, with lower uncertainties than those of the NIST glasses.

## Acknowledgements

We thank three anonymous reviewers and the Editor Jon D. Woodhead for their helpful comments, and also thank the Max Planck Graduate Center in Mainz, Germany for financial support.

# Chapter 3

# Trace element variability in single ostracod valves as a proxy for hydrochemical change in Nam Co, central Tibet, during the Holocene

This chapter is published as Yang Q, Jochum KP, Stoll B, Weis U, Börner N, Schwalb A, Frenzel P, Scholz D, Doberschütz S, Haberzettl T, Gleixner G, Mäusbacher R, Zhu L and Andreae MO (2014) Palaeogeography, Palaeoclimatology, Palaeoecology 399, 225-235.

## 3.1 Introduction

The Tibetan Plateau (TP), situated in the interaction zone of the Westerlies, the Indian Ocean Summer Monsoon (IOSM), the East Asian Summer Monsoon (EASM) and the polar air current, responds sensitively to global climate changes (An, 2000) and has been little influenced by human activities during the Holocene. Over the last several decades, numerous studies on lacustrine sediments from different sites on the TP have been performed in order to reconstruct local paleoclimate changes at different time scales (Gasse et al., 1991, 1996; Lister et al., 1991; Gu et al., 1993; Shen et al., 2005; Herzschuh et al., 2006; Wu et al., 2006; Zhu et al., 2009; Kramer et al., 2010 a, b). Lake Nam Co, the second largest lake on the TP, has recently received increasing attention. Paleoenvironmental changes at Nam Co during different time intervals of the Holocene have been reconstructed based on sedimentological, geochemical and microfossil analyses on several sediment cores (Figure 3.1) retrieved from this lake [covering the last ~8.4 ka by Li et al. (2008b) and Zhu et al. (2008); ~7.2 ka by Mügler et al. (2010); ~4.0 ka by Kasper et al. (2012, 2013); ~11.3 ka by Doberschütz et al. (2013)]. These studies indicate that the Nam Co region is primarily influenced by the IOSM, which induced generally warm and wet conditions from the early- to mid-Holocene and an enhanced drying tendency afterward in this area.

Ostracod shells, composed of low-Mg calcite, have been demonstrated to be a useful archive in paleohydrologic and paleoclimatic studies (Holmes, 1996; Xia et al., 1997b; Ito et al., 2003; Schwalb, 2003; Ito and Forester, 2009; Van der

Meeren et al., 2011). Trace element ratios (e.g., Mg/Ca and Sr/Ca) and stable isotope values ($\delta^{18}O$ and $\delta^{13}C$) in ostracod calcite have been widely used as proxies for paleosalinity and paleotemperature in lacustrine environments (Griffiths and Holmes, 2000). For the TP, ostracod species assemblages, $\delta^{18}O$ and $\delta^{13}C$ values have been used to track past lake level changes (Lister et al., 1991; Van Campo and Gasse, 1993; Mischke et al., 2008, 2010; Xie et al., 2009; Wrozyna et al., 2010, 2012). Transfer functions based on ostracod species composition have been established to estimate paleo-water electrical conductivity and depth in the lacustrine systems (Mischke et al., 2007, 2010; Wrozyna et al., 2009a; Frenzel et al., 2010; Kasper et al., 2013). However, trace element ratios in ostracod shells have rarely been used for paleoenvironmental studies in this area.

In our study, three ostracod taxa, i.e., *Leucocytherella sinensis*, ?*Leucocythere dorsotuberosa* f. *typica* and ?*Leucocythere dorsotuberosa* f. *postilirata*, were selected from both sediment cores Nam Co 8 and NC 08/01 from Lake Nam Co (Figure 3.1). All three taxa are endemic to the TP and adjacent areas and tolerate cold and saline aquatic environments (Huang et al., 1985; Zhang et al., 2006a; Wrozyna et al., 2009a). Shell sizes are generally less than 1 mm (Wrozyna et al., 2009b). As a cold-stenothermal species, *L. sinensis* is reported from lakes on the TP with water salinity up to 13‰ (Huang et al., 1985) and is also the most abundant ostracod species at Nam Co (Wrozyna et al., 2009b). The species ?*L. dorsotuberosa* lives in waters with slightly elevated salinities (Wrozyna et al., 2009a). ?*L. dorsotuberosa* f. *postilirata*, which is considered as a morphotype of ?*L. dorsotuberosa*, occurs in waters below the thermocline and increases in abundance and dominance with water depth (Wrozyna et al., 2009b). Due to the lack of previous analyses on these taxa, the information about elemental composition in their shells is still limited. Here we determined concentrations of a set of trace elements and present molar ratios of Mg/Ca, Sr/Ca, Ba/Ca, U/Ca and La/Ca in the single shells, as proxies for past hydrologic and hydrochemical changes in the lake system.

## 3.2 Material and methods

### 3.2.1 Study area

Lake Nam Co (90°16′-91°03′E, 30°30′-30°55′N; 4718 m a.s.l.), located on the southern-central TP (Figure 3.1), is the second largest and highest saline lake in China (Mügler et al., 2010). Its surface area is 2015 km² (Zhu et al., 2010b) and its maximum water depth is ca. 100 m (Wang and Zhu, 2006). The catchment

area of 10,610 km² (Zhu et al., 2010b) is surrounded by the Northern Tibetan Plateau hills in the north, the Nyainqentanglha Mountain Range in the southeast (Figure 3.1), and the Gandise Range in the south (Mügler et al., 2010), forming a closed basin. Lake Nam Co has no outflow, and its water balance is, thus, mainly controlled by precipitation, evaporation, the input of melt water and ground water. The climate of the region is semi-arid to semi-humid continental (Feng et al., 2006). The current mean annual precipitation in the lake area is about 280 mm, whereas the mean annual evaporation is approximately 790 mm for the lake zone and 320 mm for the terrestrial basin (Zhu and Meng, 2004; Wang and Zhu, 2006; Li et al., 2008b; Daut et al., 2010). The mean annual temperature is around 0 °C, with monthly average temperature ranging from -10 to 9 °C (You et al., 2006). The dominating cations in the surface water are $Na^+$ and $Mg^{2+}$, and the primary anions are $HCO_3^-$ and $SO_4^{2-}$ (Zhang et al., 2006b). The lake water is alkaline (pH 9.4) and slightly saline with a salinity of 1.3-2.9 g $l^{-1}$ (Wang and Zhu, 2006).

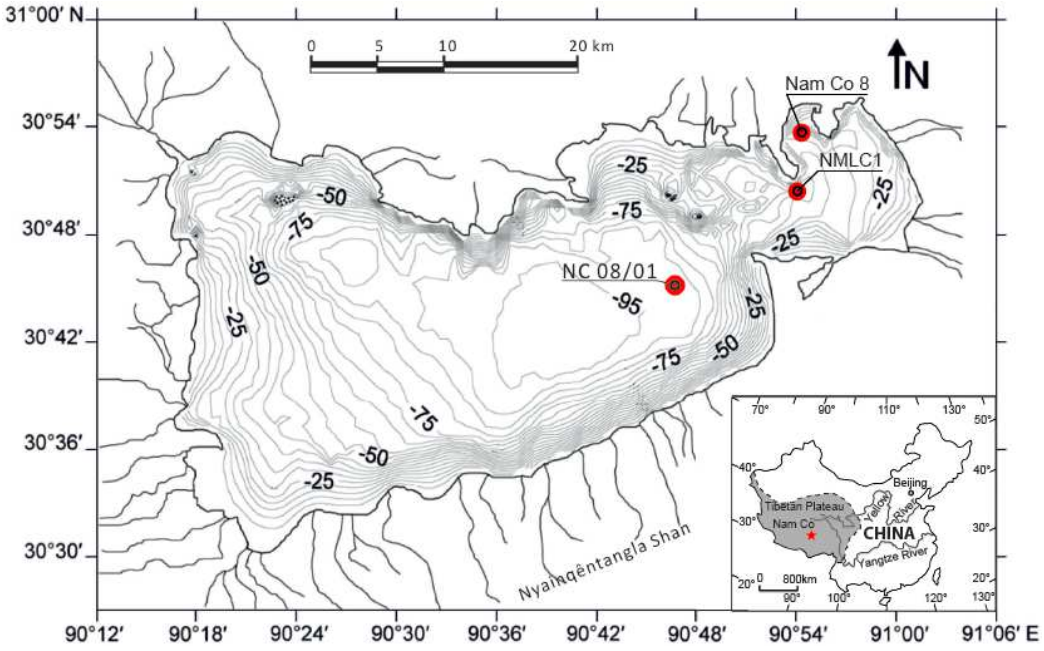


Figure 3.1: Location of Lake Nam Co in China (inset) and bathymetric map of this lake. The red dots show the core locations of NC 08/01 (Kasper et al., 2012, 2013; Doberschütz et al., 2013), Nam Co 8 (Mügler et al., 2010) and NMLC1 (Li et al., 2008b; Zhu et al., 2008), respectively (modified from Shen et al., 2005 and Kasper et al., 2012).

The Nam Co basin is located in the centre of the Lhasa block, which was accreted during the late Jurassic to the early Cretaceous (Zhu and Meng, 2004;

Kapp et al., 2005). Cretaceous-Permian granitoids and orthogneisses are exposed in the northern, southern and southeastern part of the Nam Co basin, together with Paleozoic to Cretaceous metasediments, Cretaceous red sandstones, mudstones and conglomerates. Limestone, sandstone, gabbro, greenschist and amphibolite are observed in the western part of the basin (Zhu and Meng, 2004; Kapp et al., 2005). The soils around this region mainly originate from the weathering of the surface crust. In the presence of river inflows, alpine meadows develop on the southern bank under more humid conditions, whereas arid grasslands dominate the northern lake shore (Gao, 1985). Human activities are reported to be very limited in the Nam Co area, and thus the evolution of the lake system is mainly driven by climatic changes (Zhu et al., 2008, 2010a; Xie et al., 2009; Mügler et al., 2010).

## 3.2.2 Sampling

Sediment core Nam Co 8, with a length of 2.7 m, was taken in the northern part of the eastern sub-basin of Lake Nam Co (Figure 3.1) at a water depth of 31 m (Mügler et al., 2010; Wrozyna et al., 2012), while the sediment core NC 08/01, with a length of 10.4 m, was collected in the eastern part (Figure 3.1) at a depth of 93 m (Kasper et al., 2012; Doberschütz et al., 2013). Both cores were sampled at 1 cm intervals. Approximately 5-10 g of wet sediment from each subsample was washed using deionized water with sodium bicarbonate (NaHCO3) and hydrogen peroxide (H2O2; 5%). The disintegrated sediment was sieved over a mesh of 200 μm. The sieve residue was then processed using deionized water in order to avoid carbonate precipitation and air-dried.

Ostracod valves were picked from the sieve residue with a fine brush under a low magnification stereoscopic microscope. Identification of valves was performed based on the detailed description by Wrozyna et al. (2009b). Adult valves were picked and then cleaned in deionized water. All picked valves were generally well preserved and hyaline. No dissolution evidence or clearly visible coating was observed on them. In total, 45 valves (i.e., 33 valves for *L. sinensis,* 4 valves for ?*L. dorsotuberosa* f. *typica* and 8 valves for ?*L. dorsotuberosa* f. *postilirata*) were obtained from different depths of the top 2.4 m of NC 08/01. Seventeen valves of *L. sinensis* were obtained from eight different depths (2 or 3 valves for each depth) of the top 2.6 m of Nam Co 8. The valves were cleaned manually using fine brushes under deionized water mixed with about 5% $H_2O_2$ to remove detrital material and organic matter. After cleaning, the valves were dried and then fixed on glass slides using epoxy for LA-ICP-MS analysis.

### 3.2.3 LA-ICP-MS analysis of single valves

The concentrations of a set of trace elements (i.e., Mg, Sr, Ba, U and the REEs) in single valves were determined using the high-resolution sector-field ICP-MS Thermo Element2 combined with the 213 nm (UP-213) Nd:YAG laser ablation system from New Wave at the Max Planck Institute for Chemistry (MPI), Mainz (Jochum et al., 2007). Ablation was performed in a helium atmosphere, which was mixed with the argon carrier gas prior to the plasma torch. Two measuring techniques, spot and line-scan analyses, were applied in our study. Spot analysis was performed using crater sizes of 80-100 µm and a repetition rate of 5 Hz. Three to six craters were carried out for each sample. Line-scan analysis was performed using an 80 µm crater size with a high scan speed of 80 µm $s^{-1}$ at an energy density of 4.5 J $cm^{-2}$ and a repetition rate of 5 Hz across the surface of a single shell (Figure 3.2). Generally 2-4 runs were performed for each spot analysis and 5-8 runs for each line-scan measurement. We assume that the mean value of all the runs performed on a shell is representative of the composition of the whole specimen. In total, 31 shells from NC 08/01 were measured by the line-scan method, while the other 14 shells from this core and all shells from Nam Co 8 were investigated using spot analysis.

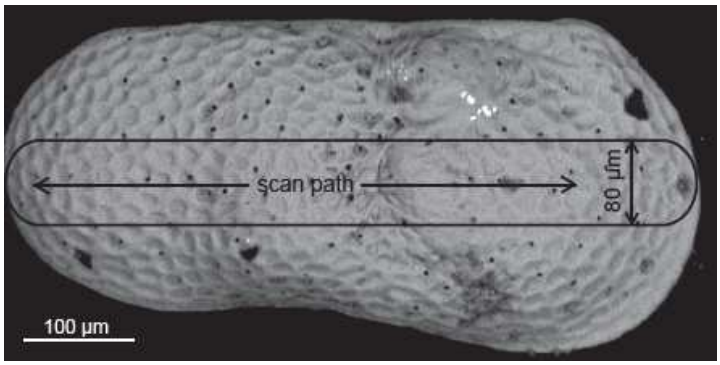


Figure 3.2: Location for a line-scan analysis on a single ostracod shell of *L. sinensis* (80 µm crater size, 80 µm $s^{-1}$ scan speed).

The isotopes measured, i.e., $^{25}Mg$, $^{86}Sr$, $^{137}Ba$, $^{238}U$, $^{139}La$, $^{140}Ce$, $^{141}Pr$, $^{146}Nd$, $^{147}Sm$, $^{151}Eu$, $^{157}Gd$, $^{159}Tb$, $^{163}Dy$, $^{165}Ho$, $^{167}Er$, $^{169}Tm$, $^{174}Yb$ and $^{175}Lu$, are interference-free as demonstrated by Jochum et al. (2012) performing experiments using medium-mass resolution ($m/\Delta m$ = 4000). In this study, all analyses were carried out in the low-mass resolution mode ($m/\Delta m$ = 300) of the mass spectrometer, using a combination of electrical and magnetic scan modes. The operating parameters for the ICP-MS are listed in Table 3.1. Tuning of the ICP-MS (including Ar and He gas flows, torch position and focusing potentials)

was performed using the NIST SRM 612 reference glass to obtain stable ion beam intensities and low oxide formation (ThO/Th < 0.5%) at maximum compatible transmission. Data reduction was carried out by calculating the blank-corrected count rates of the analysed isotopes relative to the internal standard ($^{43}$Ca). EPMA (electron probe microanalysis) was used to determine the Ca concentration in ostracod calcite. The results suggest a uniform Ca abundance in the ostracod shells with an average value of 39% (*m/m*). The silicate reference glass NIST SRM 612 and carbonate reference material MACS-3 were used for external calibration (Jochum et al., 2011, 2012). The silicate reference glass has a matrix different from ostracod calcite, but Jochum et al. (2012) demonstrated that the matrix effect for lithophile refractory elements, such as Ca, Sr, Ba, REEs, U and Th, in ostracod calcite is insignificant for LA-ICP-MS analysis when using a 213 nm laser ablation system.

Table 3.1: Operating parameters of the Element2 ICP-MS.

| | |
|---|---|
| RF power (W) | 1180 |
| Cooling gas flow rate (l min$^{-1}$) | 16 |
| Carrier gas (Ar) flow rate (l min$^{-1}$) | 0.4 |
| Carrier gas (He) flow rate (l min$^{-1}$) | 0.8 |
| Samples per peak | 120 |
| Time per pass (s) | 0.7 |
| Mass window (%) | 10 |

### 3.2.4 Chronology

Chronologies for both sediment cores have been described in detail by Mügler et al. (2010) and Doberschütz et al. (2013). It is assumed that the age of an individual ostracod shell corresponds to the age of the sediment layer from which the shell was picked.

## 3.3 Results

### 3.3.1 Concentrations of trace elements in the shells

Concentrations of 17-18 trace elements in the shells from both cores were determined in our study (Tables 3.2 and 3.3). The repeatability, expressed as relative standard deviation (RSD) in percent, of trace element analyses for line-

Table 3.2: Trace element compositions (µg $g^{-1}$) in single ostracod shells of the three taxa from NC 08/01 by line-scan and spot analyses.

| Core depth (cm) | Age (cal BP) | Mg | Sr | Ba | U | La | Ce | Pr | Nd | Sm | Eu | Gd | Tb | Dy | Ho | Er | Tm | Yb | Lu | LREE/HREE[a] |
|---|---|---|---|---|---|---|---|---|---|---|---|---|---|---|---|---|---|---|---|---|
| *L. sinensis* (Line[b]) | | | | | | | | | | | | | | | | | | | | |
| 15 | 223 | 8060 | 13100 | 569 | 10.6 | 8.60 | 16.6 | 2.29 | 6.24 | 1.69 | 0.21 | 1.47 | 0.30 | 1.64 | 0.35 | 0.84 | 0.11 | 0.66 | 0.074 | 6.5 |
| 25 | 402 | 8470 | 11300 | 479 | 0.24 | 0.54 | 1.01 | 0.10 | 0.55 | 0.23 | 0.090 | 0.059 | 0.014 | 0.17 | 0.051 | 0.074 | 0.010 | 0.14 | 0.014 | 4.8 |
| 30 | 485 | 16800 | 10400 | 640 | 3.02 | 8.21 | 15.5 | 1.35 | 5.41 | 1.15 | 0.32 | 1.35 | 0.22 | 1.11 | 0.20 | 0.59 | 0.10 | 0.57 | 0.068 | 7.6 |
| 35 | 528 | 9680 | 9660 | 513 | 6.12 | 6.95 | 11.9 | 1.58 | 4.98 | 1.45 | 0.33 | 1.59 | 0.23 | 1.44 | 0.27 | 0.72 | 0.13 | 0.65 | 0.10 | 5.3 |
| 40 | 675 | 23500 | 9510 | 505 | 17.3 | 5.37 | 10.8 | 1.14 | 3.94 | 0.75 | 0.22 | 1.13 | 0.20 | 0.98 | 0.20 | 0.63 | 0.11 | 0.35 | 0.072 | 6.0 |
| 45 | 937 | 5220 | 7220 | 385 | 14.7 | 7.30 | 15.2 | 1.21 | 5.67 | 1.71 | 0.44 | 1.39 | 0.28 | 1.72 | 0.34 | 1.00 | 0.19 | 0.68 | 0.20 | 5.4 |
| 55 | 1140 | 15000 | 9260 | 509 | 3.38 | 2.38 | 3.89 | 0.64 | 2.40 | 0.65 | 0.15 | 0.49 | 0.069 | 0.42 | 0.10 | 0.34 | 0.047 | 0.26 | 0.051 | 5.7 |
| 60 | 1276 | 11300 | 4870 | 342 | 3.32 | 3.84 | 4.42 | 1.28 | 2.07 | 1.27 | 0.20 | 0.73 | 0.17 | 0.76 | 0.17 | 0.36 | 0.10 | 0.47 | 0.089 | 4.6 |
| 63.5 | 1339 | 4040 | 5690 | 227 | 0.77 | 1.77 | 2.37 | 0.44 | 1.06 | 0.21 | 0.12 | 0.25 | 0.030 | 0.18 | 0.054 | 0.15 | 0.020 | 0.20 | 0.037 | 6.6 |
| 123.5 | 2915 | 1420 | 1990 | 108 | 2.07 | 3.81 | 7.67 | 0.93 | 3.13 | 0.86 | 0.20 | 0.89 | 0.17 | 0.84 | 0.14 | 0.47 | 0.059 | 0.30 | 0.064 | 5.7 |
| 157 | 4755 | 1100 | 970 | 76.2 | 1.71 | 8.10 | 17.3 | 1.95 | 8.94 | 2.11 | 0.42 | 2.33 | 0.40 | 2.25 | 0.42 | 1.06 | 0.18 | 0.99 | 0.12 | 5.0 |
| 161 | 5053 | 2360 | 1420 | 104 | 3.41 | 4.14 | 9.11 | 0.98 | 3.92 | 0.97 | 0.21 | 1.04 | 0.18 | 0.98 | 0.20 | 0.46 | 0.082 | 0.47 | 0.077 | 5.5 |
| 165.6 | 5391 | 3550 | 1390 | 193 | 3.34 | 4.01 | 7.76 | 1.13 | 3.75 | 1.07 | 0.13 | 1.17 | 0.13 | 1.02 | 0.13 | 0.59 | 0.031 | 0.35 | 0.073 | 5.1 |
| 166 | 5423 | 980 | 1390 | 104 | 1.92 | 3.86 | 7.79 | 0.89 | 3.73 | 1.06 | 0.15 | 0.98 | 0.17 | 0.82 | 0.20 | 0.52 | 0.066 | 0.40 | 0.063 | 5.5 |
| 176 | 5964 | 1600 | 1640 | 129 | 1.10 | 5.67 | 12.8 | 1.45 | 5.42 | 1.36 | 0.27 | 1.38 | 0.20 | 1.26 | 0.22 | 0.59 | 0.059 | 0.55 | 0.079 | 6.2 |
| 186 | 6636 | 2240 | 1390 | 115 | 1.27 | 6.28 | 15.7 | 1.75 | 6.65 | 1.72 | 0.35 | 1.69 | 0.27 | 1.69 | 0.32 | 0.89 | 0.14 | 0.79 | 0.12 | 5.5 |
| 187 | 6734 | 1370 | 1170 | 104 | 1.37 | 4.65 | 12.2 | 1.17 | 5.12 | 1.28 | 0.29 | 1.22 | 0.20 | 1.28 | 0.24 | 0.60 | 0.10 | 0.73 | 0.10 | 5.5 |
| 215 | 9058 | 1150 | 1730 | 214 | 2.05 | 3.18 | 6.11 | 0.75 | 2.36 | 0.73 | 0.17 | 0.91 | 0.089 | 0.61 | 0.13 | 0.40 | 0.052 | 0.33 | 0.059 | 5.2 |
| 221 | 9766 | 2030 | 1600 | 172 | 1.39 | 3.20 | 4.48 | 0.57 | 2.17 | 0.59 | 0.12 | 0.49 | 0.078 | 0.55 | 0.12 | 0.33 | 0.059 | 0.43 | 0.046 | 5.3 |
| 227 | 10480 | 5130 | 1400 | 145 | 2.55 | 8.70 | 18.3 | 2.24 | 9.07 | 2.16 | 0.54 | 2.57 | 0.39 | 2.29 | 0.46 | 1.12 | 0.18 | 1.15 | 0.17 | 4.9 |
| 231 | 10933 | 4470 | 12000 | 481 | 2.01 | 2.21 | 4.29 | 0.59 | 1.75 | 0.43 | 0.089 | 0.44 | 0.10 | 0.39 | 0.11 | 0.21 | 0.020 | 0.13 | 0.041 | 6.5 |
| 236 | 11266 | 4620 | 14300 | 506 | 1.09 | 1.44 | 2.57 | 0.22 | 1.02 | 0.22 | 0.045 | 0.27 | 0.032 | 0.29 | 0.052 | 0.11 | 0.024 | 0.10 | 0.007 | 6.3 |
| 240 | 11372 | 5100 | 15800 | 584 | 1.45 | 2.11 | 4.05 | 0.41 | 1.90 | 0.28 | 0.075 | 0.44 | 0.069 | 0.36 | 0.087 | 0.19 | 0.036 | 0.19 | 0.034 | 6.3 |
| f. *typica* (Line[b]) | | | | | | | | | | | | | | | | | | | | |
| 123.5 | 2915 | 2370 | 3320 | 228 | 2.16 | 4.25 | 8.86 | 1.29 | 4.63 | 1.11 | 0.38 | 0.80 | 0.10 | 0.83 | 0.10 | 0.51 | 0.054 | 0.37 | 0.045 | 7.3 |
| 187 | 6734 | 1850 | 1950 | 150 | 1.48 | 4.79 | 10.0 | 1.25 | 4.76 | 1.27 | 0.33 | 1.19 | 0.20 | 1.10 | 0.21 | 0.50 | 0.079 | 0.49 | 0.056 | 5.9 |
| f. *postilirata* (Line[b]) | | | | | | | | | | | | | | | | | | | | |
| 93.5 | 1933 | 16600 | 5810 | 625 | 4.42 | 2.34 | 3.27 | 0.41 | 1.59 | 0.33 | 0.11 | 0.42 | 0.078 | 0.20 | 0.085 | 0.20 | 0.054 | 0.15 | 0.034 | 6.6 |
| 221 | 9766 | 4880 | 1390 | 225 | 2.63 | 3.95 | 6.82 | 0.98 | 4.02 | 1.10 | 0.28 | 1.16 | 0.19 | 1.18 | 0.23 | 0.55 | 0.085 | 0.51 | 0.10 | 4.3 |
| 225.6 | 10314 | 4060 | 6210 | 496 | 1.27 | 3.53 | 6.46 | 0.82 | 3.39 | 0.98 | 0.15 | 0.93 | 0.13 | 1.11 | 0.16 | 0.57 | 0.039 | 0.31 | 0.069 | 4.6 |
| 227 | 10480 | 33300 | 1310 | 421 | 15.5 | 4.75 | 9.05 | 1.10 | 6.61 | 1.16 | 0.96 | 2.35 | 0.51 | 3.47 | 0.73 | 2.74 | 0.43 | 2.56 | 0.34 | 1.8 |
| 231 | 10933 | 9440 | 12000 | 911 | 2.08 | 5.00 | 9.00 | 1.32 | 3.70 | 0.74 | 0.20 | 1.12 | 0.17 | 0.95 | 0.18 | 0.46 | 0.051 | 0.41 | 0.068 | 5.9 |
| 236 | 11266 | 23200 | 930 | 340 | 5.20 | 5.94 | 11.0 | 1.55 | 6.34 | 1.76 | 0.61 | 2.99 | 0.49 | 3.33 | 0.90 | 2.15 | 0.35 | 2.12 | 0.35 | 2.1 |
| *L. sinensis* (Spot[c]) | | | | | | | | | | | | | | | | | | | | |
| 63.5 | 1339 | 7230 | 4980 | 285 | 1.07 | 1.53 | 2.63 | 0.59 | 1.19 | 0.48 | 0.21 | 0.66 | 0.076 | 0.44 | 0.089 | 0.28 | 0.025 | 0.24 | 0.042 | 3.6 |
| 123.5 | 2915 | 1970 | 1580 | 172 | 1.60 | 3.83 | 7.72 | 1.00 | 3.40 | 0.93 | 0.16 | 0.53 | 0.14 | 0.65 | 0.13 | 0.50 | 0.052 | 0.32 | 0.056 | 7.2 |
| 157 | 4755 | 1000 | 970 | 130 | 1.76 | 9.31 | 20.2 | 2.22 | 8.34 | 2.12 | 0.42 | 2.21 | 0.32 | 1.92 | 0.36 | 0.82 | 0.12 | 0.77 | 0.11 | 6.4 |

Table 3.2: Trace element compositions (µg $g^{-1}$) in single ostracod shells of the three taxa from NC 08/01 by line-scan and spot analyses.

| Core depth (cm) | Age (cal BP) | Mg | Sr | Ba | U | La | Ce | Pr | Nd | Sm | Eu | Gd | Tb | Dy | Ho | Er | Tm | Yb | Lu | LREE/HREE[a] |
|---|---|---|---|---|---|---|---|---|---|---|---|---|---|---|---|---|---|---|---|---|
| *L. sinensis* (Spot[c]) | | | | | | | | | | | | | | | | | | | | |
| 161 | 5053 | 5300 | 1720 | 229 | 2.54 | 4.10 | 8.62 | 0.98 | 3.31 | 0.68 | 0.26 | 0.97 | 0.17 | 0.64 | 0.15 | 0.42 | 0.11 | 0.48 | 0.11 | 5.9 |
| 165.6 | 5391 | 3200 | 1670 | 132 | 3.16 | 3.81 | 8.42 | 1.03 | 3.67 | 0.74 | 0.17 | 1.01 | 0.19 | 0.72 | 0.16 | 0.46 | 0.060 | 0.39 | 0.042 | 5.9 |
| 166 | 5423 | 2980 | 1560 | 213 | 3.66 | 5.13 | 13.2 | 2.17 | 3.73 | 0.98 | 0.45 | 0.82 | 0.15 | 0.83 | 0.14 | 0.57 | 0.071 | 0.30 | 0.059 | 8.8 |
| 176 | 5964 | 3260 | 1200 | 180 | 1.89 | 5.36 | 12.7 | 1.42 | 5.08 | 1.00 | 0.40 | 1.01 | 0.20 | 1.03 | 0.20 | 0.70 | 0.061 | 0.60 | 0.11 | 6.6 |
| 187 | 6734 | 2020 | 1520 | 142 | 2.16 | 5.47 | 11.9 | 1.31 | 4.87 | 1.40 | 0.21 | 0.97 | 0.17 | 1.32 | 0.23 | 0.59 | 0.065 | 0.36 | 0.063 | 6.7 |
| 215 | 9058 | 1390 | 1560 | 126 | 4.06 | 2.15 | 5.63 | 0.53 | 1.86 | 0.50 | 0.38 | 0.52 | 0.10 | 0.52 | 0.13 | 0.31 | 0.028 | 0.24 | 0.042 | 5.9 |
| 221 | 9766 | 2110 | 1760 | 194 | 1.22 | 3.58 | 4.40 | 0.36 | 1.36 | 0.47 | 0.077 | 0.47 | 0.043 | 0.30 | 0.066 | 0.15 | 0.028 | 0.20 | 0.021 | 8.1 |
| f. *typica* (Spot[c]) | | | | | | | | | | | | | | | | | | | | |
| 123.5 | 2915 | 3350 | 2470 | 189 | 1.55 | 2.75 | 5.53 | 0.67 | 1.73 | 0.45 | 0.10 | 0.31 | 0.069 | 0.27 | 0.060 | 0.23 | 0.026 | 0.19 | 0.045 | 9.3 |
| 187 | 6734 | 3350 | 1810 | 220 | 1.71 | 4.11 | 13.3 | 1.19 | 4.09 | 1.10 | 0.23 | 0.80 | 0.15 | 0.82 | 0.15 | 0.38 | 0.059 | 0.43 | 0.058 | 8.5 |
| f. *postilirata* (Spot[c]) | | | | | | | | | | | | | | | | | | | | |
| 221 | 9766 | 6100 | 2110 | 215 | 1.11 | 3.80 | 3.50 | 0.55 | 1.51 | 2.85 | 0.30 | 0.30 | 0.17 | 0.37 | 0.10 | 0.68 | 0.080 | - | 0.15 | - |
| 225.6 | 10314 | 8800 | 17600 | 1112 | 1.58 | 4.27 | 3.69 | 0.36 | 4.54 | 0.85 | 0.14 | 0.83 | 0.10 | 1.26 | 0.12 | 0.52 | 0.075 | 0.48 | 0.072 | 4.0 |

[a] LREE/HREE: the total concentration of La, Ce, Pr, Nd, Sm and Eu divided by that of Gd, Tb, Dy, Ho, Er, Tm, Yb and Lu in a single shell. [b] Line: line-scan analysis.

[c] Spot: spot analysis.

Table 3.3: Average trace element concentrations (µg $g^{-1}$) in the *L. sinensis* shells from different depths of Nam Co 8 by spot analysis.

| Core depth (cm) | Age (cal BP) | Sr | Ba | U | La | Ce | Pr | Nd | Sm | Eu | Gd | Tb | Dy | Ho | Er | Tm | Yb | Lu | LREE/HREE[a] |
|---|---|---|---|---|---|---|---|---|---|---|---|---|---|---|---|---|---|---|---|
| 31 | 250 | 4830 | 1400 | 16.6 | 6.63 | 15.6 | 1.66 | 6.97 | 0.93 | 0.31 | 0.63 | 0.13 | 1.17 | - | - | 0.14 | 0.97 | 0.13 | - |
| 46 | 450 | 5140 | 413 | 11.5 | 3.16 | 5.64 | 0.64 | 3.12 | 0.64 | 0.15 | 0.68 | 0.12 | 0.64 | 0.14 | 0.50 | 0.077 | 0.46 | 0.078 | 5.0 |
| 151 | 2550 | 2100 | 245 | 12.5 | 4.49 | 7.56 | 0.58 | 3.32 | 0.61 | 0.16 | 0.59 | 0.089 | - | 0.14 | 0.45 | - | 0.33 | - | - |
| 211 | 4650 | 1540 | 278 | 8.17 | 7.36 | 16.6 | 1.66 | 7.22 | 1.80 | 0.30 | 1.66 | 0.24 | 1.38 | 0.22 | 0.67 | 0.12 | 0.63 | 0.092 | 6.9 |
| 216 | 4700 | 1490 | 274 | 11.9 | 8.09 | 16.6 | 1.66 | 7.90 | 1.76 | 0.34 | 2.54 | 0.25 | 1.76 | 0.27 | 0.82 | 0.083 | 0.72 | 0.085 | 5.6 |
| 236 | 5950 | 1370 | 266 | 24.3 | 9.72 | 22.4 | 3.02 | 11.4 | 2.34 | 0.59 | 2.54 | 0.34 | 2.15 | 0.51 | 1.07 | 0.17 | 1.17 | 0.18 | 6.1 |
| 256 | 6550 | 1400 | 319 | 10.8 | 6.29 | 13.9 | 1.51 | 5.70 | 1.16 | 0.22 | 1.04 | 0.17 | 0.91 | 0.19 | 0.56 | - | 0.38 | 0.051 | - |
| 261 | 6750 | 1610 | 174 | 12.0 | 4.88 | 9.41 | 1.07 | 4.73 | 1.17 | 0.27 | 2.05 | 0.23 | 1.27 | 0.28 | 0.68 | 0.11 | 0.48 | 0.068 | 4.2 |

The concentrations in this table were obtained by the average values of two or three *L. sinensis* shells from each depth. The concentrations of some rare earth elements were not detected by the spot analyses (-). [a] LREE/HREE: the total concentration of La, Ce, Pr, Nd, Sm and Eu divided by that of Gd, Tb, Dy, Ho, Er, Tm, Yb and Lu in a single shell.

scan measurements is shown in Figure 3.3. Here the elements with lower concentrations (i.e., lower detected count rates) usually have higher RSD values. For most elements with abundances > 1 µg $g^{-1}$, the RSD values for the line-scan method range from 15-30%, which is better than the 20-40% for the spot analyses (not shown) with a lower sample test portion mass per spot than the test portion mass per line. Additionally, ?*L. dorsotuberosa* f. *postilirata,* as a deep-water taxon with extremely thin and fragile shells (Wrozyna et al., 2009a), exhibits generally higher RSD than *L. sinensis* and ?*L. dorsotuberosa* f. *typica* (Figure 3.3), associated with a lower ablated sample mass (< 0.1 µg) per line scan compared to that (ca. 0.15 µg) of the latter two.

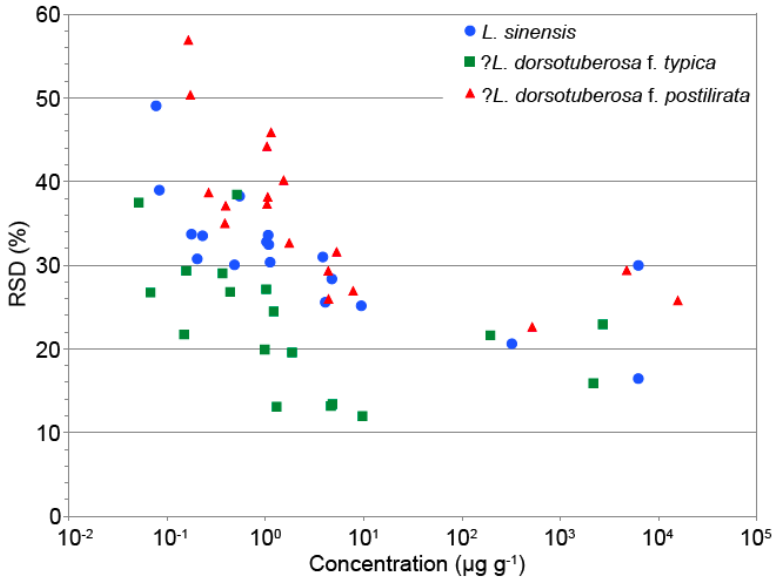


Figure 3.3: Relationship between the concentrations and RSD (relative standard deviation) values of trace elements measured in single ostracod shells, obtained by line-scan LA-ICP-MS measurements.

As shown in Tables 3.2 and 3.3, Mg and Sr are the most abundant trace metals in the specimens, showing significant variations between individual shells, even within the same taxon (e.g., Mg ranged from about 1000 to 24,000 µg $g^{-1}$ for *L. sinensis* and 4000 to 34,000 µg $g^{-1}$ for ?*L. dorsotuberosa* f. *postilirata*, while Sr from about 1000 to 16,000 µg $g^{-1}$ for *L. sinensis* and 1000 to 18,000 µg $g^{-1}$ for ?*L. dorsotuberosa* f. *postilirata*). Barium has a lower abundance than Mg and Sr, varying from about 80 to 1400 µg $g^{-1}$ for the three taxa. Uranium and the REEs have concentrations lower than 25 µg $g^{-1}$, while the lowest concentrations are observed for Eu, Tb, Ho, Er, Tm, Yb and Lu, with concentrations generally less than 1 µg $g^{-1}$.

In order to investigate the potential differences in the shell composition among the three taxa, the average concentrations and concentration ranges of Mg, Sr, Ba and Ce for the shells from both cores are shown in Figure 3.4. Due to the limited distribution of ?*L. dorsotuberosa* f. *typica* and ?*L. dorsotuberosa* f. *postilirata* and to avoid the influence of variable past hydrochemical conditions in the lake during different periods, only shells from the periods ~10.0 to ~9.1 and ~6.7 to ~6.0 cal ka BP were used in this figure. With regard to the concentration ranges, the elemental contents agree well between *L. sinensis* from both cores. Similar concentrations are observed among the three taxa from NC 08/01, with the exception of slightly higher Mg for ?*L. dorsotuberosa* f. *postilirata* (Figure 3.4), which could be due to its limited sample size. Similar abundances are also detected for other trace elements among the three taxa from NC 08/01 (Table 3.2). Because of the limited sample amount, no final conclusion can be drawn here. However, it appears that no significant species-related differences in trace element composition are observed in our study.

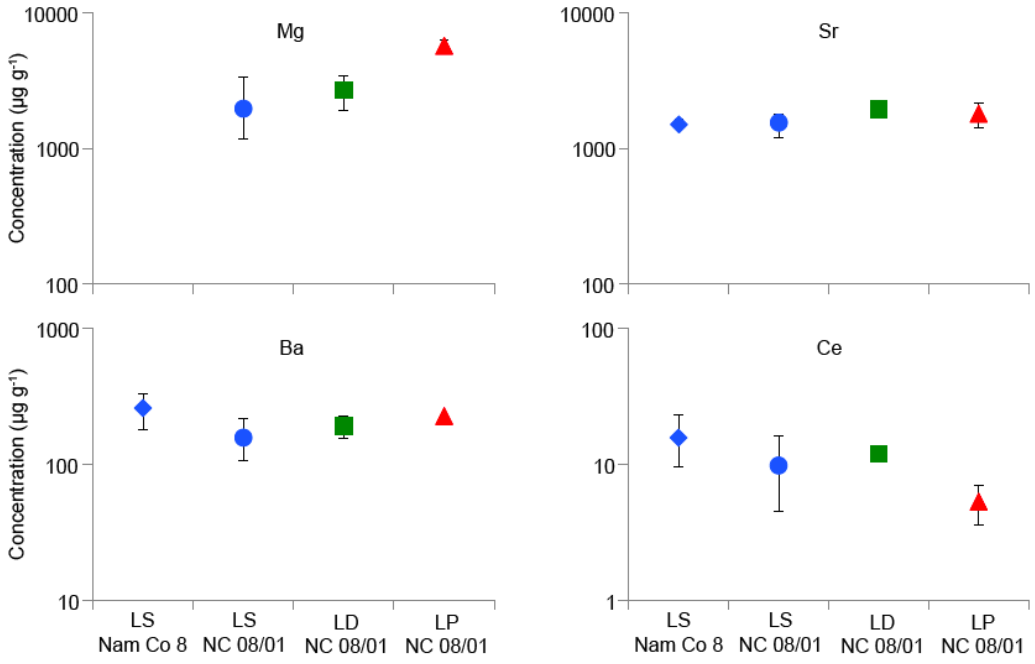


Figure 3.4: Average concentrations (shown by symbols) and concentration ranges (shown by error bars) of different trace elements in the shells from ~10.0 to ~9.1 and ~6.7 to ~6.0 cal ka BP from the cores Nam Co 8 and NC 08/01. LS, LD and LP at the X axis refer to the three species *L. sinensis* (n = 3 for Nam Co 8, n = 9 for NC 08/01), ?*L. dorsotuberosa* f. *typica* (n = 2) and ?*L. dorsotuberosa* f. *postilirata* (n = 2), respectively. Mg was not determined in the shells from Nam Co 8.

As expected, the REEs show a significant positive correlation with each other, with correlation coefficients generally higher than 0.7. Additionally, a significant light-REE (LREE, i.e., La, Ce, Pr, Nd, Sm and Eu) enrichment is observed for all three taxa, with the LREE/HREE (defined as the total concentration of LREEs divided by that of heavy-REEs, i.e., Gd, Tb, Dy, Ho, Er, Tm, Yb and Lu, in a single shell) ratios ranging from 3.6 to 8.8 for *L. sinensis*, 5.9 to 9.4 for ?*L. dorsotuberosa* f. *typica* and 1.8 to 6.8 for ?*L. dorsotuberosa* f. *postilirata*.

### 3.3.2 Trace element ratios

Figure 3.5 shows the molar ratios of Mg/Ca, Sr/Ca, Ba/Ca, U/Ca and La/Ca in the shells from both cores. Due to the high correlation between the REEs, only La/Ca, as the representative of the fluctuations of REE ratios, is shown in this figure. For the shells of the same taxa from the same depth in NC 08/01, the ratios obtained by both analytical methods agree well with each other (Figure 3.5). Sr/Ca, Ba/Ca and La/Ca show comparable values between *L. sinensis* from both cores during the same periods, while higher U/Ca is observed for the shells from Nam Co 8 during ~6.8 to ~2.6 cal ka BP compared to those from NC 08/01. ?*L. dorsotuberosa* f. *typica* exhibits consistent ratios with *L. sinensis* although the former were only collected from two depths (187 and 123.5 cm) in NC 08/01. ?*L. dorsotuberosa* f. *postilirata* was mainly found from 236 to 221 cm (~11.3 to ~9.8 cal ka BP) in NC 08/01, showing variable ratios with higher uncertainties during this interval (Figure 3.5).

In general, Mg/Ca, Sr/Ca and Ba/Ca exhibit similar fluctuations, with higher values from ~11.4 to ~10.3, relatively low and stable values from ~9.8 to ~3.0 and higher values from ~1.3 to ~0.2 cal ka BP. Differing from the higher U/Ca from Nam Co 8 after ~6.8 cal ka BP, U/Ca from NC 08/01 shows low and constant values from ~11.4 to ~3.0 and a distinct rise during ~1.3 to ~0.2 cal ka BP with intensified excursions. No clear tendency is observed for La/Ca, which shows relatively constant values considering the uncertainty ranges.

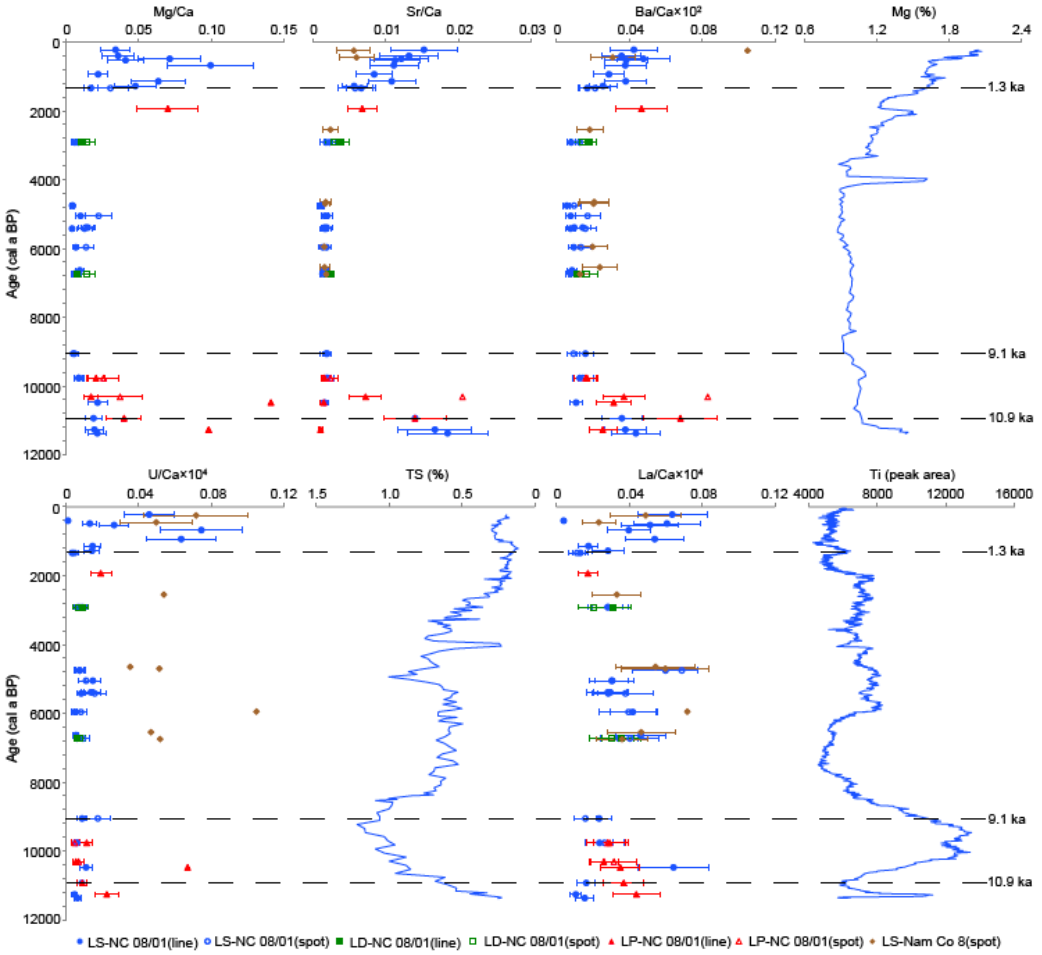


Figure 3.5: Molar ratios of trace elements to calcium in the shells of *L. sinensis* (LS), ?*L. dorsotuberosa* f. *typica* (LD) and ?*L. dorsotuberosa* f. *postilirata* (LP) from the cores Nam Co 8 and NC 08/01 plotted on an age scale, accompanied by the fluctuations of Mg, total sulphur (TS), and Ti in the sediments of NC 08/01 (Doberschütz et al., 2013). The unit "peak area" represents the X-ray fluorescence data. An uncertainty of 30% is assumed for the ratios obtained by line-scan measurements and 40% for those by spot analysis. Note that TS is on an inverse scale. Each ratio for NC 08/01 refers to the value in a single shell, while each ratio for Nam Co 8 refers to the average value in two or three shells at each depth.

## 3.4 Discussion

### 3.4.1 Mg/Ca and Sr/Ca ratios

The trace element chemistry (mainly Mg and Sr) in non-marine ostracod shells has been widely used for paleosalinity reconstructions (Griffiths and Holmes,

2000; Börner et al., 2013). Evaporative concentration in hydrologically closed basins often induces precipitation of calcium carbonates, resulting in an elevation of Mg/Ca and Sr/Ca molar ratios and therefore a positive correlation between the element ratios and salinity in the host water (Holmes et al., 1999). Since the Mg/Ca and Sr/Ca ratios in ostracod shells have been demonstrated to be a function of the same ratios in the host water, a possible positive relationship between the ratios in the shells and salinity can be expected under certain circumstances (Chivas et al., 1983, 1985, 1986; Engstrom and Nelson, 1991; Holmes, 1996; Xia et al., 1997 a, b; Wansard et al., 1998; De Deckker et al., 1999). Mg/Ca in ostracod calcite may also depend on the water temperature, although this dependence may be easily eclipsed by small Mg/Ca changes in the ambient water (De Deckker et al., 1999). Ostracod Sr/Ca is relatively independent of temperature for the ranges in which ostracods normally live (Chivas et al., 1983, 1985, 1986; Engstrom and Nelson, 1991).

A recent study concerning the hydrological characteristics of the Nam Co basin (Keil et al., 2010) reported the dominating influence of evaporative concentration on hydrochemical conditions in the lake system, which is evidenced by significant increases of stable isotope ratios ($\delta D$ and $\delta^{18}O$), solute (such as $Na^{+}$, $Mg^{2+}$ and $Sr^{2+}$) concentrations, and lake water salinity in comparison to the inflow streams and precipitation (with maximum conductivities of 1920, 431 and 5.5 $\mu S\ mm^{-1}$, respectively, Li et al., 2007; Keil et al., 2010). The climate-driven salinity variations during the Holocene period, mainly due to the precipitation/evaporation (P/E) balance, were also inferred from the sediment records from this lake (Mügler et al., 2010; Doberschütz et al., 2013; Kasper et al., 2013). In spite of a huge increase of melt water input during the last several decades (Zhu et al., 2010b), the lake water is saturated with respect to calcite at present (Keil et al., 2010). High abundances of endogenic carbonate precipitation were observed across the whole profiles of Nam Co 8 [covering the last ~7.2 ka by Mügler et al. (2010)] and NMLC1 [covering the last ~8.4 ka by Li et al. (2008b)] (Figure 3.1). This may indicate that Ca levels in the water have remained relatively constant or varied only to a small degree during large parts of the Holocene as a consequence of $CaCO_3$ precipitation. A possible exception is the interval from ~11 to ~8 cal ka BP, when little or no $CaCO_3$ precipitation was observed in NC 08/01 (covering the last ~11.3 ka), corresponding to the inferred Holocene optimum of precipitation in this region (Doberschütz et al., 2013). There is a positive relationship between Mg/Ca as well as Sr/Ca and salinity in the water samples collected from the lake water and inflow streams (Li et al., 2008b; Keil et al., 2010). Although substantial amounts ($\leq$ 25%) of clay minerals have been detected in the sediments (Li et al., 2008b; Mügler et al., 2010), which tend to uptake Mg from the host water and hence

interfere with the correlation between Mg/Ca and salinity (Holmes et al., 1997, 1999), the uptake effect is likely to be minor in Lake Nam Co. This is because clay minerals are mainly transported by the inflow streams, and the measured Mg contents in the stream waters (Keil et al., 2010) may indicate that partial or even complete Mg uptake occurs before the clay minerals reach the lake environment. Aragonite precipitation is another potential affecting factor, which can remove Sr from the host water and result in depleted Sr/Ca in water in spite of high salinity (Griffiths and Holmes, 2000). However, aragonite was not observed in NC 08/01 or NMLC1 (Li et al., 2008b; Doberschütz et al., 2013), and only detected with low concentrations from ~2.1 to ~1.4 cal ka BP in Nam Co 8 (Mügler et al., 2010), suggesting a limited effect of aragonite precipitation on water Sr/Ca. Additionally, grain size distributions are fairly uniform in the sediment records, dominated by silt deposits with less clayey and sandy materials (Mügler et al., 2010; Doberschütz et al., 2013). Allogenic detrital materials, primarily produced by bedrock weathering, glacial erosion and periglacial processes in the catchment, show relatively constant compositions (mainly including quartz, clay minerals, mica and feldspars) in the sediment profiles (Mügler et al., 2010; Doberschütz et al., 2013). This may imply that the sediment sources didn't change significantly through time and hence may have only a secondary influence on solute evolution in the lake relative to the balance between precipitation (or melt water) and evaporation.

One of the main potential pitfalls of the analysis of fossil ostracods from sediment cores is the occurrence of allochthonous shells transported to the core position. Kasper et al. (2013) reported the relative lake level of Nam Co during the last ~4.0 ka established by an ostracod-based water depth transfer function, which showed good agreement with the sedimentological, geochemical and microfossil records in NC 08/01. This could indicate a weak influence of allochthonous transport on local ostracod assemblages, perhaps due to the calm conditions at the deep water depth of NC 08/01 and its large distance to the shore. Nam Co 8 is more likely to obtain allochthonous shells during sedimentation, owing to its shallower water depth and location closer to the shore. Thus, occasional mixing with shells from other locations in the lake may not be completely excluded for our specimens. On the other hand, the ostracod shells measured in our study are generally well preserved and hyaline, without evidence of abrasion, corrosion or visible coating, perhaps indicating a minor influence of early diagenesis on these samples.

The water depth (93 m) of NC 08/01 is well below the present-day thermocline [20-30 m, Keil et al. (2010)]. Therefore, seasonal temperature

variability should have insignificant effects on the Mg/Ca signal in ostracod shells from this core. The seasonal effects could be stronger for the shells from Nam Co 8 due to its water depth (31 m) close to the thermocline, but Sr/Ca would still be less affected because of its insensibility to temperature changes.

Based on the fluctuations of Mg/Ca and Sr/Ca in the shells and the Mg record from NC 08/01 (Figure 3.5), possible hydrochemical changes in Lake Nam Co during the Holocene are discussed in the following paragraphs. Mg mainly exists as authigenic carbonate in the sediments and therefore reflects chemical enrichment in the lake water influenced by the P/E balance (Doberschütz et al., 2013).

From ~11.4 to ~10.9 cal ka BP, both Mg/Ca and Sr/Ca in *L. sinensis* and ?*L. dorsotuberosa* f. *postilirata* show relatively high values, in accordance with the higher abundance of Mg in the sediments, possibly suggesting higher Mg/Ca, Sr/Ca, and salinity in the lake water during this interval. This period corresponds to dry climatic conditions at Nam Co between ~11.6 and ~10.8 cal ka BP as inferred from the sediment records (Doberschütz et al., 2013), indicating that the negative P/E balance (inducing a strong evaporative concentration process) may be the main force driving the solute enrichment in the lake system. On the other hand, less clay mineral input due to decreased inflow streams (i.e., less precipitation and melt water) would have incorporated less Mg and hence accounted for higher Mg/Ca in the host water to some extent.

A general decreasing trend of Mg/Ca and Sr/Ca, associated with the low Mg content in the sediments, was observed in the following period from ~10.9 to ~9.1 cal ka BP, perhaps implying lower element ratios and salinity in the lake water. As a significant lake level rise of Nam Co was reported from ~10.8 to ~9.5 cal ka BP related to a strong summer monsoon on the central Tibetan Plateau (Doberschütz et al., 2013), this decrease was most likely caused by the dilution process due to enhanced freshwater (precipitation and/or melt water) influx. The increased inflows would have caused calcite undersaturation in the lake water, as reflected by little or no $CaCO_3$ precipitation in NC 08/01 (Doberschütz et al., 2013), allowing a lesser decrease of Ca relative to Mg and Sr in the host water. Alternatively, more clay mineral input by increased fluvial transport during this phase may have removed more Mg from the water and partially driven a greater drop of Mg in comparison to Ca.

Since no sample was measured from the period between ~9.1 and ~6.7 cal ka BP, the interpretation of past hydrochemical changes is impossible for this period. In the subsequent interval from ~6.7 to ~4.8 cal ka BP, the Mg and Sr ratios in the shells, as well as the Mg content in the sediments, present relatively low and constant values, potentially implying a stable lake environment with low Mg/Ca and Sr/Ca in the water. A contemporary higher lake level related to an enhancement of moisture availability was inferred during ~6.6 to ~4.8 cal ka BP (Doberschütz et al., 2013), possibly causing dilution of solute concentrations in the lake water and/or more clay uptake of Mg. Because of the limited number of samples from ~4.8 to ~1.3 cal ka BP, no detailed information on the hydrochemical variations can be derived for this period. A drying tendency was reported from 4.0 to 1.4 cal ka BP by Mügler et al. (2010), and from ~4.8 to ~2.0 cal ka BP by Doberschütz et al. (2013). However, the low ratios for *L. sinensis* and ?*L. dorsotuberosa* f. *typica* around 3.0 cal ka BP may indicate lower Mg/Ca and Sr/Ca in the water. The higher Mg/Ca and Sr/Ca in the shell of ?*L. dorsotuberosa* f. *postilirata* at ~1.9 cal ka BP is in good agreement with the Mg peak in the sediments (Figure 3.5).

With relatively large uncertainties, both Mg and Sr ratios show higher values from ~1.3 to ~0.2 cal ka BP, coupled with an enrichment of Mg in the sediments (Figure 3.5), which may reflect increased elemental ratios and salinity in the lake. This process could be due to the dry conditions at Nam Co since ~1.3 cal ka BP as reported by Doberschütz et al. (2013). Mg/Ca exhibits lower values around 0.2 cal ka BP (Figure 3.5), which may, however, not reflect low Mg concentrations (or Mg/Ca) in the host water, because the maximum Mg content in the sediment occurred at the same time. A possible reason for this discrepancy could be the lower temperature suppressing ostracod Mg uptake (De Deckker et al., 1999), perhaps due to the Little Ice Age (LIA). The LIA at Nam Co has been identified by several previous studies [from ~0.6 to ~0.3 by Zhu et al. (2008), ~0.46 to ~0.19 by Frenzel et al. (2010), ~0.55 to ~0.25 cal ka BP by Günther et al. (2011)]. Kasper et al. (2012) reported the most pronounced cold and dry event of the LIA – the Maunder Minimum from ~280 cal BP to ~260 cal BP - in this area. Additionally, an advance of the Zepu glacier in the Nyainqentanglha Mountains (Figure 3.1) during the LIA was also reported at 190 ± 80 cal BP (Jiao et al., 2005), confirming the lower temperature around 0.2 cal ka BP at Nam Co. Alternatively, the lower Mg/Ca at ~0.2 cal ka BP could be explained by a reduced uptake of Mg into ostracod calcite in high-Mg water (as reflected by high Mg content in the sediments) since a decline of the Mg distribution coefficient for ostracod calcite in high Mg/Ca solutions was observed in previous studies (Xia et al., 1997a). The hydrochemical changes during the last 0.2 ka cannot be reflected in our ostracod record because no sample was available from this period.

### 3.4.2 Ba/Ca ratios

A preliminary study by Chivas et al. (1983) reported Ba contents in the soft parts, chitin and shells of the cypridid ostracod *Mytilocypris henricae* and that Ba-uptake into the shells is possibly correlated to water temperature but less affected by Ba/Ca in solution. However, ostracod Ba/Ca has been limitedly investigated since that and the observation by Chivas et al. (1983) is not clarified. More recent studies demonstrated that Ba/Ca in inorganic calcite (Tesoriero and Pankow, 1996) and the calcite shells of certain foraminifera (Lea and Boyle, 1989; Lea and Spero, 1994; Havach et al., 2001) and mussel (Gillikin et al., 2006) species is a function of Ba/Ca in the host water and independent on water temperature.

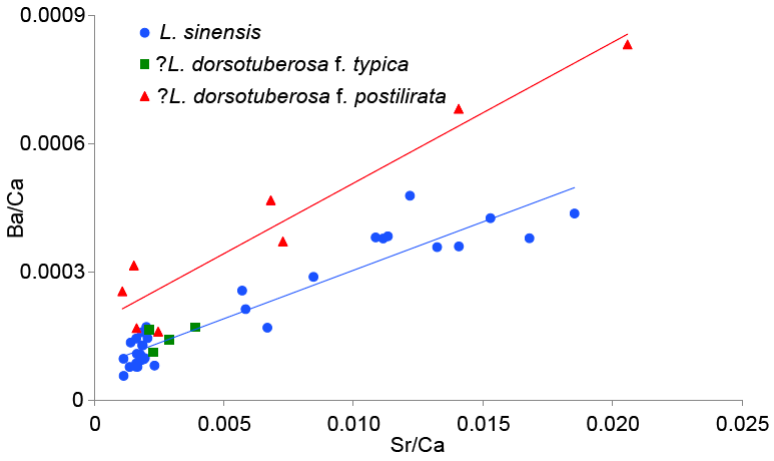


Figure 3.6: Molar ratios of Ba/Ca against Sr/Ca for the shells of the three ostracod taxa from NC 08/01. Due to the limited number of shells of ?*L. dorsotuberosa* f. *typica*, the regression lines are only applied for the data of *L. sinensis* and ?*L. dorsotuberosa* f. *postilirata*, which show high correlation coefficients of 0.94 and 0.96, respectively.

In our study, a high correlation between Sr/Ca and Ba/Ca was observed (Figure 3.6), with correlation coefficients of 0.94 for *L. sinensis* and 0.96 for ?*L. dorsotuberosa* f. *postilirata*. The ratios from ?*L. dorsotuberosa* f. *typica* are not taken into account since only four shells of this taxon were investigated, although their values seem to match well with the regression line of *L. sinensis* (Figure 3.6). The high correlation seems to indicate that the variability of Sr and Ba in the shells may be driven by the same mechanisms. Since the Sr/Ca time series shows good agreement with the reconstructed lake level changes (see section 4.1), the fluctuations of Ba/Ca (Figure 3.5) are also likely controlled by

the P/E balance, and possibly track the past solute evolution in the lake system during the Holocene period. However, no firm conclusion can be drawn here, because of the poor understanding of ostracod Ba uptake and Ba behaviour in the water of Nam Co. It is also noted that ?*L. dorsotuberosa* f. *postilirata* exhibits higher Ba abundances (higher Ba/Ca, Figure 3.6) than *L. sinensis* when similar Sr/Ca is detected for both taxa. This could be due to the specific microhabitat influencing uptake of trace metals into ostracod calcite (Ito and Forester, 2009).

### 3.4.3 U/Ca ratios

Uranium exists in oxygenated seawater as soluble U(VI) in the form of carbonate complexes (e.g., $UO_2(CO_3)_3^{4-}$, Ku et al., 1977; Langmuir, 1978). In anoxic environments, soluble U(VI) is reduced to insoluble U(IV) and precipitated as uraninite, $UO_2$, into sediments (Langmuir, 1978). U/Ca in foraminiferal calcite has been demonstrated to be related to the U/Ca ratio of the host water (Russell et al., 1994; 2004), and therefore provides the potential to reflect past redox conditions in the marine environment. U/Ca ratios in ostracod calcite have been examined to infer past oxygen levels in the bottom water of the deep lake Issyk-Kul, Kyrgyzstan (Ricketts et al., 2001). Decreasing U/Ca in ostracod shells are supposed to reflect lower oxygen availability in the lake bottom waters (Ricketts et al., 2001).

The redox condition in lake water depends mainly on two factors: organic matter flux (including productivity in the lake system and terrestrial organic material input) and vertical mixing of the water column. Increased decomposition of organic matter consumes more oxygen in the host water, thus resulting in more reducing conditions at the lake floor. Deeper water columns normally result in less oxygenated conditions in the bottom water, since they more easily become stratified and are less readily mixed by wind or inflow. Lower oxygen levels in the bottom waters, driven by high organic matter flux and weak mixing, can further enhance the reducing conditions in the lake sediments and even trigger the microbially mediated reduction of sulphate in the pore water (Ricketts et al., 2001). The by-product, $HS^-$, of sulphate reduction, which may migrate up to the bottom water, effectively removes soluble U(VI) from the bottom and pore waters by reducing $UO_2(CO_3)_3^{4-}$ to insoluble $UO_2$ (Klinkhammer and Palmer, 1991), and therefore inhibits U availability for ostracod uptake (Ricketts et al., 2001). As reported by Kasper et al. (2013), authigenic pyrite ($FeS_2$) framboids were found in NC 08/01 between ~4 and ~2 cal ka BP, indicating that sulphate reduction occurred in the sediments of Nam Co during some periods of the Holocene. Kasper et al. (2013) further suggested

that the redox conditions in the sediments and bottom waters of Nam Co were dominated by lake level changes (water column mixing) and organic matter influx (mainly originated from aquatic biomass production).

Based on the fluctuations of U/Ca for the three taxa from both sediment cores (Figure 3.5), and the total sulphur (TS) record of NC 08/01, which has been interpreted to reflect reducing conditions in the sediments (Doberschütz et al., 2013), the possible relationship between the past redox changes in the bottom waters and ostracod U/Ca ratios is discussed here. As shown in Figure 3.5, low TS was observed from ~11.4 to ~10.9 cal ka BP, perhaps implying a relatively oxic condition in the sediment as well as the bottom water, caused by the lowering lake level and less organic matter flux under drier and colder conditions (Doberschütz et al., 2013). However, lower U/Ca in the shells was detected for this period, apparently pointing to more depleted oxygen levels at the lake floor. A possible explanation for this discrepancy is that colder conditions during this period would have induced prolonged ice coverage at Nam Co and decreased oxygen availability in the host water, thus resulting in enhanced reducing condition at the lake bottom (Doberschütz et al., 2013). During 2005-2006, a 5-month ice coverage with a maximum ice thickness of more than 50 cm was observed at Nam Co (Li et al., 2008b), indicating that ice coverage may have a strong influence on the lake system. On the other hand, the TS proxy in the NC 08/01 sediments has a decadal resolution (Doberschütz et al., 2013), and is probably less affected by the seasonal effect of ice coverage.

From ~10.9 to ~9.1 and ~6.7 to ~4.8 cal ka BP, U/Ca ratios for the shells from NC 08/01 exhibit stable and low values, in accordance with relatively high TS contents, probably implying less oxygenated bottom water with higher lake levels and more aquatic biomass production. This inference is supported by the reconstructed warmer and wetter climatic conditions at Nam Co during this interval (Doberschütz et al., 2013). An overall increase of U/Ca in NC 08/01 was observed between ~1.3 and ~0.2 cal ka BP, corresponding to low TS in the sediments (Figure 3.5), indicating a shift to an enhanced oxygen level at the lake floor, probably caused by a lowering lake level and less organic material input (Kasper et al., 2012, 2013; Doberschütz et al., 2013). The low values of U/Ca around ~1.3 and ~0.4 cal ka BP could be due to the ice coverage effect and/or temporary lake level rises under short-term wet spells (Mügler et al., 2010; Wrozyna et al., 2012). In addition, higher U/Ca in the shells from Nam Co 8 is detected from ~6.7 to ~0.2 cal ka BP, in spite of the low sampling resolution, possibly due to the shallower water at the core location resulting in relatively high oxygen levels.

### 3.4.4 Rare earth elements in ostracod calcite

The concentration of fourteen REEs in single ostracod shells has been determined in our study. To our knowledge, no REEs in ostracod calcite have been reported yet. Therefore the distribution of these elements in ostracod shells and their incorporation process is still unexplored. According to previous studies, most of REEs in foraminifera tests are present in the associated Fe-Mn and/or organic contaminants with the shells, and only a minor part of the REEs are lattice-bound in foraminiferal calcite (Palmer, 1985; Haley et al., 2005; Roberts et al., 2012). The Fe-Mn cycling in the host water may induce the formation of ferromanganese oxides under oxic condition or of carbonates under reducing conditions (De Barr et al., 1988; Elderfield et al., 1990; Haley et al., 2004). These authigenic components, as well as organic materials originated from primary production in the host water and/or terrestrial input, have been demonstrated to have a strong affinity to REEs, and hence can effectively incorporate REEs from the water by adsorption and complexation. Therefore, their association with foraminiferal shells in the water column or after shell burial can significantly elevate REE abundances in the specimens. In our study, the ostracod shells are generally well preserved and hyaline without visible coatings. No significant enrichment of Fe, Mn or REEs on the shell surface was found based on repetitive line scans on the same line for some of our specimens, indicating a limited influence of these contaminants. This could be due to less active Fe-Mn behaviour at Nam Co, since ferromanganese oxides or carbonates were rarely detected in the sediments and Fe and Mn mainly exist in inorganic detrital materials (such as clay minerals and dolomites, Li et al., 2008b; Mügler et al., 2010). Moreover, Lake Nam Co is a typical oligotrophic lake with rather low productivity and terrestrial organic input (Yuan et al., 2002; Li et al., 2008a; Liu et al., 2008; Kasper et al., 2013), and thus organic associations with the shells should be minor. The cleaning process using hydrogen peroxide (see section 2.2) may also have effectively removed organic contaminants on the shell surface. However, due to the higher REE contents in Fe-Mn and organic contaminants, their minor occurrence would have significant influence on ostracod REEs considering the quite low REE concentrations in the shells (Tables 3.2 and 3.3). Therefore, further studies on more ostracod shells, especially living shells from this area, are necessary to evaluate the variations of ostracod REEs during taphonomy and diagenesis.

If we assume that the measured REEs mainly come from the ostracod calcite structure, the REEs in the shells are likely to reflect the REE characteristics in the host water. The chondrite-normalized REE patterns for the three taxa and bank soils at Nam Co are shown in Figure 3.7. It is noted that the

*L. sinensis* shells from both cores show consistent patterns (distinct LREE enrichment, Eu depletion and relatively flat HREEs) with the bank soils, indicating a possible linkage between them. As the bank soils are the major source for REE input into Nam Co (Li et al., 2011), the dissolved REEs in the lake water could be produced by weathering of REE-bearing detrital materials transported into the lake. Therefore, REEs in the shells may be indirectly influenced by the soil source when ostracods incorporate dissolved REEs from the water. However, flatter REE patterns were observed for ?*L. dorsotuberosa* f. *typica* and ?*L. dorsotuberosa* f. *postilirata*, with a weaker Eu anomaly relative to *L. sinensis* and bank soils (Figure 3.7) . This might be caused by the potential species -specific incorporation of trace metals (Ito and Forester, 2009) and/or the possible different microhabitat conditions for these species. As expected, the ostracod shells exhibit significantly lower REE contents than the soil samples (Figure 3.7), which contain a substantial amount of clay minerals (up to 20%), favouring REE enrichment (Li et al., 2011). Less LREE enrichment was also detected in the shell samples, with the average LREE/HREE ratio of 4.5 for ?*L. dorsotuberosa* f. *postilirata*, 5.7 for *L. sinensis* and 7.8 for ?*L. dorsotuberosa* f. *typica*, compared to 10.8 for the bank soils (Li et al., 2008a).

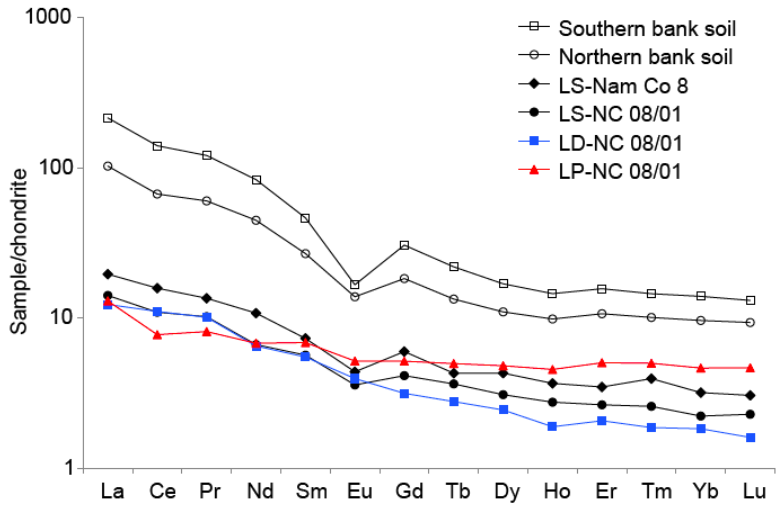


Figure 3.7: Average chondrite-normalized REE patterns (Haskin et al., 1968) for *L. sinensis* (LS), ?*L. dorsotuberosa* f. *typica* (LD) and ?*L. dorsotuberosa* f. *postilirata* (LP) from both sediment cores (Nam Co 8 and NC 08/01) and southern and northern bank soils of Lake Nam Co (Li et al., 2008a).

La/Ca ratios for the three taxa are shown in Figure 3.5, presenting relatively constant values for most of the shells in view of the uncertainty ranges. The La/Ca ratios show different variation patterns from those of Ti in NC

08/01, which is considered to reflect the detrital material input into the lake (Doberschütz et al., 2013), as well as from those of Mg/Ca, Sr/Ca and U/Ca. This suggests that REEs in the shells were not simply controlled by one of the factors controlling those variables (i.e., the P/E balance, the redox condition in the host water, or the terrestrial input). The REE behaviour in the lake waters of Nam Co is still unknown. However, previous studies (Millero, 1992; Johannesson and Lyons, 1994; Johannesson et al., 1995) suggested that dissolved REEs in alkaline lakes with carbonate ions as a major component tend to form stable carbonate complexes [$RCO_3^+$ and $R(CO_3)_2^-$, where R refers to REE]. On the other hand, the solubility products for REE carbonates [$R_2(CO_3)_3$] are quite low, ranging from $10^{-35}$ to $10^{-29}$ (Smith and Martell, 1976; Firsching and Mohammadzadel, 1986), meaning that the host water becomes easily saturated with respect to dissolved REEs in the presence of high carbonate concentrations . Considering the high pH level (around 9.3) in Lake Nam Co with relatively high carbonate ion contents (at a magnitude of $10^{-3}$ mol $l^{-1}$, Keil et al., 2010), the saturation concentrations for dissolved REEs would be as low as $10^{-13}$ to $10^{-10}$ mol $l^{-1}$. Therefore, it is likely that the levels of dissolved REEs are more or less constant in this lake due to saturation, causing the relatively constant REEs in the shells during the ostracod uptake process. An alternative possible explanation for the low La/Ca variability is that REEs, as non-bioessential trace elements (Palmer, 1985), may be excluded during the ostracod biomineralization process. Thus, ostracods would tend to inhibit the REE uptake and maintain these metals in a low concentration range in their carapaces. Or, if Fe-Mn and/or organic contaminants do occur, these components may overprint the original REE information in ostracod calcite and induce similar REE contents in the samples when similar amounts of these contaminants are associated with the shells.

## 3.5 Conclusions

LA-ICP-MS has been proven to be a useful technique for in-situ trace element determination in single ostracod shells. Due to a higher sample mass ablated per scan, the line-scan method provides more precise results compared to spot analysis and is therefore more appropriate for single shell measurement. No significant species-related difference in shell composition was detected in our study. However, this conclusion needs to be tested by further studies.

Mg/Ca and Sr/Ca in ostracod calcite have been used widely as paleosalinity indicators in previous studies. Both ratios seem to be also applicable in the Nam Co area. Variations of Ba, U and REEs in the samples are discussed in this paper. However, no distinct conclusion can be drawn here,

mainly due to the unknown behavior of these metals in the host water and uncertainties regarding their distribution and uptake process in the ostracod shells. Since the concentrations of U and REEs in the specimens are rather low, post-depositional changes, such as contaminant association with the shells after burial and diagenetic alternations, have the possibility to influence shell compositions. Therefore, more research on shells from living ostracods from this area is essential to evaluate the possible extent of these post-depositional alternations. If a clear relationship between the concentrations of these metals in ostracod shells and their levels in the host waters could be established by future field collection and laboratory cultivation, they may provide valuable insights into the past hydrological and hydrochemical changes in aquatic environments.

## Acknowledgements

This work is part of the DFG priority programme 1372 “TiP: Tibetan Plateau – Formation – Climate – Ecosystem”, grant no. MA1308/23-1. Q.Y. thanks the Max Planck Graduate Centre in Mainz, Germany, for financial support.

# Chapter 4

# Lead isotope and trace element variability during the Penultimate Interglacial in a stalagmite from the Hüttenbläserschachthöhle, north-western Germany

This chapter is submitted as Yang Q, Scholz D, Jochum KP, Hoffmann DL, Stoll B, Weis U, Schwager B, Andreae MO (2014) Chemical Geology.

## 4.1 Introduction

Speleothems, such as stalagmites and flowstones, have been widely used as paleoclimate archives (e.g., McMillan et al., 2005; Spötl et al., 2008; Wang et al., 2008; Wassenburg et al., 2012). They often have long continuous growth periods that can be dated precisely and accurately by U-series methods (Scholz and Hoffmann, 2008), and provide multiple paleoenvironmental proxies that can be analysed at high resolution (Fairchild et al., 2006). Moreover, the occurrence of speleothems in all continental areas provides the opportunity for comparison of past climate changes in different regions (Henderson, 2006). The most commonly measured proxies in speleothems are the carbon and oxygen isotope ratios ($\delta^{13}C$ and $\delta^{18}O$), which have been utilized to reconstruct soil/vegetation dynamics (e.g., Genty et al., 2003) and temperature/precipitation changes (McDermott, 2004), respectively. Recently, speleothem trace element records have received increased attention for reconstruction of paleohydrological processes (Treble et al., 2003; Fairchild et al., 2006; Borsato et al., 2007; Fairchild and Treble, 2009; Wassenburg et al., 2012, 2013). Isotope ratios, such as $^{87}Sr/^{86}Sr$, $^{234}U/^{238}U$ and $\delta^{34}S$, provide the potential to record atmospheric fluxes or local hydrological conditions (Goede et al., 1998; Zhou et al., 2005; Wynn et al., 2008). Finally, analysis of fluorescent organic material in speleothems enabled recognition of flushing events of the cave systems during historical periods (Baker et al., 2002).

In environmental sciences, the radiogenic isotopes $^{206}Pb$, $^{207}Pb$ and $^{208}Pb$, as products of the radioactive decay of $^{238}U$, $^{235}U$ and $^{232}Th$, respectively, have been extensively applied for tracing both global and local Pb pollution sources due to their conservative behaviour and preferential resistance during physico-

chemical fractionation processes (Komárek et al., 2008). Investigations of Pb isotope ratios in different environmental archives, such as atmospheric aerosols, peat deposits, lake/stream sediments, soils, etc., can discern the contribution of different anthropogenic Pb contaminants, such as leaded gasoline, coal combustion, metallurgical activities and waste incineration (Monna et al., 1997; Hansmann and Köppel, 2000; Ettler et al., 2004; Carignan et al., 2005). Under natural conditions, geogenic Pb isotopes can be used to identify potential sources of Pb ore deposits and the tectonic conditions of their formation (Large et al., 1983; Krahn and Baumann, 1996; Stückrad et al., 2008). U-Pb dating was demonstrated to be a promising method for speleothem chronology, in particular for older samples than the dating range of the $^{230}Th/U$ method (Richards et al., 1998; Bajo et al., 2012). However, to our knowledge, Pb isotopes have not been used as paleoenvironmental proxies in speleothem studies. Since Pb in speleothems is mainly derived from the epikast and the soil zone (Fairchild and Treble, 2009), Pb isotope ratios may provide an insight into varying contribution of different Pb sources and local hydrological conditions.

Here, an aragonitic stalagmite collected from the Hüttenbläserschachthöhle, north-western Germany, has been investigated for a set of trace elements (such as Sr, Mg, Al, Si, Mn, Th, P and Pb) and Pb isotope ratios. We provide a preliminary interpretation of Pb isotope ratios ($^{207}Pb/^{206}Pb$ and $^{208}Pb/^{206}Pb$) and also discuss potential hydrological changes during Marine Isotope Stage (MIS) 7 based on the observed trace element variations.

## 4.2 Material and methods

### 4.2.1 Study area and sampling

The Hüttenbläserschachthöhle (Figure 4.1) is situated in the Middle- to Upper Devonian limestone of the Sauerland Mountains (Northern Rhenish Massif, north-western Germany; Burchette, 1981) and is one of the biggest caves of the Iserlohn cave system. This cave was discovered in 1993 and has a length of 4,360 m with an elevation difference of 46 m (Grebe, 1994). The Iserlohn cave region is covered by forest, with ridges and valleys generally following the west-south-west east-north-east strike of the rock formation (Von Kamp, 1972). As reported by the nearby meteorological station Hagen Fley, the mean annual precipitation in the area is 850 mm, and the mean annual temperature is around 9.9 °C (Richter et al., 2004). Stalagmite HBSH-1 (Scholz et al., 2011) was retrieved deep inside the cave (Figure 4.1). HBSH-1 is approximately 55 cm long with a clearly visible lamination (Figure 4.2). It is mainly composed of aragonite,

with limited calcite content occurring in few short sections. Here we focus on an approximate 6 cm long section from the bottom part of this stalagmite (i.e., corresponding to ca. 52 to 46 cm distance from top, Figure 4.2).

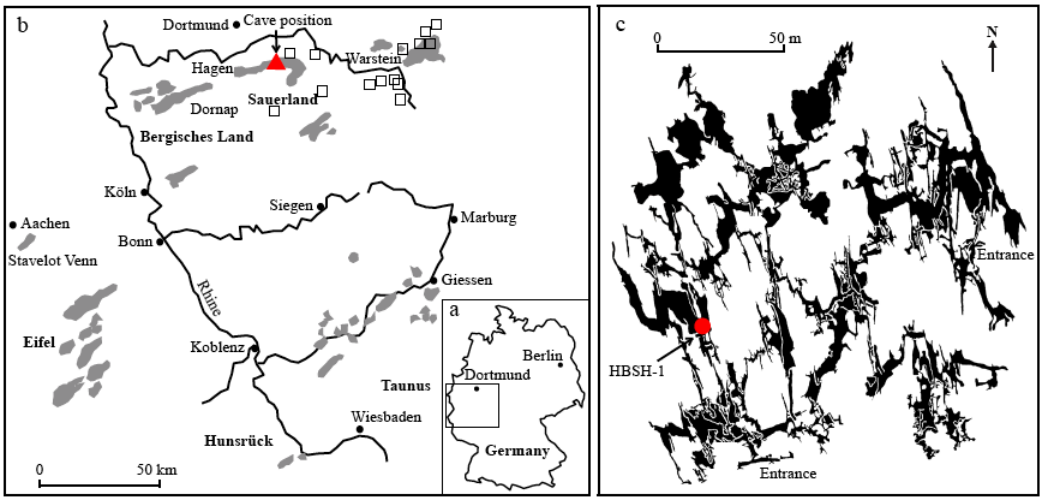


Figure 4.1: (a) Location of the study area in north-western Germany. (b) Location of the Hüttenbläserschachthöhle (red triangle), associated with the massive Devonian limestones (grey areas) in the region and the galena deposits (black squares) in the northern Sauerland (Large et al., 1983). (c) Cave map of Hüttenbläserschachthöhle with the sampling location of HBSH-1 (red dot, revised from Grebe (2007) and Niggemann et al. (2003)).

### 4.2.2 $^{230}$Th/U dating

Seven sub-samples, weighing 10-15 mg, were drilled as powders from the bottom part of HBSH-1. The chemical pretreatment for these sub-samples was performed as described by Hoffmann (2008). Following dissolution in $HNO_3$, a defined quantity of a mixed $^{229}Th/^{233}U/^{236}U$ spike was added into the sub-sample solutions. The solutions were dried down for sample-spike equilibration. The obtained residues were dissolved in $HNO_3$, HCl and $H_2O_2$ to decompose the organic components and then dried down again. Afterwards, the residues were dissolved in 6N HCl and then passed through ion exchange resin (AG 1×8) to separate Th and U fractions. Th and U were eluted from the resin using 6N HCl and 1N HBr and MilliQ $H_2O$, respectively. The Th and U fractions were dried down, then dissolved in 7N $HNO_3$, and separately processed through the resin for purification. Th was eluted by 6N HCl and U by 1N HBr and MilliQ $H_2O$. Both fractions were dried down and then dissolved in 0.8 N $HNO_3$ for the dating measurements.

$^{230}$Th/U dating was performed with a Nu plasma MC-ICP-MS (multi-collector-inductively coupled plasma-mass spectrometer) at the Max Planck Institute for Chemistry (MPIC), Mainz, Germany. This instrument is equipped with twelve Faraday cups and three SEM ion counting detectors (Jochum et al., 2011b). U and Th were measured separately. A standard-sample bracketing procedure was applied in order to derive correction factors for mass fractionation and Faraday cup to SEM gain (Hoffmann et al., 2007). A Cetac Aridus nebulizer with a PFA spray chamber was used to introduce samples into the ICP-MS (Jochum et al., 2011b). Prior to analysis, the tuning process (including the torch position, gas flows and ion lenses) was performed to obtain the highest intensities and optimal peak shapes on the Faraday cups. Different measurement routines for the standards and samples were performed, depending on their $^{238}$U and $^{232}$Th contents. Each standard/sample measurement was followed by a wash out procedure (including MilliQ $H_2O$, mixed solution of 0.8N $HNO_3$ and 0.05N HF, 0.8N $HNO_3$). The tail contribution to $^{229}$Th, $^{230}$Th, $^{233}$U and $^{234}$U was estimated by measuring the half-masses around the corresponding peaks, such as 229.5, 230.5, 233.5 and 234.5. Data reduction was processed off-line, during which SEM nonlinearity, mass fractionation, Faraday cup to SEM gain, background intensities and tail contribution were corrected (Jochum et al., 2011b). Further methodological details can be found in several related publications (Hoffmann et al., 2007; Jochum et al., 2011b; Žák et al., 2012).

### 4.2.3 Trace element and Pb isotope analyses

The concentration of a set of trace elements (Sr, Mg, Al, Si, Mn, Th, P and Pb) and lead isotope ratios ($^{207}$Pb/$^{206}$Pb and $^{208}$Pb/$^{206}$Pb) in HBSH-1 were determined using the high-resolution sector-field ICP-MS Thermo Element2, combined with the 213 nm (UP-213, for trace elements) and 193 nm (UP-193SS, for Pb isotopes) Nd:YAG laser ablation systems from New Wave at the MPIC, Mainz, Germany. Trace element analyses were performed along the growth axis of HBSH-1 using an 80 μm spot size and 100 μm step width. The details for the laser ablation system operation are shown in Table 4.1. The measured isotopes (i.e., $^{88}$Sr, $^{25}$Mg, $^{27}$Al, $^{29}$Si, $^{55}$Mn, $^{232}$Th, $^{31}$P and $^{208}$Pb) are interference-free as demonstrated by Jochum et al. (2012) performing experiments using medium-mass resolution ($m/\Delta m$ = 4000). In this study, all element analyses were performed in the low-mass resolution mode ($m/\Delta m$ = 300) of the mass spectrometer, using a combination of electrical and magnetic scan modes. The operating parameters for the ICP-MS are listed in Table 4.2. To avoid potential surface contamination, the first three to five scans of each spot analysis were excluded. Data reduction was carried out by calculating the blank corrected count rates of the analysed

isotopes relative to the internal standard $^{43}Ca$. The silicate reference glass NIST SRM 612 and carbonate reference materials MACS1 and MACS3 were used for external calibration of the trace element analyses (Jochum et al., 2011a, 2012).

Table 4.1: Operating parameters for the laser ablation system UP-193SS and UP-213.

| Laser ablation system | UP-213 | UP-193SS |
|---|---|---|
| Spot size (μm) | 80 | 110 |
| Step width (μm) | 100 | 200 |
| Dwell time (s) | 80 | 95 |
| Warm up time (s) | 18 | 13 |
| Washout time (s) | 30 | 45 |
| Pulse repetition rate (Hz) | 10 | 10 |

Table 4.2: Operating parameters of the Element2 ICP-MS.

| Operating parameters | Trace elements | Pb isotopes |
|---|---|---|
| RF power (W) | 1180 | 1270 |
| Cooling gas flow rate (l $min^{-1}$) | 16 | 15 |
| Carrier gas (Ar) flow rate (l $min^{-1}$) | 0.4 | 0.8 |
| Carrier gas (He) flow rate (l $min^{-1}$) | 0.8 | 0.6 |
| Samples per peak | 120 | 100 |
| Time per pass (s) | 0.7 | 0.07 |
| Mass window (%) | 10 | 10 |
| Mode of analysis | A combination of electrical and magnetic scan mode | Electrical scan mode |

Detection limits for trace element measurements are shown in Table 4.3. It needs to point out that the detection limits could change by a factor of three to four per sequence depending on the measurement conditions (Wassenburg et al., 2012). To evaluate the reproducibility of LA-ICP-MS for elemental concentration determination, SD (standard deviation) and RSD (relative standard deviation, in percent) values were calculated based on the results of MACS1 measurements (Table 4.3). The obtained MACS1 elemental concentrations and corresponding SD values show good agreement with the published values by Jochum et al. (2012; 2014).

Pb isotope analyses were performed parallel to the measuring track of trace elements using a spot size of 110 μm and step width of 200 μm (Table 4.1). The distance between the two tracks is < 0.5 mm. Measurements were carried

Table 4.3: Detection limits and reproducibility of elemental concentration determination in our study.

| Element | Detection limit (µg $g^{-1}$) | Concentration in MACS1 (µg $g^{-1}$) | Reproducibility (SD, µg $g^{-1}$) | RSD (%) |
|---|---|---|---|---|
| Sr | 0.03 | 180 | 14 | 8 |
| Mg | 0.2 | 9.6 | 0.9 | 9 |
| Al | 0.1 | 25 | 3 | 12 |
| Si | 30 | 85 | 21 | 25 |
| Mn | 0.06 | 104 | 7 | 7 |
| Th | 0.0002 | 0.01 | 0.001 | 11 |
| P | 2 | 2.7 | 0.9 | 33 |
| Pb | 0.005 | 88 | 8 | 9 |

SD: standard deviation. RSD: relative standard deviation.

out using the fast electrical scan mode with 0.075 s per pass for the mass scan of $^{206}Pb$, $^{207}Pb$ and $^{208}Pb$, resulting in a nearly simultaneous analysis for all three isotopes (Jochum et al., 2006a). $^{204}Pb$ was not determined due to its low abundance in the samples and the interference of $^{204}Hg$. Each run included approximately 300 blank and 2,000 measurements. To compensate for the count rate decrease during spot analyses, data reduction was performed by calculating the blank corrected Pb isotope ratios for each pass followed by averaging the ratios (Jochum et al., 2006a). The silicate reference material KL2-G was used to correct mass discrimination, while the silicate reference material ATHO-G was used to access the measurement accuracy (Jochum et al., 2006a, 2011b). Based on the correction factors derived from the KL2-G results, the obtained ratios of $^{207}Pb/^{206}Pb$ and $^{208}Pb/^{206}Pb$ in ATHO-G (Table 4.4) agree well with the published values by Jochum et al. (2011b). SD and RSD values for both lead isotope ratios in KL2-G and ATHO-G were also calculated (Table 4.4), which suggested an external precision of 0.3-0.5% for lead isotope measurements by LA-ICP-MS with lead concentration ranging from 2 to 6 µg $g^{-1}$.

Table 4.4: Lead isotope ratios and related SD (standard deviation) and RSD (relative standard deviation) values in KL2-G and ATHO-G obtained in our study.

| | Pb concentration (µg $g^{-1}$)[a] | $^{207}Pb/^{206}Pb$ | SD | RSD (%) | $^{208}Pb/^{206}Pb$ | SD | RSD (%) |
|---|---|---|---|---|---|---|---|
| KL2-G | 2.07 | 0.8213 | 0.0036 | 0.44 | 2.0260 | 0.0104 | 0.51 |
| ATHO-G | 5.67 | 0.8421 | 0.0022 | 0.26 | 2.0730 | 0.0071 | 0.34 |

[a] Pb concentration data in KL2-G and ATHO-G are derived from Jochum et al. (2006b).

## 4.3 Results

### 4.3.1 Age-depth model

The $^{230}Th/U$ dating results are shown in Table 4.5. All samples were taken from the aragonitic sections of HBSH-1. Due to the relatively high U content (at the μg $g^{-1}$ level), the analytical errors of the $^{230}Th/U$-ages are relatively small (Table 4.5). The activity ratios of ($^{230}Th/^{232}Th$) are high, implying negligible contents of detrital Th. Nevertheless, all ages have been corrected for potential detrital contamination assuming a bulk Earth $^{232}Th/^{238}U$ weight ratio of 3.8 for the detritus and $^{230}Th$, $^{234}U$ and $^{238}U$ being in secular equilibrium (Table 4.5). The difference between the corrected and uncorrected ages is insignificant for all samples.

Table 4.5: $^{230}Th/U$ dating results for the bottom section of HBSH-1.

| Distance from top (mm) | $^{238}U$ (μg $g^{-1}$) | ($^{230}Th/^{238}U$) | ($^{234}U/^{238}U$) | ($^{230}Th/^{232}Th$) | Uncorrected age (ka) | Corrected age (ka) |
|---|---|---|---|---|---|---|
| 457 | 5.22 ± 0.05 | 1.356 ± 0.010 | 1.529 ± 0.003 | 10520 ± 166 | 188.54 ± 3.25 | 188.53 ± 3.25 |
| 460 | 4.26 ± 0.04 | 1.356 ± 0.005 | 1.519 ± 0.002 | 4127 ± 40 | 192.01 ± 1.96 | 191.99 ± 1.94 |
| 464 | 5.19 ± 0.05 | 1.371 ± 0.006 | 1.526 ± 0.003 | 3925 ± 37 | 194.80 ± 2.23 | 194.79 ± 2.28 |
| 488 | 3.58 ± 0.03 | 1.351 ± 0.011 | 1.496 ± 0.003 | 7773 ± 118 | 198.34 ± 3.99 | 198.33 ± 3.92 |
| 492 | 4.28 ± 0.04 | 1.356 ± 0.005 | 1.496 ± 0.002 | 4150 ± 39 | 200.44 ± 2.03 | 200.43 ± 2.04 |
| 495 | 4.84 ± 0.04 | 1.334 ± 0.006 | 1.464 ± 0.003 | 433 ± 4 | 204.99 ± 2.70 | 204.84 ± 2.64 |
| 515 | 5.42 ± 0.06 | 1.288 ± 0.005 | 1.409 ± 0.002 | 2267 ± 21 | 209.99 ± 2.30 | 209.97 ± 2.27 |

Uncertainty is defined as the 2-sigma standard error.

The dated section of HBSH-1 contains an age interval of approximately 21 ka, from ~210.0 ka at 515 mm distance from top to ~188.5 ka at 457 mm. No age inversion was detected within the analytical uncertainties, which range from 1.9 to 3.9 ka (Table 4.5).

The age-depth model was established using the StalAge algorithm of Scholz and Hoffmann (2011) (Figure 4.2). Also shown are the corresponding 95% confidence limits. Note that the age model is quite linear for the whole section (Figure 4.2), and no hiatus or significant growth rate changes are observed. This suggests a relatively uniform, slow growth rate of 3.1 μm $a^{-1}$. Consequently, the 80 and 110 μm spot sizes for trace element and Pb isotope analyses correspond to a temporal resolution of 25.8 and 35.5 a, respectively.

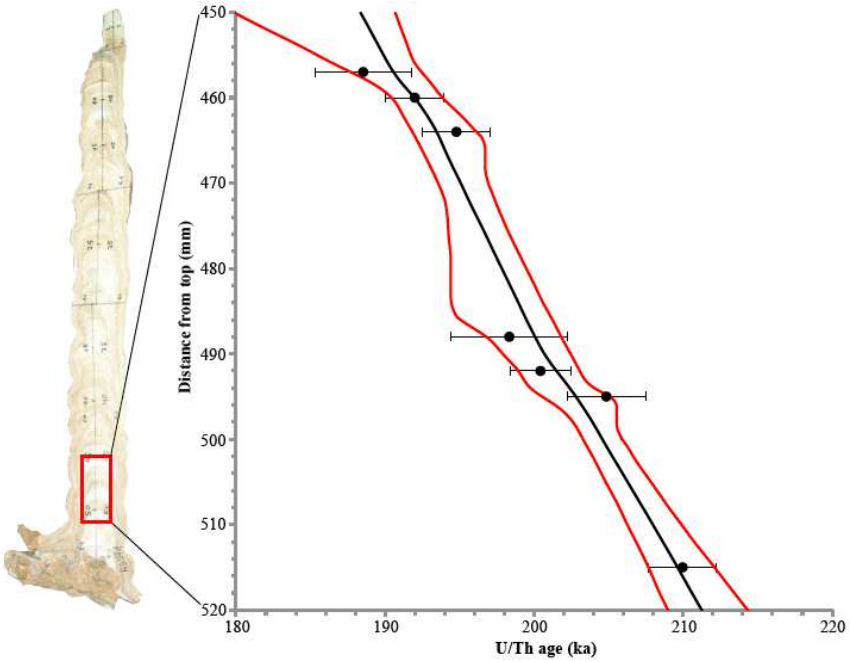


Figure 4.2: Picture of Stalagmite HBSH-1 (left panel) and the age-depth relationship (right panel) for its bottom section (marked by the red rectangle). The age model (black line) and the corresponding 95% confidence intervals (red lines) were calculated using the StalAge algorithm (Scholz and Hoffmann, 2011). Individual $^{230}Th/U$-data are presented with 2-sigma analytical uncertainties.

## 4.3.2 Geochemistry

The trace element concentration and Pb isotope ratios of the studied section of HBSH-1 are shown in Figure 4.3. Note that the Sr concentration, as expected for aragonites, are relatively high in this sample, ranging from 490 to 950 μg $g^{-1}$, with an average value of 640 μg $g^{-1}$ (Figure 4.3). Significant covariations are observed between the elements Mg, Al, Si, Mn, Th, P and Pb, showing high abundances between ~204.9 and ~201.5 as well as between ~198.4 and ~195.9 ka, and rather low contents between ~210.0 and ~204.9, ~201.5 and ~198.4 as well as between ~195.9 and ~190.0 ka (Figure 4.3). The maximum concentrations of Mg, Al, Si, Mn, Th, P and Pb are 720, 4200, 16300, 330, 0.54, 430 and 16.7 μg $g^{-1}$, respectively, while the minimum concentrations can be as low as tens of μg $g^{-1}$ (such as Si and P), or several μg $g^{-1}$ (Mg) or even lower than 1 μg $g^{-1}$ (Al, Mn, Th and Pb). Higher P is also detected from ~195.9 to ~193.1 ka.

As shown in Figure 4.3, variations of $^{207}Pb/^{206}Pb$ and $^{208}Pb/^{206}Pb$ are in phase with those of Mg, Al, Si, Mn, Th, P and Pb, in the sense that high, but

relatively constant Pb isotope ratios prevail during those periods when the trace element concentrations are high, albeit variable. It is notable that both ratios seem to have upper limits, i.e., ~0.86 for $^{207}Pb/^{206}Pb$ and ~2.11 for $^{208}Pb/^{206}Pb$. Troughs of $^{207}Pb/^{206}Pb$ and $^{208}Pb/^{206}Pb$, which can be as low as 0.73 and 1.84, respectively, mainly occur during the intervals with low element abundances (Figure 4.3).

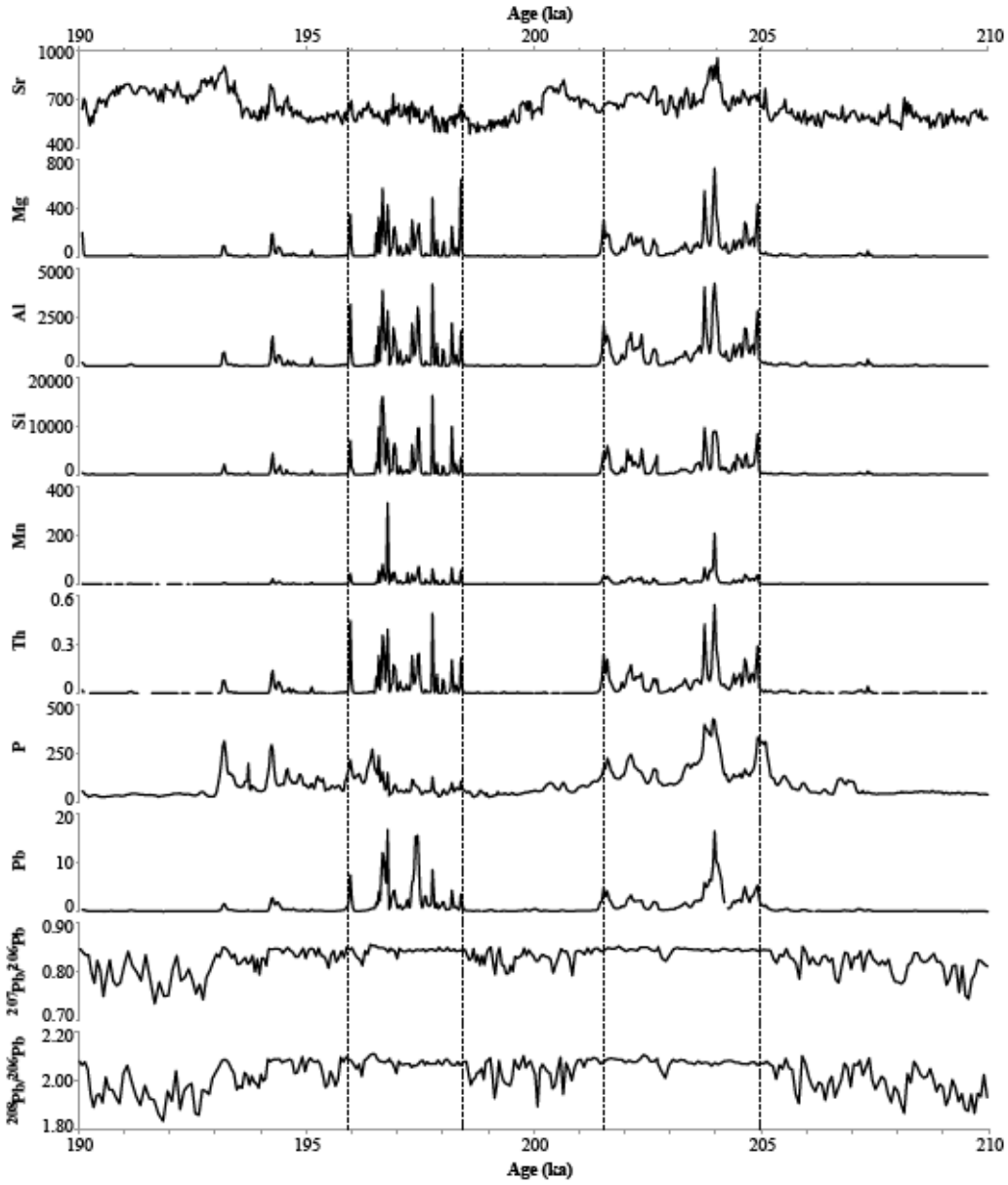


Figure 4.3: Trace element concentrations (in μg $g^{-1}$) and Pb isotope ratios in the bottom section of Stalagmite HBSH-1 plotted against age.

## 4.4 Discussion

### 4.4.1 Trace element variability

Speleothem Mg and Sr are mainly sourced from dissolution of carbonate host rock and weathering of the overlying regolith zones (Fairchild and Treble, 2009). Both elements show a preference to be transported as solutes and tend to behave as free ions ($Mg^{2+}$ and $Sr^{2+}$) in cave water systems (Borsato et al., 2007). Deposition of aragonitic speleothems often indicates high Mg/Ca ratios in cave drip waters since $Mg^{2+}$ is known to be an inhibitor for calcite precipitation (Frisia et al., 2002; McMillan et al., 2005; Wassenburg et al., 2012, 2013). High Mg/Ca in cave drip waters could result from dissolution of dolomite minerals in the host rock and soil above the cave, or be due to prior calcite precipitation (PCP, Fairchild et al., 2006; Fairchild and Treble, 2009). PCP may occur when the infiltrating water encounters a gas phase with lower $pCO_2$ within the karstic aquifer or at the cave ceiling, causing degassing of $CO_2$, supersaturation of water with respect to $CaCO_3$ and, as a consequence calcite precipitation (Fairchild and Treble, 2009). Due to the low distribution coefficients for Mg and Sr between calcite and solutions ($D_{Mg}$ = 0.019 and $D_{Sr}$ = 0.072 at 15 °C; Huang and Fairchild, 2001), PCP results in an enrichment of Mg and Sr in both drip water and speleothems (Fairchild et al., 2006; Fairchild and Treble, 2009). PCP may not only induce deposition of aragonitic speleothems by elevating drip water Mg/Ca, but also the occurrence of prior aragonite precipitation (PAP) upflow to the drip sites (Wassenburg et al., 2012, 2013). Owing to the contrasting distribution coefficients between aragonite and solutions for Mg ($0.00002 \leq D_{Mg} \leq 0.00008$ or $D_{Mg} \approx 0.0007$ or 0.0017; Zhong and Mucci, 1989; Gaetani and Cohen, 2006; Gabitov et al., 2008) and Sr ($D_{Sr} \approx 1.2$; Gaetani and Cohen, 2006), drip waters may have increased Mg/Ca but decreased Sr/Ca subsequent to PAP. Therefore, a positive (negative) correlation between Mg and Sr in calcitic speleothems has often been linked to the occurrence of PCP (PAP) (Fairchild and Treble, 2009; Wassenburg et al., 2012, 2013). However, the relationship between the two elements may be disturbed in aragonitic samples due to their different physico-chemical properties in the aragonite matrix. Due to the similar ionic radii between $Sr^{2+}$ (1.2 Å) and $Ca^{2+}$ (1 Å), $Sr^{2+}$ ions are easily incorporated into the aragonite crystal lattice, whereas $Mg^{2+}$ is more difficult to be incorporated because of the discrepancy between the ionic radii of $Mg^{2+}$ (0.72 Å) and $Ca^{2+}$. Therefore, Sr in speleothem aragonite could be elevated by PCP or depleted by PAP, while Mg may remain relatively constant at trace levels in aragonitic specimens. However, Wassenburg et al. (2012; 2013) have reported higher Mg levels for some aragonitic speleothems. In these cases, it is very likely that Mg was not incorporated as free ions but mainly through absorption of the ions or

association with colloids and/or particles, such as clay minerals (Wassenburg et al., 2012; 2013).

As shown in Figure 4.3, the Sr concentration is relatively high throughout the whole profile, having an average of 640 μg $g^{-1}$, which is expected due to the preferential incorporation of Sr into the aragonitic matrix. Magnesium shows rather low abundances (several μg $g^{-1}$) within some sections of HBSH-1 (e.g., between ~210.0 to ~204.9, ~201.5 and ~198.4 and ~195.9 and ~190.0 ka, Figure 4.3), which could be explained by the low distribution coefficient of Mg in aragonite (Zhong and Mucci, 1989; Gaetani and Cohen, 2006; Gabitov et al., 2008). On the other hand, peaks with high Mg contents (hundreds of μg $g^{-1}$) are observed between ~204.9 and ~201.5 as well as between ~198.4 and ~195.9 ka, which seems unlikely to be mainly derived from incorporation of free Mg ions (Wassenburg et al., 2013). No distinct relationship between Sr and Mg is observed, and the correlation coefficient is -0.12 ($P < 0.001$). This is probably due to the different transportation and incorporation mechanisms of Sr (potentially as free ions) and Mg (probably mainly as non-ionic phases).

The transport and incorporation of Mg into HBSH-1 as non-ionic phases are supported by the distinct covariations between Mg and Al, Si, Mn, Th, P and Pb (Figure 4.3). As major constituents of clay minerals, Al and Si are mainly transported in colloidal and particulate forms in the karstic aquifer (Zhou et al., 2008; Fairchild and Treble, 2009). Therefore, high abundances of both elements in speleothems may be linked to increased detrital material input caused by enhanced water infiltration (Zhou et al., 2008; Wassenburg et al., 2012). Magnesium ions are easily absorbed by clay minerals because of charge deficits in their crystal structures (Brigatti et al., 2006). Therefore, an association of Mg with clay minerals is the most likely mechanism to generate high Mg abundances in aragonitic speleothems, especially when crystal growth is fast (Wassenburg et al., 2012, 2013). Thorium also tends to adsorb onto clay minerals, related to the extremely low solubility of Th ions ($Th^{4+}$) in aqueous solutions (Langmuir, 1978; Dorale et al., 2004). A covariation between Th and Al (Si) is thus expected for speleothems with a high Th content (Wassenburg et al., 2012).

Manganese and Pb can be mobilized as $Mn^{2+}$ and $Pb^{2+}$ ions in the infiltrating water, which would be derived from dissolution of the carbonate host rock and weathering of clastic soil components (Richter et al., 2004; Borsato et al., 2007; Wassenburg et al., 2012). Dissolved Mn and Pb may also form complexes with organic matter (such as soil humic substances), providing

organic colloidal sources for speleothem Mn and Pb (Richter et al., 2004; Borsato et al., 2007; Wassenburg et al., 2012). Alternatively, both metals can be transported as inorganic colloids and/or detrital particles and possibly be present as non-carbonate inclusions in speleothems (Zhou et al., 2008; Wassenburg et al., 2012). Manganese was found to be enriched in feldspar and clay minerals of loess sediments in the northern Rhenish Massif (Richter et al., 2004). Natural Pb in soils is mainly associated with residual silicate fractions (Teusch et al., 2001). In addition, many occurrences of galena (PbS)-bearing mineralization have been reported for the Sauerland, Germany (Large et al., 1983; Figure 4.1). Therefore, we assume that inorganic colloids and/or fine particles, possibly advanced by enhanced infiltration of water, are the main forms for transport and incorporation of Mn and Pb into HBSH-1, inducing the consistent variations between Mn, Pb, Al and Si. However, free ions and organic complexes may also contribute to a subordinate degree.

Various sources as well as transport and incorporation mechanisms for P in speleothems have been proposed (Fairchild and Treble, 2009). In the soil environment, dissolved P (inorganic phosphate ions) can be released by vegetation decay and microbial activity (Huang et al., 2001; Treble et al., 2003). This release may be enhanced at lower pH level (Giesler et al., 2005). As a consequence, warm and wet conditions would have multiple promoting effects on P release from the soil since increased soil temperature and water availability favour vegetation productivity and decomposition; enhanced water infiltration advances P transport capacity; higher $CO_2$ production due to increased microbial activity may result in decreased pH in the soil (Borsato et al., 2007). On the other hand, dissolved P can be chelated to organic acids, such as soil humic substances (Huang et al., 2001; Treble et al., 2003). Therefore, mobilization and incorporation as organic colloids may also be important for speleothem P (Borsato et al., 2007; Fairchild et al., 2010). Moreover, speleothem P can be sourced from apatite minerals contained in the carbonate host rock and the overlying soil layers, which means that P may also be transported as insoluble particles given the low solubility of apatite (Fairchild and Treble, 2009). In natural systems, all these mechanisms may occur simultaneously making the interpretation of speleothem P records a non-trivial task (Treble et al., 2003; Borsato et al., 2007; Fairchild et al., 2010; Wassenburg et al., 2012). However, as suggested by Borsato et al. (2007), P transport and incorporation, in different inorganic and organic forms, is generally facilitated by high water infiltration. Therefore, high P content in speleothems is likely to be linked to more active local hydrology, which could be caused by increased rainfall on short time scales or climate amelioration on longer time scales (Fairchild and Treble, 2009). This may explain the observed positive correlation between P and the other trace elements in HBSH-1 (Figure 4.3). On the other hand, the uncorrelated P variation

observed between ~195.9 and ~193.1 ka (i.e., a more distinct increase compared to Mg, Al, Si, Mn, Th and Pb) could be explained by complexation with organic acids (Huang et al., 2001; Zhou et al., 2008).

Based on the discussion above, we assume that Mg, Al, Si, Mn, Th, P and Pb in HBSH-1 are mainly transported and incorporated as colloids and/or particles resulting in the observed covariations. Enhanced water infiltration, likely caused by increased rainfall during these periods, would have favoured the mobilization of these elements in the karstic aquifer, consequently inducing higher elemental abundances in the stalagmite (i.e., from ~204.9 to ~201.5 and ~198.4 to ~195.9 ka, Figure 4.3). In contrast, lower recharge and drier conditions resulted in the rather low concentrations between ~210.0 and ~204.9, ~201.5 and ~198.4 as well as ~195.9 and ~190.0 ka (Figure 4.3). Strontium, perhaps mainly transported and incorporated as free ions, shows a different variation from the other elements.

### 4.4.2 Pb isotope ratios

To interpret the Pb isotope record in HBSH-1, it is necessary to evaluate the potential sources of Pb for this stalagmite. Since the age interval of HBSH-1 (~210.0 to ~190.0 ka, Figure 4.2) is very short compared to the half-lives of the parent isotopes (i.e., $4.466 \times 10^9$ a for $^{238}U$, $0.704 \times 10^9$ a for $^{235}U$ and $1.401 \times 10^{10}$ a for $^{232}Th$; Long, 1999), the in situ generation of Pb after deposition is negligible. Therefore, any variation of the Pb isotope ratios in HBSH-1 should reflect changes in the relative contribution of Pb from external sources with variable Pb isotopic compositions. These external sources may include atmospheric deposition of Pb as well as Pb derived from the carbonate host rock and the overlying soil. Since HBSH-1 was retrieved from deep inside the cave, direct deposition of Pb at the surface of the stalagmite by cave ventilation may be excluded. On the other hand, atmospheric deposition of Pb into the soil above the cave could indirectly influence the Pb isotope ratios recorded in the stalagmite. However, taking into account the well-developed vegetation cover in the cave region, which was probably similar or even better developed during MIS 7 due to the corresponding climate amelioration (Spötl et al., 2008), regional dust mobilization and subsequent atmospheric deposition can be considered insignificant. The majority of Pb incorporated into HBSH-1 may, thus, originate from the host rock and/or soil cover.

To estimate the potential contribution of Pb from the carbonate host rock and the overlying soil to HBSH-1, it is essential to determine the Pb isotope ratios of the two sources. However, to our knowledge, the Pb isotope ratios of both the limestone and soil in the cave region have not been determined yet. Thus, we only provide a preliminary discussion of the Pb isotope variability in HBSH-1 here.

Lead-isotope diagrams (e.g., $^{208}Pb/^{206}Pb$ versus $^{207}Pb/^{206}Pb$, Figure 4.4) can be used to reflect the variation in the thorogenic and uragenic isotopes of lead (Haack et al., 2003). A correlation of the isotope ratios in such a diagram may indicate mixing of two components with distinct Pb isotope characteristics (Monna et al., 2000; Haack et al., 2003): one represents lower $^{207}Pb/^{206}Pb$ and $^{208}Pb/^{206}Pb$ ratios (possibly related to geogenic background Pb), the other represents higher isotope ratios (possibly linked to ore Pb). As shown in Figure 4.4, $^{208}Pb/^{206}Pb$ and $^{207}Pb/^{206}Pb$ are significantly correlated in HBSH-1, with the correlation coefficient of 0.86 ($P < 0.001$), perhaps indicating a mixture of two Pb components. The point scatter along the regression line (Figure 4.4) may be due to the relative large analytical uncertainties [defined as 2RSE (relative standard error) ranging from 0.2 to 1.8%, depending on the corresponding Pb abundances], or due to the incorporation of more than two Pb components (Haack et al., 2003). However, considering the relatively large uncertainty of the Pb isotope ratios, the influence of the latter should be minor.

As discussed above, the two potential components of Pb with different isotope ratios are most likely derived from the carbonate host rock and/or the soil in the cave area. Large et al. (1983) reported Pb isotope data for different galena mineralizations in the northern Sauerland (Figure 4.1). The various occurrences of galena in the area (i.e., vein-types in quartzites and shales of Eifelian age and Palaeozoic country rocks, and disseminated mineralization in Cretaceous-Tertiary sediments) display relatively consistent Pb isotope ratios (Large et al., 1983). This may be due to a common source of Precambrian detritus for all genetically different Pb-Zn deposits in the area (Brown, 1965; Wedepohl et al., 1978). The results reported by Large et al. (1983) show a good agreement with the high Pb isotope ratios observed in HBSH-1 (Figure 4.4), perhaps indicating that galena minerals are the end-member with high Pb isotope ratios for the Pb mixing line described by the HBSH-1 data. This assumption is supported by several factors. First, as shown in Figure 4.5, higher $^{207}Pb/^{206}Pb$ and $^{208}Pb/^{206}Pb$ ratios are in phase with higher Pb concentrations in HBSH-1, indicating that the component with high isotope ratios may have higher Pb abundances, which is consistent with the Pb characteristics in the galena

deposits. In addition, as reported by Large et al. (1983), galena mineralization has occurred as disseminated phases in the Cretaceous-Tertiary sediments that filled karst cavities in the Devonian reef limestones. This implies that galena grains may be released by dissolution and weathering of the carbonate host rock and then incorporated into the stalagmite by the infiltrating water. Furthermore, due to the co-occurrence of galena, marl and clay minerals in karst cavities in the Devonian limestones (Large et al., 1983), these minerals may have been released simultaneously from the host rock by weathering processes and transported in the karstic aquifer. This would result in an in-phase enrichment of trace elements transported as colloids and/or particles (e.g., Al, Si and Pb, Figure 4.3) in HBSH-1 by enhanced water infiltration.

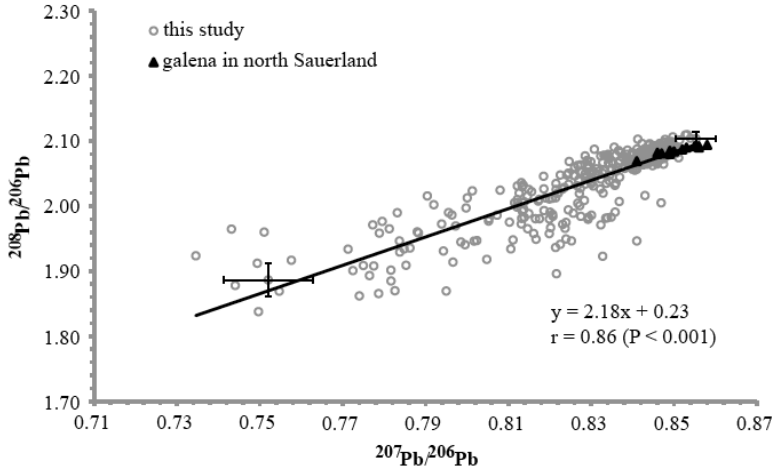


Figure 4.4: $^{208}Pb/^{206}Pb$ vs $^{207}Pb/^{206}Pb$ diagram for HBSH-1. Also shown are the Pb isotope data of galena from the northern Sauerland, Germany (Large et al., 1983). The uncertainties, defined as 2RSE (relative standard error), of our isotope ratios range from 0.2 to 1.8%, depending on the Pb abundances. For reasons of clarity, only the uncertainties for two data points (one with higher and one with lower ratios) are shown here (error bars). A regression line for our stalagmite data is also plotted.

Another potential source for the end-member with high Pb isotope ratios may be the soil above the cave. Lead in soils can be derived from atmospheric deposition, litterfall and Pb incorporation from the underlying bedrock (Erel et al., 1997). As discussed above, the effect of atmospheric deposition should be minor for the cave region of HBSH-1, when anthropogenic Pb pollution can be excluded (Erel et al., 1997), which is definitely the case for the MIS 7 growth phase of HBSH-1 discussed here. Thus, as suggested by Erel et al. (1997), natural lead in soils developed on carbonate bedrock is mainly derived from non-

carbonate rock residue because the Pb in the carbonate fraction of the bedrock is more easily released by rainfall and/or groundwater flow. If this was the case for the soil above Hüttenbläserschachthöhle, the Pb isotope ratios of the soil should be comparable to those of the galena minerals in the cave area, which means that the overlying soil should have a similar influence (i.e., providing Pb with high isotope ratios) on the Pb isotope ratio recorded in HBSH-1. However, as currently no Pb isotope data for soil samples from the area are available, this assumption cannot be confirmed by our analytical data.

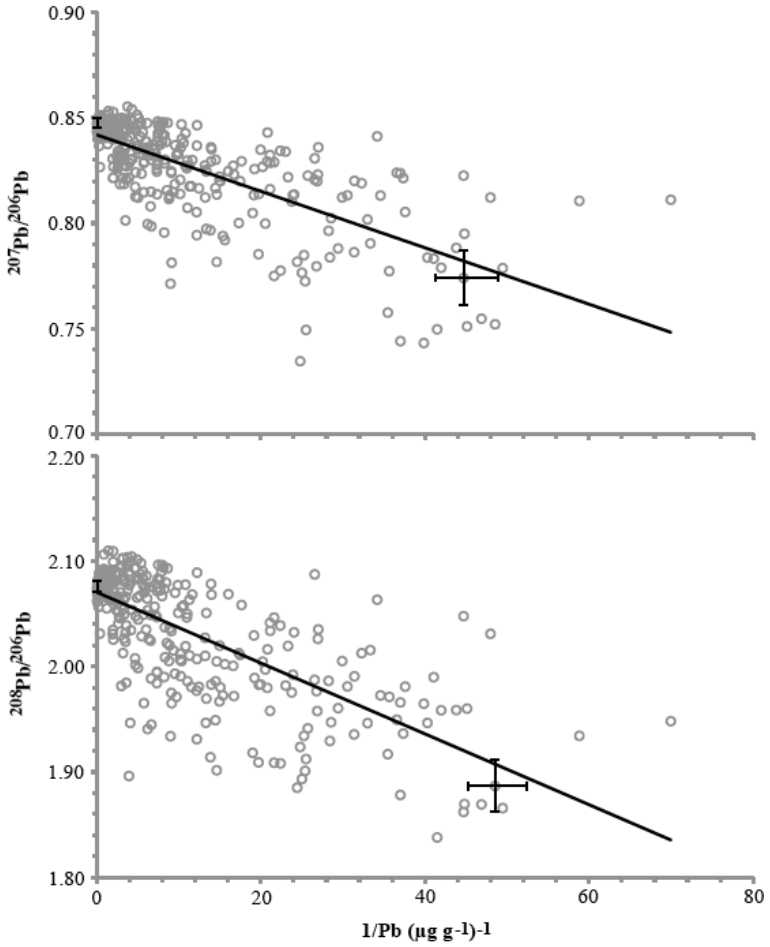


Figure 4.5: $^{207}Pb/^{206}Pb$ vs 1/Pb (upper panel) and $^{208}Pb/^{206}Pb$ vs 1/Pb (lower panel) diagrams for HBSH-1. Due to the different step widths for Pb concentration and isotope determination, only the concentration data having the consistent depths with the isotope ratios were plotted in this figure. The uncertainties, defined as 2RSE (relative standard error), of the Pb isotope ratios and concentrations range from 0.2 to 1.8% and 4.0 to 8.5%, respectively, depending on the Pb abundances. For reasons of clarity, only the uncertainties for two data points (one with higher and one with lower ratios) are shown (error bars) in each panel. The regression lines are also plotted.

The identification of the component with lower $^{207}Pb/^{206}Pb$ and $^{208}Pb/^{206}Pb$ ratios for HBSH-1 is more difficult, in particular due to the limited Pb isotope information available for the study region. As shown in Figure 4.5, lower Pb isotope ratios in HBSH-1 are generally related to rather low Pb concentrations. This indicates that the end-member with lower isotope ratios may come from a source with a low Pb concentration. A possible source for the Pb with lower isotope ratios in HBSH-1 is the carbonate fraction in the limestone host rock. As reported by previous studies (Smith et al., 1991; Erel et al., 1997), the Pb content of the carbonate fraction of limestones can be as low as 0.1 - 1 μg $g^{-1}$, which is comparable to the low Pb concentration observed in HBSH-1 (Figure 4.3). In addition, Smith et al. (1991) reported very low Pb isotope ratios ($^{207}Pb/^{206}Pb$ values down to 0.43 and $^{208}Pb/^{206}Pb$ down to 0.99) in the carbonate fraction of the Middle Devonian limestones from south-western Ontario, Canada (similar in age to the host rock of the Hüttenbläserschachthöhle). Thus, the carbonate fraction in such limestones has the potential to provide Pb with low isotope ratios to the stalagmites fed by their water solutions. This hypothesis is supported by the observed trace element variability in HBSH-1 (Figure 4.3). As discussed in Section 4.1, the phases between ~210.0 and ~204.9, ~201.5 and ~198.4 as well as ~195.9 and ~190.0 ka, correspond to relatively low infiltration rates, which could have depressed the transport of colloidal/particle materials, such as galena and clay minerals. However, relatively low recharge would favour the release of Pb from the carbonate fraction of the limestone host rock due to the longer water residence time in the karstic aquifer. Thus, we suggest that there could be a relatively constant low Pb supply (with low isotope ratios) from the carbonate fraction of the host rock, which was likely superimposed by Pb (with high isotope ratios) from the local galena minerals when the hydrological activity increased. It is also noted that peak values of $^{207}Pb/^{206}Pb$ and $^{208}Pb/^{206}Pb$ are observed during these periods (Figure 4.3), perhaps reflecting minor incorporation of galena minerals during weaker hydrological conditions. This interpretation must be confirmed by future studies of Pb isotope ratios of the limestone host rock and soil samples from the cave area.

## 4.5 Conclusions

In our study, LA-ICP-MS was used to investigate a set of trace elements and radiogenic lead isotopes in the bottom section of a stalagmite collected from north-western Germany. The chronology of this section was determined by the $^{230}Th/U$ method. The variations of Pb isotope ratios observed in HBSH-1 are in phase with the trace element concentrations. This indicates that all proxies may be influenced by the same mechanism. Since the Pb incorporated into the

stalagmite is mainly derived from external sources, such as the carbonate host rock and/or the soil cover above the cave, Pb isotopes have the potential to reflect the contribution of different sources of Pb. A mixture of two Pb components with distinct isotope ratios is assumed for HBSH-1. The end-member with high Pb isotope ratios for the Pb mixing in HBSH-1 may be mainly derived from the galena deposits in the cave area, while the component with low isotope ratios could be sourced from the carbonate fraction in the limestone host rock. However, this assumption needs to be clarified by future studies.

## Acknowledgements

Q.Y. thanks the Max Planck Graduate Center in Mainz, Germany, for financial support. D.S. thanks D.K. Richter, S. Niggemann and W. Grebe for providing stalagmite HBSH-1.

# Chapter 5

# Conclusion: Main findings and outlook

LA-ICP-MS is used to investigate trace element and isotopic characteristics in samples with different matrices, such as the BAM silicate reference glasses, ostracod shells (calcite with low-Mg) and aragonitic stalagmite. The spot analysis of LA-ICP-MS is proven to be a useful method for in-situ measurements of silicate glasses and carbonate samples. However, due to the extremely low thickness of ostracod shells, the line-scan method provides more precise results with a higher sample mass ablated per scan compared to spot analysis and is therefore more appropriate for single shell measurements.

The homogeneity of both BAM glasses with respect to major and trace elements was investigated in this study. The results suggested that all major (Si, Na, Ca, Mg, Al and K) and thirty-three trace elements are homogeneously distributed at the μm scale, except the elements Cs, Se, Cl, Ni, Mo, Cr, Hf, Pb, Fe and Zr, which may be inhomogeneously distributed. These results may support the application of BAM glasses as reference materials for bulk and microanalysis. Future studies are needed to focus on the discrepancies between the homogeneity results reported in the certificate and this work. With the exception of Sr, Ba, Ce and Pb, the concentrations of eighteen trace elements (As, Cd, Cl, Co, Cr, Cu, Fe, Mn, Mo, Ni, Sb, Se, Sn, S, Ti, V, Zn and Zr) show good agreement with the certified values, indicating the accuracy of the LA-ICP-MS data. Additionally, the abundances of P, Rb, Y, Nb, Cs, La, Pr, Nd, Sm, Eu, Gd, Tb, Dy, Ho, Er, Tm, Yb, Lu, Hf, Ta, Th and U were also determined, which may favour the use of BAM glasses as microanalytical reference glasses.

Based on the LA-ICP-MS measurements, no significant species-related difference in shell composition between the three ostracod taxa was observed in this study, although this conclusion needs to be clarified in future research. Mg/Ca and Sr/Ca ratios in ostracod calcite may be used as paleosalinity indicators in the Lake Nam Co. The interpretation for ostracod Ba, U and REEs is inconclusive here, mainly because of the unclear behaviour of these metals in the lake water and uncertainties regarding their distribution and uptake process in the ostracod shells. It is likely that the U and REEs abundances in ostracod shells are easily affected by inorganic (such as Fe-Mn oxides or carbonates) and

organic contaminants associated with the specimens after burial and diagenetic alternations. Therefore, more studies on shells from living ostracods from this area are necessary to evaluate the possible influence of post-depositional alternations on ostracod biomineralisation. If a certain correlation between Ba, U and REEs concentrations in ostracod calcite and those in host water could be established in the future, these metals may shed light on paleohydrological and paleohydrochemical reconstruction in aquatic environments.

A set of trace elements (Sr, Mg, Al, Si, Mn, Th, P and Pb) and radiogenic Pb isotopes were investigated in the bottom section of a stalagmite collected from north-western Germany. The chronology of this section was determined by the $^{230}$Th/U method. The variations of Pb isotope ratios observed in HBSH-1 are in phase with the trace element concentrations. This indicates that all proxies may be influenced with the same mechanism. Since the Pb incorporated into the stalagmite is mainly derived from external sources, such as the carbonate host rock and/or the soil cover above the cave, Pb isotopes have the potential to reflect the contribution of different sources of Pb. A mixture of two Pb components with distinct isotope ratios is assumed for HBSH-1. The end-member with high Pb isotope ratios for the Pb mixing in HBSH-1 may be mainly derived from the galena deposits in the cave area, while the component with low isotope ratios could be sourced from the carbonate fraction in the limestone host rock. However, this assumption needs to be clarified by future studies.

# List of Figures

# List of Tables

# Bibliography

An, Z., 2000. The history and variability of the East Asian paleomonsoon climate. Quaternary Science Reviews 19, 171–187.

Bajo, P., Drysdale, R., Woodhead, J., Hellstrom, J., Zanchetta, G., 2012. High-resolution U-Pb dating of an Early Pleistocene stalagmite from Corchia Cave (central Italy). Quaternary Geochronology 14, 5-17.

Baker, A., Proctor, C., Barnes, W.L., 2002. Stalagmite lamina doublets: a 1000 years proxy record of severe winters in northwest Scotland. International Journal of Climatology 22, 1339-1345.

Börner, N., De Baere, B., Yang, Q., Jochum, K.P., Frenzel, P., Andreae, M.O., Schwalb, A., 2013. Ostracod shell chemistry as proxy for paleoenvironmental change. Quaternary International 313-314, 17-37.

Borsato, A., Frisia, S., Fairchild, I.J., Somogyi, A., Susini, J., 2007. Trace element distribution in annual stalagmite laminae mapped by micrometer-resolution X-ray fluorescence: implications for incorporation of environmentally significant species. Geochimica et Cosmochimica Acta 71, 1494-1512.

Brigatti, M.F., Galan, E., Theng, B.K.G., 2006. Structures and mineralogy of clay minerals, in: Bergaya, F., Theng, B.K.G., Lagaly, G. (Ed.), Handbook of Clay Science, Developments in Clay Science. Elsevier, Amsterdam, pp. 19-86.

Brown, J.S., 1965. Oceanic lead isotopes and ore genesis. Economic Geology 60, 47-68.

Burchette, T.P., 1981. European Devonian reefs: a review of current concepts and models. The Society of Economic Paleontologists and Mineralogists (SEPM) Special Publication 30, 85-142.

Carignan, J., Libourel, G., Cloquet, C., Le Forestier, L., 2005. Lead isotopic composition of fly ash and flue gas residues from municipal solid waste combustors in France: implication for atmospheric lead source tracing. Environmental Science & Technology 39, 2018-2024.

Chivas, A.R., De Deckker, P., Shelley, J.M.G., 1983. Magnesium, strontium, and barium partitioning in nonmarine ostracode shells and their use in paleoenvironmental reconstructions – a preliminary study, in: Maddocks, R.F. (Ed.), Applications of Ostracoda. University of Houston, Geosciences Department, Houston, pp. 238-249.

Chivas, A.R., De Deckker, P., Shelley, J.M.G., 1985. Strontium content of ostracods indicates lacustrine palaeosalinity. Nature 316, 251-253.

Chivas, A.R., De Deckker, P., Shelley, J.M.G., 1986. Magnesium and strontium in non-marine ostracod shells as indicators of palaeosalinity and palaeotemperature. Hydrobiologia 143, 135-142.

Daut, G., Mäusbacher, R., Baade, J., Gleixner, G., Kroemer, E., Mügler, I., Wallner, J., Wang, J., Zhu, L., 2010. Late Quaternary hydrological changes inferred from lake level fluctuations of Nam Co (Tibetan Plateau, China). Quaternary International 218, 86-93.

De Baar, H.J.W., German, C.R., Elderfield, H., Van Gaans, P., 1988. Rare earth element distribution in anoxic waters of the Cariaco Trench. Geochimica et Cosmochimica Acta 52, 1203-1219.

De Deckker, P., Chivas, A.R., Shelley, J.M.G., 1999. Uptake of Mg and Sr in the euryhaline ostracod *Cyprideis* determined from in vitro experiments. Palaeogeography, Palaeoclimatology, Palaeoecology 148, 105-116.

Doberschütz, S., Frenzel, P., Haberzettl, T., Kasper, T., Wang, J., Zhu, L., Daut, G., Schwalb, A., Mäusbacher, R., 2013. Monsoonal forcing of Holocene paleoenvironmental change on the central Tibetan Plateau inferred using a sediment record from Lake Nam Co (Xizang, China). Journal of Paleolimnology. doi:10.1007/s10933-013-9702-1.

Dorale, J.A., Edwards, R.L., Calvin Alexander, J.E., Shen, C., Richards, D.A., Cheng, H., 2004. Uranium-series dating of speleothems: current techniques, limits, and applications, in: Sasowski, I.D., Mylroie, J. (Ed.), Studies of Cave Sediments. Kluwer Academic/Plenum Publishers, New York, pp. 177-197.

Eggins, S.M., Shelley, M.G., 2002. Compositional heterogeneity in NIST SRM 610-617 glasses. Geostandards Newsletter: The Journal of Geostandards and Geoanalysis, 26, 269-286.

Elderfield, H., Upstill-Goddard, R., Sholkovitz, E.R., 1990. The rare earth elements in rivers, estuaries, and coastal seas and their significance to the composition of ocean waters. Geochimica et Cosmochimica Acta 54, 971-991.

Engstrom, D.R., Nelson, S.R., 1991. Paleosalinity from trace metals in fossil ostracods compared with observational records at Devils Lake, North Dakota, USA. Palaeogeography, Palaeoclimatology, Palaeoecology 83, 295-312.

Erel, Y., Veron, A., Halicz, L., 1997. Tracing the transport of anthropogenic lead in the atmosphere and in soils using isotopic ratios. Geochimica et Cosmochimica Acta 61, 4495-4505.

Ettler, V., Mihaljevič, M., Komárek, M., 2004. ICP-MS measurements of lead isotopic ratios in soils heavily contaminated by lead smelting: tracing the sources of pollution. Analytical and Bioanalytical Chemistry 378, 311-317.

Fairchild, I.J., Smith, C.L., Baker, A., Fuller, L., Spötl, C., Mattey, D., McDermott, F., E.I.M.F., 2006. Modification and preservation of environmental signals. Earth-Science Reviews 75, 105-153.

Fairchild, I.J., Spötl, C., Frisia, S., Borsato, A., Susini, J., Wynn, P.M., Cauzid, J., E.I.M.F., 2010. Petrology and geochemistry of annually laminated stalagmites from an Alpine cave (Obir, Austria): seasonal cave physiology, in: Pedley, H.M.,

Rogerson, M. (Ed.), Tufas and Speleothems: Unravelling the Microbial and Physical Controls. Geological Society, London, Special Publication 336, 295–321.

Fairchild, I.J., Treble, P.C., 2009. Trace elements in speleothems as recorders of environmental changes. Quaternary Science Reviews 28, 449-468.

Feng, Z., An, C., Wang, H., 2006. Holocene climatic and environmental changes in the arid and semi-arid areas of China: a review. The Holocene 16, 1-12.

Firsching, F.H., Mohammadzadel, J., 1986. Solubility products of the rare-earth carbonates. Journal of Chemical & Engineering Data 31, 40-42.

Frenzel, P., Wrozyna, C., Xie, M., Zhu, L., Schwalb, A., 2010. Palaeo-water depth estimation for a 600-year record from Nam Co (Tibet) using an ostracod-based transfer function. Quaternary International 218, 157-165.

Frisia, S., Borsato, A., Fairchild, I.J., McDermott, F., Selmo, E.M., 2002. Aragonite-calcite relationship in speleothems (Grotte de Clamouse, France): environment, fabrics and carbonate geochemistry. Journal of Sedimentary Research 72, 687-699.

Gabitov, R.I., Gaetani, G.A., Watson, E.B., Cohen, A.L., Ehrlich, H.L., 2008. Experimental determination of growth rate effect on $U^{6+}$ and $Mg^{2+}$ partitioning between aragonite and fluid at elevated $U^{6+}$ concentration. Geochimica et Cosmochimica Acta 72, 4058-4068.

Gaetani, G.A., Cohen, A.L., 2006. Element partitioning during precipitation of aragonite from seawater: a framework for understanding paleoproxies. Geochimica et Cosmochimica Acta 70, 4617-4634.

Gao, Y.X., 1985. Tibetan soil. Science, Beijing, pp 2-15 (in Chinese).

Gasse, F., Arnold, M., Fontes, J.C., Fort, M., Gibert, E., Huc, A., Li, B., Li, Y., Liu, Q., Melieres, F., Van Campo, E., Wang, F., Zhang, Q., 1991. A 13,000-year climate record from Western Tibet. Nature 353, 742–745.

Gasse, F., Fontes, J.C., Van Campo, E., Wei, K., 1996. Holocene environmental changes in Bangong Co basin (western Tibet). Part 4: discussion and conclusions. Palaeogeography, Palaeoclimatology, Palaeoecology 120, 79-92.

Genty, D., Blamart, D., Ouahdi, R., Gilmour, M., Baker, A., Jouzel, J., Van-Exer, S., 2003. Precise dating of Dansgaard-Oeschger climate oscillation in western Europe from stalagmite data. Nature 421, 833-838.

Giesler, R., Adersson, T., Lövgren, L., Persson, P., 2005. Phosphate sorption in aluminum- and iron-rich humus soils. Soil Science Society of America Journal 69, 77-86.

Gillikin, D.P., Dehairs, F., Lorrain, A., Steenmans, D., Baeyens, W., André, L., 2006. Barium uptake into the shells of the common mussel (*Mytilus edulis*) and the potential for estuarine paleo-chemistry reconstruction. Geochimica et Cosmochimica Acta 70, 395-407.

Goede, A., McCulloch, M., McDermott, F., Hawkesworth, C., 1998. Aeolian contribution to strontium and strontium isotope variations in a Tasmanian speleothem. Chemical Geology 149, 37-50.

Grebe, W., 1994. Die Hüttenbläserschachthöhle – eine neuentdeckte Höhle in Iserlohn-Letmathe. Mitteilungen & Berichte. Speläogruppe Letmathe 10 (1-4), 49-65.

Grebe, W., 2007. Die Feuersteinkugel aus dem Hüttenbläser. Speläologisches Jahrbuch 22-23, 61-64.

Griffiths, H., Holmes, J.A., 2000. Non-marine ostracods & Quaternary palaeoenvironments. Quaternary Research Association, Technical Guide no. 8, London.

Gu, Z., Liu, J., Yuan, B., Liu, D., Liu, R., Liu, Y., Yaskawa, K., 1993. Monsoon variations of the Qinghai-Xizang Plateau during the Last 12,000 years—geochemical evidence from the sediments in the Siling Lake. Chinese Science Bulletin 38, 577–581.

Guillong, M., Hametner, K., Reusser, E., Wilson, S.A., Günther, D., 2005. Preliminary characterisation of new glass reference materials (GSA-1G, GSC-1G, GSD-1G and GSE-1G) by laser ablation-inductively coupled plasma-mass spectrometry using 193 nm, 213 nm and 266 nm wavelengths. Geostandards and Geoanalytical Research, 29, 315–331.

GUM, 1995. Guide to the Expression of Uncertainty in Measurement. International Organisation for Standardization (Geneva, Switzerland), ISBN 92-67-10188-9.

Günther, F., Mügler, I., Mäusbacher, R., Daut, G., Leopold, K., Gerstmann, U.C., Xu, B., Yao, T., Gleixner, G., 2011. Response of δD values of sedimentary n-alkanes to variations in source water isotope signals and climate proxies at lake Nam Co, Tibetan Plateau. Quaternary International 236, 82-90.

Haack, U.H., Heinrichs, H., Gutsche, F.H., Plessow, K., 2003. The isotopic composition of anthropogenic Pb in soil profiles of Northern Germany: evidence for pollutant Pb from a continent-wide mixing system. Water, Air, & Soil Pollution 150, 113-134.

Haley, B.A., Klinkhammer, G.P., McManus, J., 2004. Rare earth elements in pore waters of marine sediments. Geochimica et Cosmochimica Acta 68 (6), 1265-1279.

Haley, B.A., Klinkhammer, G.P., Mix, A.C., 2005. Revisiting the rare earth elements in foraminiferal tests. Earth and Planetary Science Letters 239, 79-97.

Hansmann, W., Köppel, V., 2000. Lead isotopes as tracers of pollutants in soils. Chemical Geology 171, 123-144.

Haskin, B.A., Haskin, M.A., Frey, F.A., Wildeman, T.R., 1968. Relative and absolute terrestrial abundances of the rare earth elements, in: Ahrens, L.H. (Ed.), Origin and Distribution of the Elements. Pergamon Press, Oxford, pp. 889-912.

Havach, S.M., Chandler, G.T., Wilson-Finelli, A., Shaw, T.J., 2001. Experimental determination of trace element partition coefficients in cultured benthic foraminifera. Geochimica et Cosmochimica Acta 65 (8), 1277-1283.

Henderson, G.M., 2006. Caving in to new chronologies. Science 313, 620-622.

Herzschuh, U., Winter, K., Wünnemann, B., Li, S., 2006. A general cooling trend on the central Tibetan Plateau throughout the Holocene recorded by the Lake Zigetang pollen spectra. Quaternary International 154-155, 113-121.

Hoffmann, D.L., 2008. $^{230}$Th isotope measurements of femtogram quantities for U-series dating using multi ion counting (MIC) MC-ICPMS. International Journal of Mass Spectrometry 275, 75-79.

Hoffmann, D.L., Prytulak, J., Richards, D.A., Elliott, T., Coath, C.D., Smart, P.L., Scholz, D., 2007. Procedures for accurate U and Th isotope measurements by high precision MC-ICP-MS. International Journal of Mass Spectrometry 264, 97-109.

Holmes, J.A., 1996. Trace-element and stable-isotope geochemistry of non-marine ostracod shells in Quaternary palaeoenvironmental reconstruction. Journal of Paleolimnology 15, 223-235.

Holmes, J.A., Allen, M.J., Street-Perrott, F.A., Ivanovich, M., Perrott, R.A., Waller, M.P., 1999. Late Holocene palaeolimnology of Bal Lake, Northern Nigeria, a multidisciplinary study. Palaeogeography, Palaeoclimatology, Palaeoecology 148, 169-185.

Holmes, J.A., Street-Perrott, F.A., Allen, M.J., Fothergill, P.A., Harkness, D.D., Kroon, D., Perrott, R.A., 1997. Holocene palaeolimnology of Kajemarum Oasis, Northern Nigeria: an isotopic study of ostracodes, bulk carbonate and organic carbon. Journal of the Geological Society 154, 311-319.

Hu, M.Y., Fan, X.T., Stoll, B., Kuzmin, D., Liu, Y., Liu, Y.S., Sun, W.D., Wang, G., Zhan, X.C., Jochum, K.P., 2011. Preliminary Characterisation of New Reference Materials for Microanalysis: Chinese Geological Standard Glasses CGSG-1, CGSG-2, CGSG-4 and CGSG-5. Geostandards and Geoanalytical Research, 35, 235-251.

Huang, B., Yang, L., Fan, Y., 1985. Ostracodes from surface deposits of Recent lakes in Xizang. Acta Micropalaeontologica Sinica 2, 369-376 (in Chinese with English abstract).

Huang, H., Fairchild, I.J., Borsato, A., Frisia, S., Cassidy, N.J., McDermott, F., Hawkesworth, C.J., 2001. Seasonal variation in Sr, Mg and P in modern speleothems (Grotta di Ernesto, Italy). Chemical Geology 175, 429-448.

Huang, Y., Fairchild, I.J., 2001. Partitioning of $Sr^{2+}$ and $Mg^{2+}$ into calcite under karst-analogue experimental conditions. Geochimica et Cosmochimica Acta 65, 47-62.

ISO Guide 35, 1989. Certification of reference materials: General and statistical principles. International Organisation for Standardization (Geneva, Switzerland), 32pp.

Ito, E., De Deckker, P., Eggins, S.M., 2003. Ostracodes and their shell chemistry: implications for paleohydrologic and paleoclimatologic applications. Paleontological Society Papers 9, 119-144.

Ito, E., Forester, R.M., 2009. Changes in continental ostracode shell chemistry; uncertainty of cause. Hydrobiologia 620, 1-15.

Jarosewich, E., 2002. Smithsonian microbeam standards. Journal of Research of the National Institute of Standards and Technology, 107, 681–685.

Jiao, K., Iwata, S., Yao, T., Jing, Z., Li, Z., 2005. Variation of Zepu Glacier and environmental change in the eastern Nyaiqêntanglha range since 3.2 ka BP. Journal of Glaciology and Geocryology 27, 74-79 (in Chinese with English abstract).

Jochum, K.P., Scholz, D., Stoll, B., Weis, U., Wilson, S.A., Yang, Q., Schwalb, A., Börner, N., Jacob, D.E., Andreae, M.O., 2012. Accurate trace element analysis of speleothems and biogenic calcium carbonates by LA-ICP-MS. Chemical Geology 318-319, 31-44.

Jochum, K.P., Stoll, B., 2008. Reference materials for elemental and isotopic analyses by LA- (MC)-ICP-MS: Successes and outstanding needs. In: Sylvester P. (ed.), Laser ablation ICP-MS in the Earth Sciences: Current practices and outstanding issues. Mineralogical Association of Canada, Short Course Series. Min. Ass. Canada, Quebec, Canada, 40, 147–168.

Jochum, K.P., Stoll, B., Friedrich, J.M., Amini, M., Becker, St., Dücking, M., Ebel, D.S., Enzweiler, J., Hu, M.Y., Kuzmin, D., Mertz-Kraus, R., Müller, W.E.G., Regnery, J., Sobolev, A., Wang, X.H., Zhan, X.C., 2009. Laser Ablation-Inductively Coupled Plasma-Mass Spectrometry and its application in geochemistry, cosmochemistry and environmental research. Rock and Mineral Analysis, 28, 53-68.

Jochum, K.P., Stoll, B., Herwig, K., Willbold, M., 2006a. Improvement of in situ Pb isotope analysis by LA-ICP-MS using a 193 nm Nd:YAG laser. Journal of Analytical Atomic Spectrometry 21, 666-675.

Jochum, K.P., Stoll, B., Herwig, K., Willbold, M., 2007. Validation of LA-ICP-MS trace element analysis of geological glasses using a new solid-state 193 nm Nd:YAG laser and matrix-matched calibration. Journal of Analytical Atomic Spectrometry 22, 112-121.

Jochum, K.P., Stoll, B., Herwig, K., Willbold, M., Hofmann, A.W., Amini, M., Aarburg, S., Abouchami, W., Hellebrand, E., Mocek, B., Raczek, I., Stracke, A., Alard, O., Bouman, C., Becker, St., Dücking, M., Brätz, H., Klemd, R., de Bruin, D., Canil, D., Cornell, D., de Hoog, J.C.M., Dalpé, C., Danyushevsky, L.V., Eisenhauer, A., Gao, Y., Snow, J.E., Groschopf, N., Günther, D., Latkoczy, C., Guillong, M., Hauri, E., Höfer, H.E., Lahaye, Y., Horz, K., Jacob, D.E., Kasemann, S., Kent, A.J.R., Zack, T., Ludwig, T., Mason, P.R.D., Meixner, A., Rosner, M., Misawa, K., Nash, B.P., Pfänder, J.A., Premo, W.R., Sun, W.D., Tiepolo, M., Vannucci, R., Vennemann, T., Wayne, D., Woodhead, J.D., 2006b. MPI-DING reference glasses for in situ microanalysis: New reference values for element concentrations and isotope ratios. Geochemistry Geophysics Geosystems, 7, Q02008, doi: 10.1029/2005GC001060.

Jochum, K.P., Stoll, B., Weis, U., Jacob, D.E., Mertz-Kraus, R., Andreae, M.O., 2014. Non-matrix matched calibration for the multi-element analysis of geological and environmental samples using 200 nm femtosecond LA-ICP-MS: a comparison with nanosecond lasers. Geostandards and Geoanalytical Research http://dx.doi.org/ 10.1111/j.1751-908X.2014.12028.x

Jochum, K.P., Weis, U., Stoll, B., Kuzmin, D., Yang, Q., Raczek, I., Jacob, D.E., Stracke, A., Birbaum, K., Frick, D.A., Günther, D., Enzweiler, J., 2011a. Determination of reference values for NIST SRM 610-617 glasses following ISO guidelines. Geostandards and Geoanalytical Research 35, 397-429.

Jochum K.P., Willbold M., Raczek I., Stoll B., Herwig K., 2005. Chemical characterisation of the USGS reference glasses GSA-1G, GSC-1G, GSD-1G, GSE-1G, BCR-2G, BHVO-2G and BIR-1G using EPMA, ID-TIMS, ID-ICP-MS and LA-ICP-MS. Geostandards and Geoanalytical Research, 29, 285–302.

Jochum, K.P., Wilson, S.A., Abouchami, W., Amini, M., Chmeleff, J., Eisenhauer, A., Hegner, E., Iaccheri, L.M., Kieffer, B., Krause, J., McDonough, W.F., Mertz-Kraus, R., Raczek, I., Rudnick, R.L., Scholz, D., Steinhoefel, G., Stoll, B., Stracke, A., Tonarini, S., Weis, D., Weis, U., Woodhead, J.D., 2011b. GSD-1G and MPI-DING reference glasses for in situ and bulk isotopic determination. Geostandards and Geoanalytical Research 35, 193-226.

Johannesson, K.H., Lyons, W.B., 1994. The rare earth element geochemistry of Mono Lake water and the importance of carbonate complexing. Limnology and Oceanography 39, 1141-1154.

Johannesson, K.H., Lyons, W.B., Stetzenbach, K.J., Byrne, R.H., 1995. The solubility control of rare earth elements in natural terrestrial waters and the significance of $PO_4^{3-}$ and $CO_3^{2-}$ in limiting dissolved rare earth concentrations: a review of recent information. Aquatic Geochemistry 1, 157-173.

Kane, J.S., 2002. Fitness-for-purpose of reference material reference values in relation to traceability of measurement, as illustrated by USGS BCR-1, NIST SRM 610 and IAEA NBS 28. Geostandards Newsletter: The Journal of Geostandards and Geoanalysis, 26, 7–29.

Kane, J.S., Potts, P.J., Wiedenbeck, M., Carignan, J., Wilson, S., 2003. International Association of Geoanalysts' protocol for the certification of geological and environmental reference materials. Geostandards Newsletter: The Journal of Geostandards and Geoanalysis, 27, 227–244.

Kapp, J.L.D., Harrison, T.M., Kapp, P., Grove, M., Lovera, O.M., Lin, D., 2005. Nyainqentanglha Shan: a window into the tectonic, thermal, and geochemical evolution of the Lhasa block, southern Tibet. Journal of Geophysical Research-Part B-Solid Earth 110 (88), 24.

Kasper, T., Frenzel, P., Haberzettl, T., Schwarz, A., Daut, G., Meschner, S., Wang, J., Zhu, L., Mäusbacher, R., 2013. Interplay between redox conditions and hydrological changes in sediments from Lake Nam Co (Tibetan Plateau) during the past 4000 cal BP inferred from geochemical and micropaleontological analyses. Palaeogeography, Palaeoclimatology, Palaeoecology 392, 261-271.

Kasper, T., Haberzettl, T., Doberschütz, S., Daut, G., Wang, J., Zhu, L., Nowaczyk, N., Mäusbacher, R., 2012. Indian Ocean Summer Monsoon (IOSM)-dynamics within the past 4 ka recorded in the sediments of Lake Nam Co, central Tibetan Plateau (China). Quaternary Science Reviews 39, 73-85.

Keil, A., Berking, J., Mügler, I., Schütt, B., Schwalb, A., Steeb, P., 2010. Hydrological and geomorphological basin and catchment characteristics of Lake Nam Co, south-central Tibet. Quaternary International 218, 118-130.

Klinkhammer, G.P., Palmer, M.R., 1991. Uranium in the oceans: Where it goes and why. Geochimica et Cosmochimica Acta 55, 1799-1806.

Komárek, M., Ettler, V., Chrastný, V., Mihaljevič, M., 2008. Lead isotopes in environmental sciences: a review. Environment International 34, 562-577.

Krahn, L., Baumann, A., 1996. Lead isotope systematics of epigenetic lead-zinc mineralization in the western part of the Rheinisches Schiefergebirge, Germany. Mineralium Deposita 31, 225-237.

Kramer, A., Herzschuh, U., Mischke, S., Zhang, C., 2010a. Late Quaternary environmental history of the south-eastern Tibetan Plateau inferred from the Lake Naleng non-pollen palynomorph record. Veget Hist Archaeobot 19, 453-468.

Kramer, A., Herzschuh, U., Mischke, S., Zhang, C., 2010b. Holocene treeline shifts and monsoon variability in the Hengduan Mountains (southern Tibetan Plateau), implications from palynological investigations. Palaeogeography, Palaeoclimatology, Palaeoecology 286, 23-41.

Ku, T.L., Knauss, K.G., Mathieu, G.G., 1977. Uranium in the open ocean: concentration and isotopic composition. Deep Sea Research 24, 1005-1007.

Langmuir, D., 1978. Uranium solution-mineral equilibria at low temperatures with applications to sedimentary ore deposits. Geochimica et Cosmochimica Acta 42, 547-569.

Large, D., Schaeffer, R., Höhndorf, A., 1983. Lead isotope data from selected galena occurrences in the north Eifel and north Sauerland, Germany. Mineralium Deposita 18, 235-243.

Lea, D.W., Boyle, E.A., 1989. Barium content of benthic foraminifera controlled by bottom-water composition. Nature 338, 751-753.

Lea, D.W., Spero, H.J., 1994. Assessing the reliability of paleochemical tracers: barium uptake in the shells of planktonic foraminifera. Paleoceanograhy 9 (3), 445-452.

Li, C., Kang, S., Wang, X., Ajmone-Marsan, F., Zhang, Q., 2008a. Heavy metals and rare earth elements (REEs) in soil from the Nam Co basin, Tibetan Plateau. Environmental Geology 53, 1433-1440.

Li, C., Kang, S., Zhang, Q., Kaspari, S., 2007. Major ionic composition of precipitation in the Nam Co basin, Central Tibetan Plateau. Atmospheric Research 85, 351-360.

Li, M., Kang, S., Zhu, L., You, Q., Zhang, Q., Wang, J., 2008b. Mineralogy and geochemistry of the Holocene lacustrine sediments in Nam Co, Tibet. Quaternary International 187, 105-116.

Li, M., Zhu, L., Wang, J., Wang, L., Yi, C., Galy, A., 2011. Multiple implications of rare earth elements for Holocene environmental changes in Nam Co, Tibet. Quaternary International 236, 96-106.

Lister, G.S., Kelts, K., Zao, C., Yu, J., Niessen, F., 1991. Lake Qinghai, China: closed-basin lake levels and the oxygen isotope record for ostracoda since the latest Pleistocene. Palaeogeography, Palaeoclimatology, Palaeoecology 84, 141-162.

Liu, X., Kang, S., Liu, Y., Han, W., 2008. Microbial community structures in the Nam Co Lake, Tibetan Plateau, and comparison with other alpine lakes. Journal of Glaciology and Geocryology 30 (6), 1041-1047 (in Chinese with English abstract).

Long, L., 1999. Lead isotopes, in: Marshall, C.P., Fairbridge, R.W. (Ed.), Encyclopedia of Geochemistry. Kluwer Academic Publishers.

Matschat, R., Dette, A., Guadagnino, E., 2005. The certification of the Mass Fraction of Arsenic (III) oxide, Barium oxide, Cadmium oxide, Cerium (IV) oxide, Chloride, Cobalt oxide, Chromium (III) oxide, Copper (II) oxide, Iron (III) oxide, Manganese (II) oxide, Molybdenum (VI) oxide, Nickel (II) oxide, Lead (II) oxide, Antimony (III) oxide, Selenium, Tin (IV) oxide, Sulfur trioxide, Strontium oxide, Titanium (IV) oxide, Vanadium (V) oxide, Zinc oxide, and Zirconium (IV) oxide in Soda Lime Glass BAM-S005-A and BAM-S005-B. http://www.rm-certificates.bam.de/en/certificates/special_materials/.

McDermott, F., 2004. Palaeo-climate reconstruction from stable isotope variations in speleothems: a review. Quaternary Science Reviews 23, 901-918.

McMillan, E.A., Fairchild, I.J., Frisia, S., Borsato, A., McDermott, F., 2005. Annual trace element cycles in calcite-aragonite speleothems: evidence of drought in the western Mediterranean 1200-1100 yr BP. Journal of Quaternary Science 20 (5), 423-433.

Millero, F.J., 1992. Stability constants for the formation of rare earth inorganic complexes as a function of ionic strength. Geochimica et Cosmochimica Acta 56, 3123-3132.

Mischke, S., Herzschuh, U., Massmann, G., Zhang, C., 2007. An ostracod-conductivity transfer function for Tibetan lakes. Journal of Paleolimnology 38, 509-524.

Mischke, S., Kramer, M., Zhang, C., Shang, H., Herzschuh, U., Erzinger, J., 2008. Reduced early Holocene moisture availability in the Bayan Har Mountains,

northeastern Tibetan Plateau, inferred from a multi-proxy lake record. Palaeogeography, Palaeoclimatology, Palaeoecology 267, 59-76.

Mischke, S., Zhang, C., Börner, A., Herzschuh, U., 2010. Lateglacial and Holocene variation in aeolian sediment flux over the northeastern Tibetan Plateau recorded by laminated sediments of a saline meromictic lake. Journal of Quaternary Science 25 (2), 162-177.

Monna, F., Hamer, K., Lévêque, J., Sauer, M., 2000. Pb isotopes as a reliable marker of early mining and smelting in the Northern Harz province (Lower Saxony, Germany). Journal of Geochemical Exploration 68, 201-210.

Monna, F., Lancelot, J., Croudace, I.W., Cundy, A.B., Lewis, J.T., 1997. Lead isotopic composition of airborne material from France and the Southern U.K. implications for Pb pollution sources in urban areas. Environmental Science & Technology 31, 2277-2286.

Mügler, I., Gleixner, G., Günther, R., Mäusbacher, R., Daut, G., Schütt, B., Berking, J., Schwalb, A., Schwark, L., Xu, B., Zao, T., Zhu, L., Yi, C., 2010. A multi-proxy approach to reconstruct hydrological changes and Holocene climate development of Nam Co, central Tibet. Journal of Paleolimnology 43, 625-648.

NBS, 1970. Certificate of analysis: Trace elements in glass SRMs: SRM 610 through 619, inclusive. National Bureau of Standards (Gaitherburg, USA), 4pp.

Niggemann, S., Mangini, A., Richter, D.K., Wurth, G., 2003. A paleoclimate record of the last 17,600 years in stalagmites from the B7 cave, Sauerland, Germany. Quaternary Science Reviews 22, 555-567.

Palmer, M.R., 1985. Rare earth elements in foraminifera tests. Earth and Planetary Science Letters 73, 285-298.

Richards, D., Bottrell, S.H., Cliff, R.A., Ströhle, K., Rowe, P.J., 1998. U-Pb dating of a speleothem of Quaternary age. Geochimica et Cosmochimica Acta 62, 3683-3688.

Richter, D.K., Götte, T., Niggemann, S., Wurth, G., 2004. $REE^{3+}$ and $Mn^{2+}$ activated cathodoluminescence in lateglacial and Holocene stalagmites of central Europe: evidence for climatic processes? Holocene 14, 759-767.

Ricketts, R.D., Johnson, T.C., Brown, E.T., Rasmussen, K.A., Romanovsky, V.V., 2001. The Holocene paleolimnology of Lake Issyk-Kul, Kyrgyzstan: trace element and stable isotope composition of ostracodes. Palaeogeography, Palaeoclimatology, Palaeoecology 176, 207-227.

Roberts, N.L., Piotrowski, A.M., Elderfield, H., Eglinton, T.I., Lomas, M.W., 2012. Rare earth element association with foraminifera. Geochimica et Cosmochimica Acta 94, 57-71.

Rocholl, A.B.E., Simon, K., Jochum, K.P., Bruhn, F., Gehann, R., Kramar, U., Luecke, W., Molzahn, M., Pernicka, E., Seufert, M., Spettel, B., Stummeier, J., 1997. Chemical characterisation of NIST silicate glass reference material SRM 610 by ICP-MS, TIMS, LIMS, SSMS, INAA, AAS and PIXE. Geostandards Newsletter: The Journal of Geostandards and Geoanalysis, 21, 101-114.

Russell, A.D., Emerson, S., Nelson, B.K., Erez, J., Lea, D.W., 1994. Uranium in foraminiferal calcite as a recorder of seawater uranium concentrations. Geochimica et Cosmochimica Acta 58, 671-681.

Russell, A.D., Hönisch, B., Spero, H.J., Lea, D.W., 2004. Effects of seawater carbonate ion concentration and temperature on shell U, Mg, and Sr in cultured planktonic foraminifera. Geochimica et Cosmochimica Acta 68, 4347-4361.

Scholz, D., Hoffmann, D.L., 2008. $^{230}$Th/U-dating of fossil corals and speleothems. Journal of Quaternary Science (Eiszeitalter und Gegenwart) 57, 52-77.

Scholz, D., Hoffmann, D.L., 2011. StalAge – an algorithm designed for construction of speleothem age models. Quaternary Geochronology 6, 369-382.

Scholz, D., Hoffmann, D.L., Spötl, C., Hopcroft, P., Mangini, A., Richter, D.K., 2011. Decoupled evolution of temperature and precipitation in Western Germany during the Last Interglacial reconstructed from a precisely dated speleothem. Mineralogical Magazine 75, 1823.

Schwalb, A., 2003. Lacustrine ostracodes as stable isotope recorders of late-glacial and Holocene environmental dynamics and climate. Journal of Paleolimnology 29 (3), 265-351.

Shen, J., Liu, X., Wang, S., Matsumoto, R., 2005. Palaeoclimatic changes in the Qinghai Lake area during the last 18,000 years. Quaternary International 136, 131-140.

Smith, P.E., Farquhar, R.M., Hancock, R.G., 1991. Direct radiometric age determination of carbonate diagenesis using U-Pb in secondary calcite. Earth and Planetary Science Letters 105, 474-491.

Smith, R.M., Martell, A.E., 1976. Critical Stability Constants, Volume 4, Inorganic Complexes, Plenum Press, New York.

Spötl, C., Scholz, D., Mangini, A., 2008. A terrestrial U/Th-dated stable isotope record of the Penultimate Interglacial. Earth and Planetary Science Letters 276, 283-292.

Stückrad, S., Sable, K.J., Wilcke, W., 2008. Periglacial transport distance of Pb derived from small-scale ore veins in the Rhenish Slate Mountains. Geoderma 148, 232-239.

Tesoriero, A.J., Pankow, J.F., 1996. Solid solution partitioning of $Sr^{2+}$, $Ba^{2+}$, and $Cd^{2+}$ to calcite. Geochimica et Cosmochimica Acta 60, 1053-1063.

Teutsch, N., Erel, Y., Halicz, L., Banin, A., 2001. Distribution of natural and anthropogenic lead in Mediterranean soils. Geochimica et Cosmochimica Acta 65, 2853-2864.

Treble, P., Shelley, J.M.G., Chappell, J., 2003. Comparison of high-resolution subannual records of trace elements in a modern (1911-1992) speleothems with instrumental climate data from southwest Australia. Earth and Planetary Science Letters 216, 141-153.

Van Campo, E., Gasse, F., 1993. Pollen- and diatom-inferred climatic and hydrological changes in Sumxi Co basin (western Tibet) since 13,000 yr B.P.. Quaternary Research 39, 300-313.

Van der Meeren, T., Ito, E., Verschuren, D., Almendinger, J.E., Martens, K., 2011. Valve chemistry of *Limnocythere inopinata* (Ostracoda) in a cold arid environment – Implications for paleolimnological interpretation. Palaeogeography, Palaeoclimatology, Palaeoecology 306, 116-126.

Von Kamp, H., 1972. Geologische Karte von Nordrhein-Westfallen 1:25.000. Erläuterung zu Blatt 461 Hohenlimburg. 2 völlig neu bearbeitete Auflage, Krefeld, 182 S.

Wang, J., Zhu, L., 2006. Preliminary study on the field investigation of Nam Co. Annual report of Nam Co monitoring and research station for multisphere interactions. ITPRCAS, Beijing, p. 42.

Wang, Y., Cheng, H., Edwards, R.L., Kong, X., Shao, X., Chen, S., Wu, J., Jiang, X., Wang, X., An, Z., 2008. Millennial- and orbital-scale changes in the east Asian monsoon over the past 224,000 years. Nature 451, 1090-1093.

Wansard, G., De Deckker, P., Julià, R., 1998. Variability in ostracod partition coefficients D(Sr) and D(Mg) - Implications for lacustrine palaeoenvironmental reconstructions. Chemical Geology 146, 39-54.

Wassenburg, J.A., Immenhauser, A., Richter, D.K., Jochum, K.P., Fietzke, J., Deininger, M., Goos, M., Scholz, D., Sabaoui, A., 2012. Climate and cave control on Pleistocene/Holocene calcite-to-aragonite transitions in speleothems from Morocco: Elemental and isotopic evidence. Geochimica et Cosmochimica Acta 92, 23-47.

Wassenburg, J.A., Immenhauser, A., Richter, D.K., Niedermayr, A., Riechelmann, S., Fietzke, J., Scholz, D., Jochum, K.P., Fohlmeister, J., Schröder-Ritzrau, A., Sabaoui, A., Riechelmann, D.F.C., Schneider, L., Esper, J., 2013. Moroccan speleothem and tree ring records suggest a variable positive state of the North Atlantic Oscillation during the Medieval Warm Period. Earth and Planetary Science Letters 375, 291-302.

Wedepohl, K.H., Delevaux, M.H., Doe, B.R., 1978. The potential source of lead in the Permian Kupferschiefer bed of Europe and some selected Paleozoic mineral deposits in the Federal Republic of Germany. Contributions to Mineralogy and Petrology 65, 273-281.

Wrozyna, C., Frenzel, P., Daut, G., Mäusbacher, R., Zhu, L., Schwalb, A., 2012. Holocene lake-level changes of Lake Nam Co, Tibetan Plateau, deduced from ostracod assemblages and $\delta^{18}O$ and $\delta^{13}C$ signatures of their valves. Developments in Quaternary Sciences 17, 281-295.

Wrozyna, C., Frenzel, P., Steeb, P., Zhu, L., Gelden, R., Mackensen, A., Schwalb, A., 2010. Stable isotope and ostracode species assemblage evidence for lake level changes of Nam Co, southern Tibet, during the past 600 years. Quaternary International 212, 2-13.

Wrozyna, C., Frenzel, P., Steeb, P., Zhu, L., Schwalb, A., 2009a. Recent lacustrine ostracoda and a first transfer function for palaeo-water depth estimation in Nam Co, southern Tibetan Plateau. Revista Española de Micropaleontología 41 (1-2), 1-20.

Wrozyna, C., Frenzel, P., Xie, M., Zhu, L., Schwalb, A., 2009b. A taxonomical and ecological overview of recent and Holocene ostracodes of the Nam Co region, southern Tibet. Quaternary Sciences 29 (4), 665-677.

Wu, Y., Lücke, A., Jin, Z., Wang, S., Schleser, G.H., Battarbee, R.W., Xia, W., 2006. Holocene climate development on the central Tibetan Plateau: a sedimentary record from Cuoe Lake. Palaeogeography, Palaeoclimatology, Palaeoecology 234, 328–340.

Wynn, P.M., Fairchild, I.J., Baker, A., Baldini, J.U.L., McDermott, F., 2008. Isotopic archives of sulfate in speleothems. Geochimica et Cosmochimica Acta 72, 2465-2477.

Xia, J., Engstrom, D.R., Ito, E., 1997a. Geochemistry of ostracode calcite: Part 2. The effects of water chemistry and seasonal temperature variation on *Candona rawsoni*. Geochimica et Cosmochimica Acta 61 (2), 383-391.

Xia, J., Haskell, B.J., Engstrom, D.R., Ito, E., 1997b. Holocene climate reconstructions from tandem trace-element and stable-isotope composition of ostracodes from Coldwater Lake, north Dakota, USA. Journal of Paleolimnology 17, 85-100.

Xie, M., Zhu, L., Peng, P., Wang, J., Wang, Y., Schwalb, A., 2009. Ostracod assemblages and their environmental significance from the lake core of the Nam Co on the Tibetan Plateau 8.4 ka BP. Journal of Geographical Sciences 19, 387-402.

You, Q., Kang, S., Li, C., Li, M., Liu, J., 2006. Features of meteorological parameters at Nam Co station, Tibetan Plateau. Annual report of Nam Co Monitoring and Research Station for multisphere interactions 1, 1-8 (in Chinese with English abstract).

Yuan, J., Gao, J., Lu, X., Chen, K., 2002. Assessment on wetland resources in Nam Co and countermeasures for conservation and rational use. Resources Science 24 (4), 29-36 (in Chinese with English abstract).

Žák, K., Richter, D.K., Filippi, M., Živor, R., Deininger, M., Mangini, A., Scholz, D., 2012. Coarsely crystalline cryogenic cave carbonate – a new archive to estimate the Last Glacial minimum permafrost depth in Central Europe. Climate of the Past 8, 1821–1837.

Zhang, L., Sun, Z., An, Z., Liu, W., Li, X., 2006a. A preliminary analysis on Ostracoda of different water bodies from Qinghai Lake area, NW China. Acta Micropalaeontologica Sinica 23 (4), 425-436 (in Chinese with English abstract).

Zhang, Q., Kang, S., Wang, F., Li, C., Xu, Y., 2006b. Major ion chemistry in the Nam Co Basin, Tibetan Plateau. Annual Report of Nam Co Monitoring and Research Station for Multisphere Interactions 1, 86-96.

Zhong, S., Mucci, A., 1989. Calcite and aragonite precipitation from seawater solutions of various salinities: precipitation rates and overgrowth compositions. Chemical Geology 78, 283-299.

Zhou, H., Chi, B., Lawrence, M., Zhao, J., Yan, J., Greig, A., Feng, Y., 2008. High-resolution and precisely dated record of weathering and hydrological dynamics recorded by manganese and rare-earth elements in a stalagmite from Central China. Quaternary Research 69, 438-446.

Zhou, J., Lundstrom, C.C., Fouke, B., Panno, S., Hackley, K., Curry, B., 2005. Geochemistry of speleothem records from southern Illinois: development of ($^{234}$U)/($^{238}$U) as a proxy for paleoprecipitation. Chemical Geology 221, 1-20.

Zhu, D., Meng, X., 2004. On the Quaternary Environmental Evolution of the Nam Co Area, Tibet. Geology Press, Beijing, pp. 1-93 (in Chinese with English abstract).

Zhu, L., Peng, P., Xie, M., Wang, J., Frenzel, P., Wrozyna, C., Schwalb, A., 2010a. Ostracod-based environmental reconstruction over the last 8,400 years of Nam Co Lake on the Tibetan plateau. Hydrobiologia 648, 157-174.

Zhu, L., Wu, Y., Wang, J., Lin, X., Ju, J., Xie, M., Li, M., Mäusbacher, R., Schwalb, A., Daut, G., 2008. Environmental changes since 8.4 ka reflected in the lacustrine core sediments from Nam Co, central Tibetan Plateau, China. The Holocene 18 (5), 831-839.

Zhu, L., Xie, M., Wu, Y., 2010b. Quantitative analysis of lake area variations and the influence factors from 1971 to 2004 in the Nam Co basin of the Tibetan Plateau. Chinese Science Bulletin 55, 1294-1303.

Zhu, L., Zhen, X., Wang, J., Lü, H., Xie, M., Kitagawa, H., Possnert, G., 2009. A ~ 30,000-year record of environmental changes inferred from Lake Chen Co, Southern Tibet. Journal of Paleolimnology 42, 343-358.